NUMERICAL STUDY OF ISOTHERMAL TWO-PHASE FLOW DISPERSION IN THE PACKED BED OF A HYDRODESULFURIZATION REACTOR

Manuel Martínez del Álamo

Dipòsit Legal: T. 1711-2011

Manuel Martínez del Álamo

NUMERICAL STUDY OF ISOTHERMAL TWO-PHASE FLOW DISPERSION IN THE PACKED BED OF A HYDRODESULFURIZATION REACTOR

PhD Thesis
directed by
Dr. Jordi Pallarès Curto
Dr. Francesc Xavier Grau Vidal

Mechanical Engineering Department

UNIVERSITAT ROVIRA I VIRGILI

Tarragona
2011

WE STATE:

That the present work, entitled

Numerical study of isothermal two-phase flow dispersion in the packed bed of a hydrodesulfurization reactor

presented by Manuel Martínez del Álamo to opt to the degree of PhD in Chemical, Environmental and Process Engineering has been developed under our supervision and that all results achieved are consequence of the work done by the aforementioned PhD student.

And, to inform you of that and in order for it to have the needed effects, we sign this certification.

Tarragona, July 2011.

Dr. Jordi Pallarès Curto

Dr. Francesc Xavier Grau Vidal

Contents

UNIVERSITAT ROVIRA I VIRGILI
NUMERICAL STUDY OF ISOTHERMAL TWO-PHASE FLOW DISPERSION IN THE PACKED BED OF A HYDRODESULFURIZATION REACTOR
Manuel Martínez del Álamo
DL:T. 1711-2011

Abstract

Trickle-bed reactors are commonly used in the industry for hydrodesulfurization processes. In these two-phase flow fixed-bed reactors gas and liquid descend co-currently through a packed bed of solid catalyst particles. The uniformity of the two-phase flow over the bed is a key parameter for the optimum performance of the catalyst. A maldistribution of the two-phase mixture decreases the effective volume of the reactor in which the hydrodesulfurization occurs, and in addition it can lead to the formation of hot spots which may decrease the catalyst life. Hence, it is of great importance to have a tool which can correctly predict the behavior of these two-phase flows through packed beds.

The main objective of this work is to predict the two-phase flow dispersion in a trickle-bed reactor. Since the flow and the dispersion are dominated by mechanical effects, physical properties are considered to remain constant and chemical reactions, heat and mass transfer processes are not taken into account. In order to develop the flow model, a realistic case study has been chosen, consisting in an industry scale reactor (2.77 m in diameter and 19.68 m in height) with four beds with different porosities and filled with particles of different sizes. Before the reaction zone, there is a distribution tray above the beds, where the two-phase flow is expected to mix before entering the first of the beds.

Two different tools are used in this study. The first one is the well established and widely used commercial CFD software Fluent. However, drag and capillarity models not available by default in the software are implemented through *User Defined Functions*, written in C programming language. The second tool is a domestic CFD code named *Multiphase Flow Solver (MFS)*, which has been developed during this PhD thesis, constituting one of the objectives of this work.

There is no need to model turbulence in porous media for the flow conditions considered. Simulations performed with and without implementing a turbulence model yield the same results. This simplifies slightly the already complex modelization of two-phase flow dispersion in porous media. Capillarity is the most important cause of the dispersion of the two-phase flow in a packed bed, and at the same time it is also one of the major causes of complexity of the model. Changes in this term have a big impact both on the flow behavior and on the numerical stability of the model.

Fluent predicts accurately the macroscopic pressure drop in this type of flows for the operating conditions of interest in this study, but there are two issues regarding two-phase flow dispersion in porous media which need to be properly solved. One is the lack of a continuous dispersion as the flow descends through the bed. The second issue which needs to be solved is the reconcentration of liquid when the flow moves from a less porous bed to one more porous. Despite those two issues, the overall magnitude of the predicted two-phase flow dispersion is in reasonable agreement with the experimental data available in the literature, a fact which allows the software to be used in most of the cases presented in this PhD thesis.

At the current state of development MFS provides already realistic results, more consistent with experimental data than those provided by commercial software. Nevertheless, further numerical work has to be done in order to provide the code with better numerical stability. MFS is also able to incorporate a capillarity term without the stability problems of Fluent. In addition, the current version of MFS can be used for parallel computation on shared memory machines with OpenMP.

No significant differences are found in the two-phase flow dispersion between different regions of the reactor. Two different regions of the trickle-bed reactor are studied: one containing the projection of a chimney from the center of the distribution tray and its surrounding area and another one for a near-wall region, containing also the projection of one chimney and three additional half-chimneys from the surrounding region. The distribution of the liquid phase does not change significatively as the flow descends, except at the interface of two beds with different porosity.

No flow attachment to the wall is observed. The regions under the projections

of the chimneys from the distribution tray placed near the wall spread the liquid faster in radial direction in the first 3 m of the reactor than those in the center of the reactor. That tendency changes from a depth of 5 m on, and the regions under the projections of the chimneys placed at the center of the distribution tray spread the liquid faster radially than those placed near the wall of the reactor. Liquid descends with higher velocity in the central region than in the near-wall region, which allows the liquid from surrounding regions to move towards the center of the reactor. However, given the plumes displacement and the reactor dimensions, any wall effect on the flow is discarded.

The simulations predict that a completely uniform distribution in the first 11 m of the reactor is not achieved. However, a uniform distribution is reached for the first 0.3 m in radial direction at a bed depth of 11 m.

Aknowledgements

This work has been carried out in the ECoMMFiT research group, from the Mechanical Engineering Department of the ETSEQ of University Rovira i Virgili, under the supervision of Dr. Jordi Pallarès and Dr. Francesc Xavier Grau.

I want to thank both of them for having guided me through this road, sometimes rocky, to finally reach the end and overcoming the difficulties which often arose while walking it. Their knowledge, availability and advices have been of great value, and without them I probably would have not been able to cross the finish line.

My parents also had a big impact on this. First of all, because obviously I would not be here had they never met each other. On a serious note, I want to thank their support during these years I spent battling time and again in front of a computer screen, fighting the numerical instabilities and other enemies who suddenly came out of nowhere. They are among the few people who, when I said I was doing a PhD, did not reply *"And when are you going to get a job?"*.

I also want to thank my workmates and friends Roland, Guille, Sylvana, Pedro, Sibel, Salva, Núria, José, the rest of the *Fountain Square Team* (they know what I mean) and all the PhD students, professors, technicians and administrative staff, past and present, who made my stay in the group comfortable and with whom I shared some very good moments.

Thanks to Núria Juanpere for always being willing to help with all the paperwork, since the very first day until now.

I want to express my gratitude to Repsol for the financial support to execute this PhD thesis, and specially Antonio López and Miguel Ángel García, from the

Repsol Technological Center in Móstoles.

And last but not least, I want to thank the members of the jury to accept the invitation to evaluate this work.

List of Figures

List of Tables

Chapter 1

Introduction

Trickle-bed reactors are commonly used in the industry, and particularly in hydrodesulfurization processes, which remove sulphur from oil related products. Hydrogen is mixed with the fuel and hydrogen sulfide is formed. The chemical reaction takes place at high temperature and high pressure. In the two-phase flow fixed-bed reactors used in the industry for hydrodesulfurization processes, gas and liquid phases descend co-currently through a fixed bed of solid catalyst particles. The two-phase flow uniformity over the bed is a key parameter for the optimum performance of the catalyst. A non-uniform distribution of the two-phase mixture decreases the effective volume of the reactor in which the hydrodesulfurization takes place, and it could lead to the formation of hot spots which may decrease the catalyst life. Hence it is of great importance to have a tool which can correctly reproduce the behavior of this type of flows. First, to gain knowledge on what is happening inside the reactor and, secondly, to carry out the modifications needed to optimize its performance.

Trickle-bed reactors usually operate on various flow regimes [1]:

- Spray flow, where gas is a continuous phase with liquid drops.
- Trickle flow, where there are one directional liquid rivulets and some discontinuous liquid films with a continous gas phase.
- Pulse flow, intermittent passage of gas -and liquid- rich zones through the reactor.
- Downward bubble flow, where liquid is the continuous phase with dispersed gas flow.

1.1 Bibliography review

The interest to obtain a uniform well mixed two-phase flow in catalytic beds has motivated most of the studies carried out to determine the liquid spreading in packed beds. Cihla and Schmidt [2] proposed a series of analytical solutions to an advection-diffusion equation to predict the liquid spreading in a column, for different types of inlet distributors. The mathematical model assumes a radial diffusion term with an adjustable diffusion coefficient and an advection term along the axial direction. Baker et al. [3] carried out experimental studies in columns of different sizes and filled with particles of different shapes and sizes to evaluate the radial liquid spreading. These authors found that initial uniform distribution is essential, since the flow from a single stream needs a length equivalent to four or five column diameters to become uniform. Wang et al. [4] studied experimentally the radial liquid maldistribution in trickle beds. They found that the small-scale maldistribution was dominated by the gas-liquid interaction, while the solid-liquid interaction governed the large-scale maldistribution. Boyer and Fanget [5] developed a new gamma-ray tomographic system to measure liquid distribution in a trickle-bed. Harter et al. [6] used two experimental techniques to study the flow distribution inside a catalyst bed: a collecting device and a gamma-ray tomographic system.

Jiang et al. [7, 8] simulated the macroscale multiphase flow in packed beds and compared the results with available experimental data. The CFDLIB package, based in the Eulerian k-fluid model, was used in their simulations. The Holub model [9] for particle-fluid interactions and the Attou model [10] for gas-liquid interaction were implemented in the model. The comparison showed that the k-fluid model predicted reasonably well the pressure gradient and the global liquid saturation in the trickle flow regime for liquid upflow in a cylindrical packed bed. Gunjal et al. [11] studied the liquid distribution in a trickle bed reactor, both experimental and numerically, for different cases, including an asymmetric liquid inlet. Commercial CFD software Fluent [12] was used in their simulations. Radial liquid spreading was underpredicted, due to lack of performance of the capillary model, according to the authors. Boyer et al. [13] studied liquid spreading from a point source in a column through gamma-ray tomography and numerical simulation. CFDLIB was also used in their simulations. The comparison showed that the prediction of the radial liquid spreading was strongly affected by the capillary pressure term. Different

models for this term were tested and a modification of this capillary pressure term was proposed to fit experimental data better.

Jiang et al. [14] used an extended DCM (*Discrete Cell Model*) to study two-phase flow distribution. In the DCM the trickle bed is modelled as a number of cells which are inter-connected. DCM results were compared to both CFD and experimental results, and according to the authors, both numerical results were quantitatively comparable between them and qualitatively comparable to the experimental data.

There have been also several works in the development of computational codes for multiphase flows. Harlow and Amsden [15] developed a computing technique for multiphase flows, where the momentum transport between phases was implicit, allowing for different degrees of coupling between them. It was used in different applications, but not in a trickle-bed column. Moukalled and Darwish [16, 17] developed pressure-based algorithms for multiphase flow calculation with two different approaches: mass conservation [16] and geometric conservation [17]. They were used in a wide variety of multiphase flow problems, but none of them was a trickle-bed column, neither.

Despite the amount of research carried out on this type flows, besides the study of Boyer et al. [13] there is no published work, as far as this author knows, of a computational code able to accurately deal with radial non-uniformities in multiphase flows through packed beds. Most of the computational fluid dynamics studies published to this point either avoid radial non-uniformities or take them into account but do not provide detailed results on flow distribution, centering their results around macroscopic variables.

1.2 Objectives

The main objective of this study is to predict the behavior of a two-phase flow, liquid and gas, which flows downwards through a fixed-bed of solid static particles in a catalytic reactor. Since the flow and the dispersion are dominated by mechanical effects, physical properties are considered to remain constant and chemical re-

actions, heat and mass transfer processes are not taken into account. In order to develop the flow model, a realistic case study has been chosen, consisting in an industry scale reactor (2.77 m in diameter and 19.68 m in height) with four catalytic beds with different porosities and filled with particles of different sizes. Before the reaction zone, there is a distribution tray above the beds, where the two-phase flow is expected to mix before entering the first packed bed. The knowledge of the flow distribution is key to determine the actual reactor operation. It is expected to know if the flow distribution is uniform in radial direction, if there are regions where phases are poorly mixed and if the two-phase flow behaves in a different way in the near-wall region than in the central region.

At first, the commercial CFD software Fluent [12] is used to study this type of two-phase flow through packed beds. One of the goals of this work is to implement additional drag and capillarity models not included by default in the software to improve its accuracy in the prediction of the two-phase flow dispersion. In order to do that, the models have to be entered through *User Defined Functions (UDF)*, written in C programming language. This may generate some additional numerical instabilities in the solution process, so it is important to implement those UDF's correctly to avoid numerical instabilities.

Given the current lack of computational tools able to accurately predict two-phase flow dispersion through packed beds, the development of a domestic computational code which correctly models this type of flows is an objective of this PhD thesis. Since, with the exception of the article by Boyer et al. [13], there are no published works, as far as this author knows, of a CFD code which predicts with accuracy the two-phase flow dispersion in packed beds, the development of such a tool will be a contribution to the current state of the art in the field of Multiphase Computational Fluid Dynamics.

Due to the complexity of the system, seven different cases are studied. The first three of those cases are used to validate the computational tools, the fourth case compares two different tools (Fluent and the domestic code) under the same conditions and the last three cases focus on the two-phase flow dispersion inside the reactor.

Chapter 2

Antecedents

The subject of this PhD Thesis traces its roots back to 2004, when Repsol approached the ECoMMFiT research group at University Rovira i Virgili with the aim of working together in a project to study flow patterns in hydrodesulfurization reactors. At that time, the focus was to study the flow behavior in the distribution tray of a reactor. Jordi López, under the supervision of Dr. Pallarès and Dr. Grau, carried out the first part of that study until early 2005.

The hydrodesulfurization reactor operates in trickle-flow regime. The liquid and gas inlet is placed at the top of the reactor, which has a distribution tray to mix both phases. This tray is settled with chimneys, whose purpose is to help the two-phase flow to be better distributed. Below the distribution tray there are four catalytic beds of different porosity each and filled with different types of particles. It is in these beds where the chemical reactions take place and sulphur is removed from oil. A sketch of the reactor is shown in Figure 2.1.

In that initial period, the flow behavior inside a chimney was studied, and the relationship between the liquid flow and the liquid height outside a chimney was determined. As an example, flow distribution in a chimney and at its outlet can be seen in Figure 2.2.

In that part of the project the flow distribution at the catalytic bed inlet was also obtained, as shown in Figure 2.3, where an upper view of liquid volume fraction contours is shown, being the red color a liquid volume fraction of 0.4 and the blue

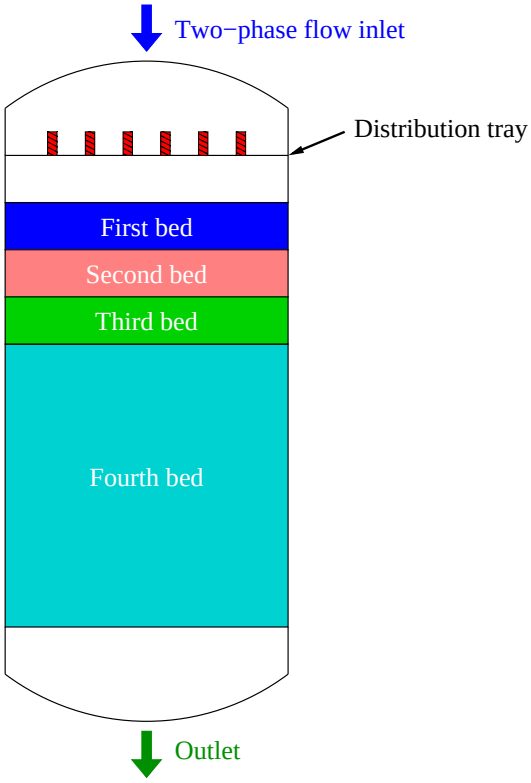

Figure 2.1: Sketch of the reactor

color gas. The arrow shows the gas inlet direction into the chimney. The white circumference corresponds to the projection of a chimney on the bed inlet.

Besides studying the flow behavior in a chimney, its behavior was also studied in the distribution tray. Numerical simulations with a computational domain comprising one quarter of the tray, since that is the existing symmetry in the system, were carried out to determine the liquid heights distribution in the tray and, consequently, the flow distribution. Figure 2.4 shows the heights distribution obtained which, as it can be seen, is highly uniform. Figure 2.5 shows a plot with the angular average heights of liquid on the tray in the radial direction. As it can be observed in the plot, the maximum deviation in height was of 3 mm (up to 2 % of the mean height).

As the last part of this initial study, a simulation to check the possible effects of the tray inclination on the flow distribution was carried out. It must be noted that

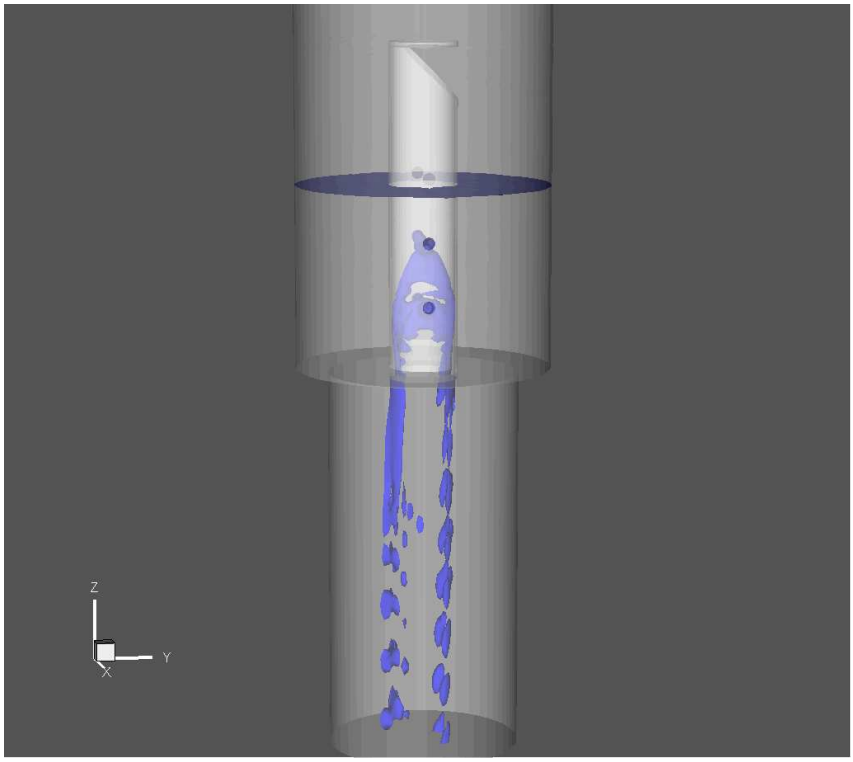

Figure 2.2: Flow distribution in a chimney. Isosurface of the liquid volume fraction 0.3.

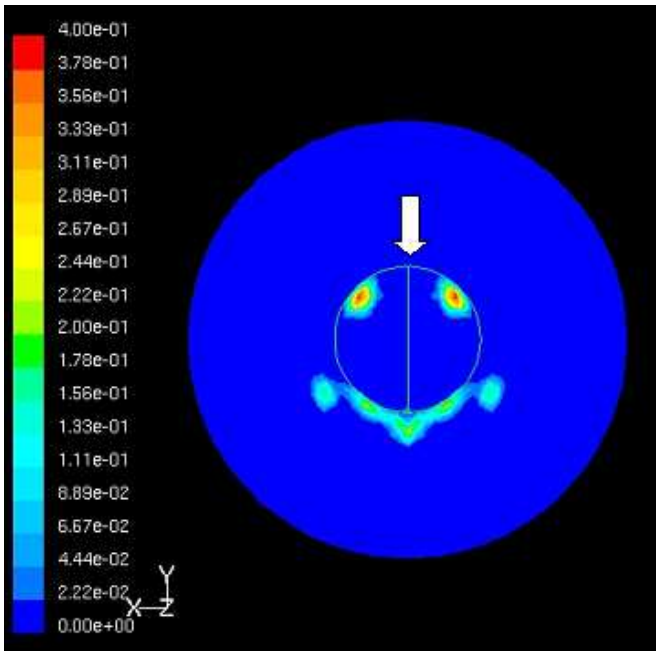

Figure 2.3: Flow distribution at the bed inlet. Contours of the liquid volume fraction.

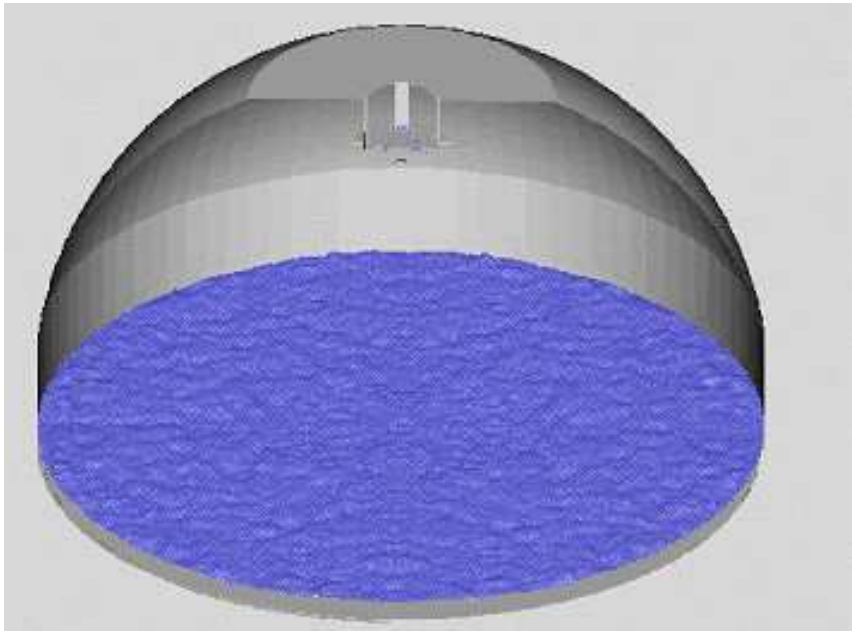

Figure 2.4: Liquid heights distribution in the distribution tray. Isosurface of the liquid volume fraction.

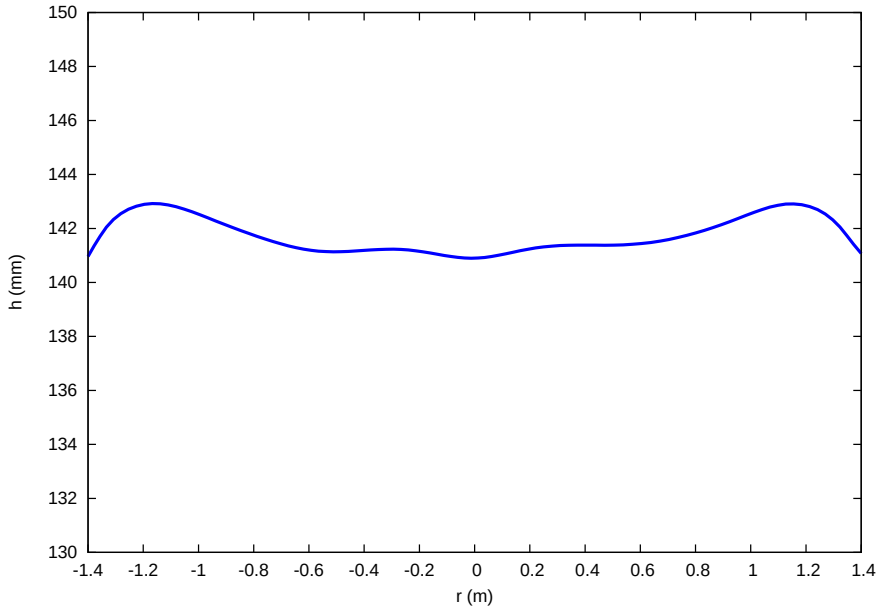

Figure 2.5: Liquid heights on the distribution tray with no inclination

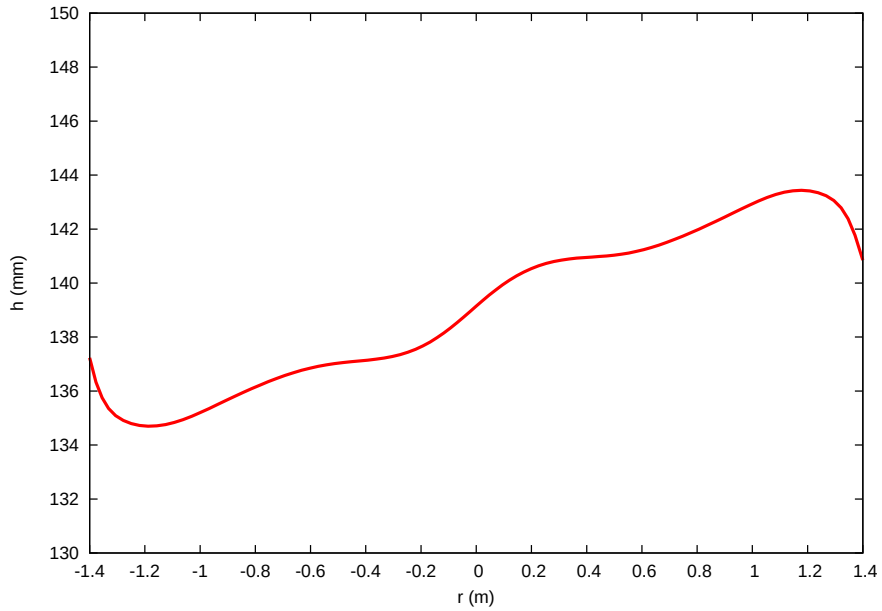

Figure 2.6: Liquid heights on the distribution tray with an 8-mm inclination. Computational domain a quarter of the tray.

this study was also carried out on a computational domain corresponding to one quarter of the tray, which although correct in the case of a non-inclined tray, it is not strictly true in the case of the inclined tray, since the real existing symmetry in that case is of 180^{o} and not 90^{o}. The inclination considered was of 8 mm. Results for this inclination are shown in Figure 2.6, where it can be seen that the liquid heights distribution varied 10 mm from the minimum to the maximum heights. The direction of the inclination is in the x-axis positive direction.

In June 2005, I joined that project, continuing the work that Jordi López had started. New goals for the project were established then and carried out. The inclination of the tray was studied without resorting to any non-strictly true symmetry element, in other words, performing the simulations in a computational domain comprising one half of the tray. Figure 2.7 shows the liquid heights distribution on the tray for an inclination of 8 mm, with a computational domain of half tray. As it can be observed, the maximum deviation of liquid heights was of 6 mm, 4 mm less than the predicted with a computational domain of a quarter of the tray and 3 mm more than in a non-inclined tray. Figure 2.8 plots the three cases together.

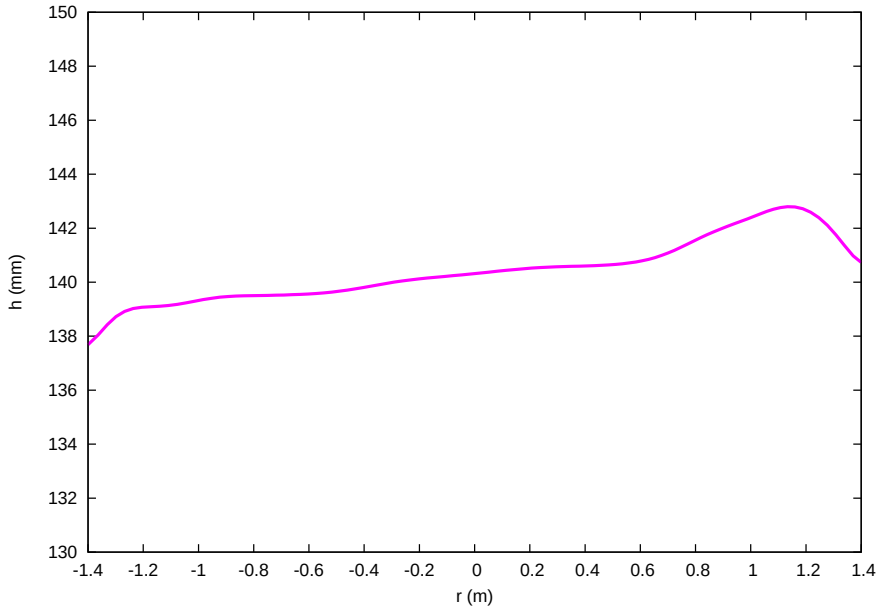

Figure 2.7: Liquid heights on the distribution tray with an 8-mm inclination. Computational domain half tray.

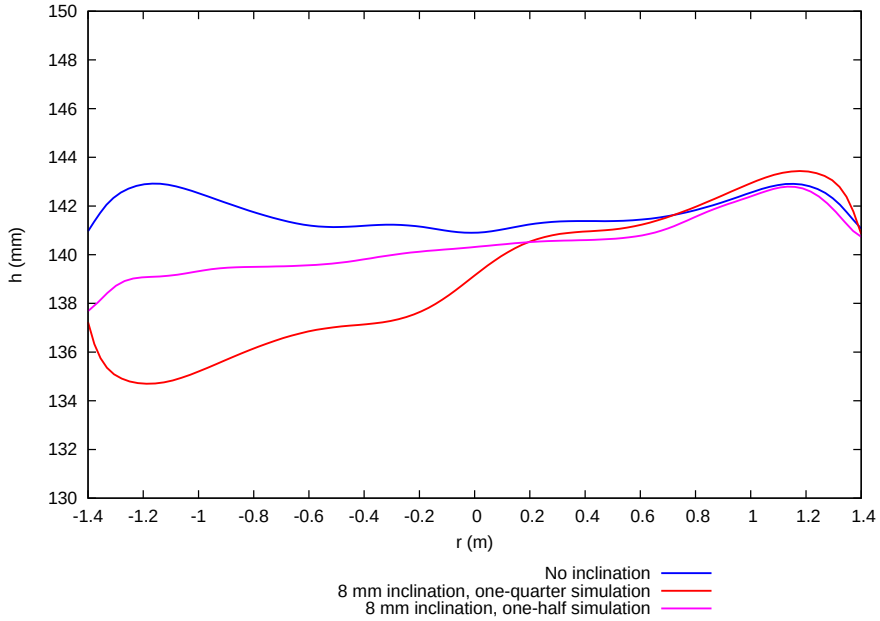

Figure 2.8: Liquid heights on the distribution tray.

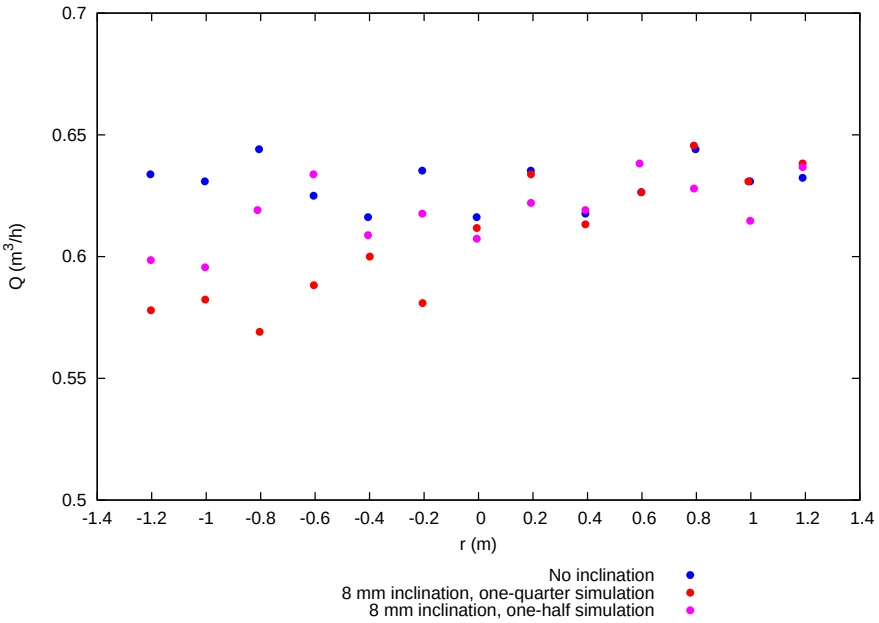

Figure 2.9: Liquid flow rates through the chimneys of the distribution tray.

The liquid height on the tray is related to the liquid flow rate through the chimneys. Figure 2.9 shows the liquid flow rate values through the chimneys. The dots are plotted at the radial position where the chimneys are placed. As it can be seen, there was a significative difference between simulating one quarter or half of the tray. In the chimney placed at a radial position of -0.8 m, the difference in liquid flow rate was of 0.05 m^3/h (8 %), which means that the assumption of a symmetry of one quarter of the tray was not accurate enough. Taking the half tray simulation as reference, the effect of the inclination was not a big one. The maximum difference was of 0.035 m^3/h (5.6 %).

The next step was to validate the dispersion models for two-phase flows available in Fluent and to study the dispersion in the reactor beds without taking into account chemical reaction nor heat or mass transfer effects. These topics are presented and analyzed in the following chapters and they constitute the main body of this thesis.

Chapter 3

Physical model

The main objective of this work is to study the two-phase flow dispersion on beds of solid particles for a hydrodesulfurization reactor. However, in order to properly simulate the reactor itself, the tools used need to be validated through comparison with available data in the literature. Hence different cases have been studied (both for validation purposes and for the study of the two-phase flow dispersion), which are shown in Table 3.1. The physical models of the seven cases considered are described in the following subsections.

3.1 Case A: Flow regime influence

In this case, the possible effect of turbulence in the flow through porous media is studied. A single-phase flow of water through a prism is used for this simulation. There is no need for a two-phase flow since it is the effect of turbulence on a packed bed the one subject of study for this case. The domain can be seen in Figure 3.1,

Table 3.1: Studied cases

Case	Description
A	Flow regime influence
B	Pressure drop validation
C	Two-phase flow dispersion validation
D	Two-phase flow dispersion with a porosity change
E	Two-phase flow dispersion in the central region of the reactor
F	Two-phase flow dispersion in the near-wall region of the reactor
G	Effect of the wall in the two-phase flow distribution along the reactor

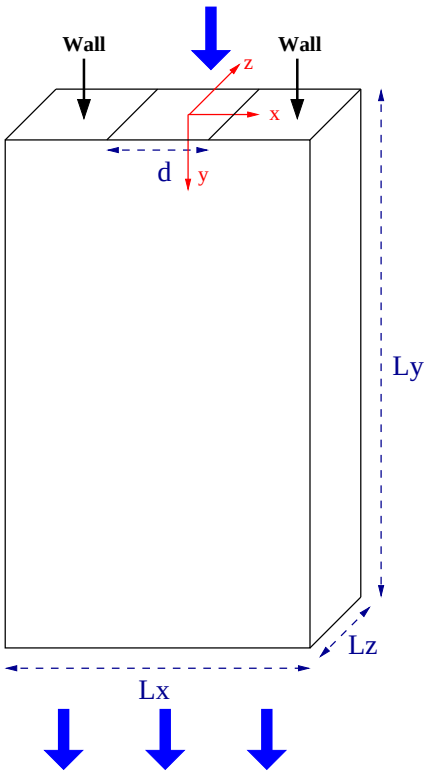

Figure 3.1: Sketch of the prism used in the simulations to determine the flow regime influence.

whose dimensions are shown in Table 3.2. Water at room temperature enters the prism through the central part of the upper face and exits through the lower face. The inlet surface velocity is 0.1 m/s and the media porosity is 0.5. Non-slipping boundary condition is imposed at the walls.

Table 3.2: Prism dimensions

Variable	Value (m)
L_x	6.0
L_y	10.0
L_z	1.5
d	2.0

3.2 Case B: Pressure drop validation

The pressure drop through a packed bed for a two-phase flow is studied in this case. The original experimental data for this validation can be found in the article

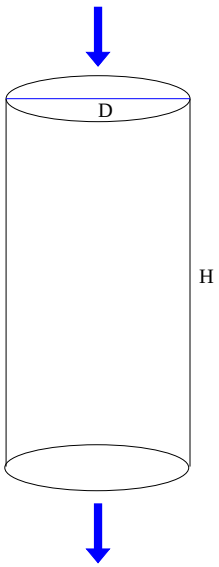

Figure 3.2: Sketch of the column used in the experiments presented by Tsochatzidis et al. [18]

Table 3.3: Column characteristics

Variable	Value
D	0.14 m
H	1.24 m
ε	0.362
d_p	$3.175 \cdot 10^{-3}$ m

by Tsochatzidis et al. [18]. A sketch of the system is shown in Figure 3.2 and the column characteristics are shown in Table 3.3. Air and water at room conditions are the fluids used in this case. Two versions of this case are studied. The first one consists of a series of data with uniform inlet distribution, which means that water and air enter uniformly mixed through the top of the column. In the second set, the inlet flow distribution is not uniform, where half of the inlet presents a uniform mix of air and water while only air enters through the other half.

Two simplifications were made in the simulation in regards to the experiments carried out in that study by Tsochatzidis et al. [18], which are listed below:

1. There is an additional section in the upper part of the column in the experiments. Air enters through the side of that section, at the top of which there is a distributor with holes for the liquid. Given that the complete geometry of the distributor is not provided, it was decided to enter the two-phase mix

through the top of the column shown in Figure 3.2

2. Air is saturated with water in the experiments, in order to avoid mass transfer between the phases. In these simulations air is not saturated. Previous simulations with both saturated and non-saturated air showed that air saturation has no effect, as the difference in the results was less than 1 %.

The different values for both the air and water inlet flow rates are shown in Chapter 6 along the results and discussions for this case, ranging from 1.25 to 13.56 kg/m^2s for water and from 0.136 to 0.366 kg/m^2s for air. Non-slipping boundary conditions are imposed at the cylindrical walls.

3.3 Case C: Two-phase flow dispersion validation

This case is the same as that studied by Boyer et al. [13]. The dispersion of an air-water two-phase flow in a cylindrical vertical packed column is studied in this case. The column has an inner diameter of 0.4 m and a bed height of 1.8 m. The packing consists of spherical glass particles of diameter 1.99 m. Although the authors report the porosity distribution in the bed, an average value of 0.365 has been used as constant porosity in the bed. Both fluids, air and water, are at room temperature. Liquid is injected through a tube of inner diameter 8 mm placed at the center of the top of the column while air is injected around the liquid inlet over the top surface of the column. A sketch of the column is shown in Figure 3.3, where the blue arrow shows the liquid injection and the reds arrows show the region where the air enters the column. Since this case is axisymmetric, the computational domain is only a two-dimensional plane with the same height of the column and width the radius of the column (from the center to the wall). Axisymmetric boundary condition is imposed at the axis (center of the column) and non-slip boundary condition at the wall.

3.4 Case D: Two-phase flow dispersion with a porosity change

Two contiguous beds with different porosities are the subject of study in this case. The two-dimensional domain can be seen in Figure 3.4 while the beds charac-

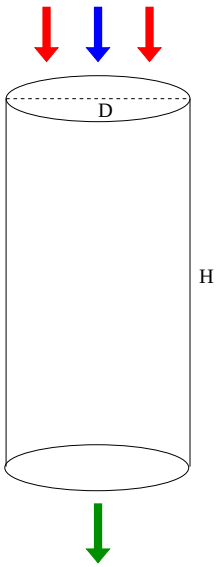

Figure 3.3: Sketch of the column used in the studies of Boyer et al. [13]

teristics and physical properties of the fluids are shown in Table 3.4. The left side is a symmetry axis while the right side is a wall with non-slipping boundary condition. The liquid is entered through the first 4 mm next to the symmetry axis while the gas enters through the rest of the upper face.

3.5 Case E: Two-phase flow dispersion in the central region of the reactor

In this case, the dispersion of a three-dimensional isothermal two-phase flow in the reactor beds is studied, without including neither chemical reactions nor heat and mass transfer processes which take place in a real reactor. The reactor has four beds with particles of different shapes and sizes. A sketch of the reactor was already shown in Figure 2.1. The characteristics of the reactor beds are shown in Table 3.5.

Two different cases for the two-phase flow dispersion in the reactor were studied. The first case considers the flow distribution in the beds below a set of chimneys placed at the central region of the reactor, far from the wall. The inlet conditions are the results from previous simulations where the volume fractions and velocities distributions before entering the first bed were studied. Figure 2.3 shows the vol-

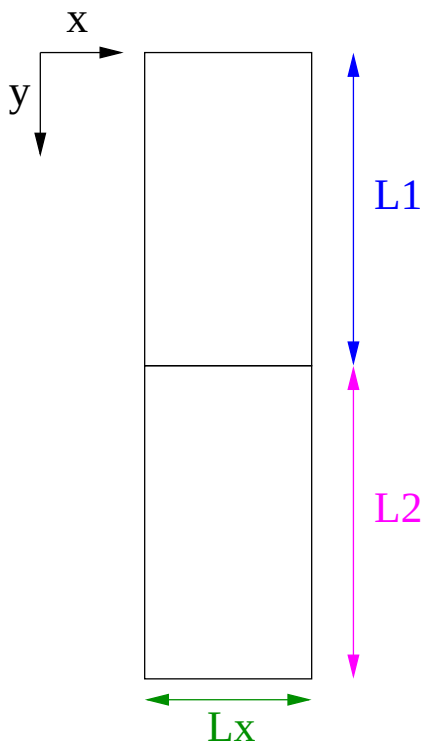

Figure 3.4: Sketch of the contiguous beds configuration.

Table 3.4: Reactor system characteristics in two beds of different porosity.

Top bed porosity	0.33
Bottom bed porosity	0.53
L1 (mm)	150
L2 (mm)	150
Lx (mm)	100
v_l (x $<$ 4 mm)	0.22 m/s
v_g (4 mm $<$ x $<$ 200 mm)	$2.8{\cdot}10^{-3}$ m/s
ρ_l	611 kg/m^3
ρ_g	20.8 kg/m^3
μ_l	$1.7{\cdot}10^{-4}$ $Pa\ s$
μ_g	$2.52{\cdot}10^{-2}$ $Pa\ s$
Drag in x-direction	Yes
Drag in y-direction	Yes
Capillarity	Yes

Table 3.5: Beds characteristics

Bed	**Porosity**	**Depth** (*mm*)
1	0.33	150
2	0.53	150
3	0.45	150
4	0.40	15560

ume fraction distribution at the inlet of the first bed.

The domain for this case consists of a rhombic section prism. The dimensions of this cross section, centered around one chimney's projection, are selected according to the symmetry elements existing in the chimneys distribution on the tray. The velocities and volume fractions set at the inlet were obtained from the previous simulation of the flow at the inlet section of the reactor, the latter previously shown in Figure 2.3. Figure 3.5 shows the placement of one of the chimneys belonging to the central region (computational domain represented by the red rhombus) while Figure 3.6 shows the computational domain for this case. The chimney's projection is shown in Figure 3.6 at the top of the bed. The four beds are also shown in this figure. Periodic boundary conditions are imposed at the lateral walls of the domain to model the effect of the surrounding chimneys. The height of the fourth bed has been considered of 450 mm, since previous simulations predict fully developed flow for beds deeper than 70 mm. An regular hexahedral mesh of 1346700 computational cells is used in the simulation for this case.

3.6 Case F: Two-phase flow dispersion in the near-wall region of the reactor

The second case considers the flow distribution near the reactor wall. As in the previous case for the central region, the inlet conditions are the results from previous simulations where the volume fractions and velocities distributions before entering the first bed were studied.

Figure 3.7 shows, within a red rectangle, one of the chimneys belonging to the

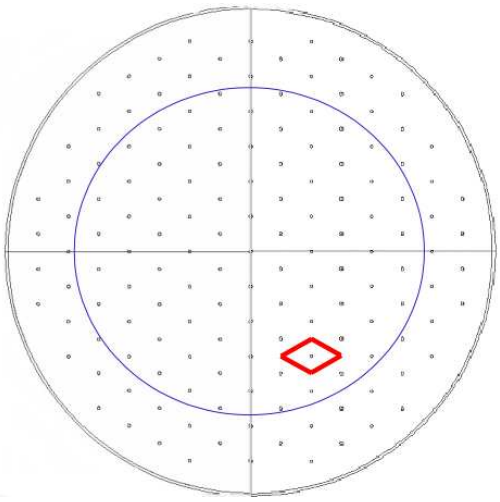

Figure 3.5: Above view of the chimneys distribution on the tray. Projection of a chimney of the central region.

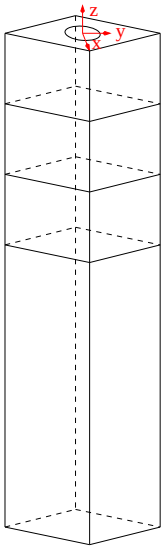

Figure 3.6: Computational domain for the central region simulation.

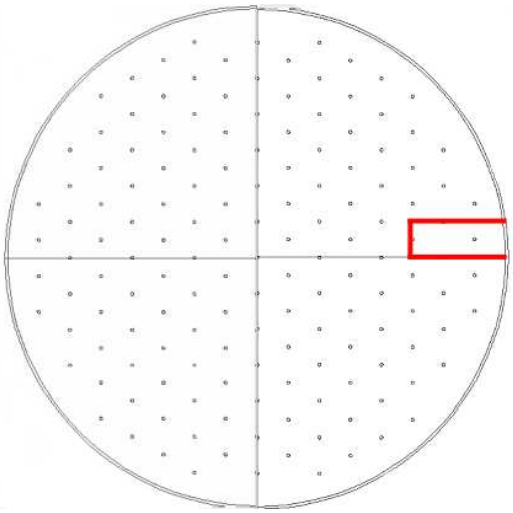

Figure 3.7: Above view of the chimneys distribution on the tray. Projection of a chimney of the near-wall region.

near-wall region. The computational domain for this region, shown in Figure 3.8, consists of a prism of rectangular section. The chimneys projections contained in the rectangle representing the top of the bed are shown in Figure 3.8. As it can be seen in Figure 3.8, the top of the computational domain contains the projection of one chimney placed near the wall and three halves of the projection of one chimney distributed along the perimeter of the top surface. Specific volume fraction and inlet velocity distributions are imposed at the top of the bed as inlet boundary conditions, in agreement with numerical simulations of flow at the outlet of a chimney. No-slip condition is set at the wall and symmetry boundary conditions at the lateral faces of the domain, which are perpendicular to the y direction. At the boundaries opposite of the wall, velocities and volume fractions distributions are imposed, which are obtained from the simulation of the flow in a central region of the bed. A regular hexahedral mesh of 1228500 computational cells is used for this simulation.

3.7 Case G: Effect of the wall on the two-phase flow distribution along the reactor

A study of the possible effect of the wall on the two-phase flow distribution is carried out in this case. That effect, where the liquid tends to attach the wall of

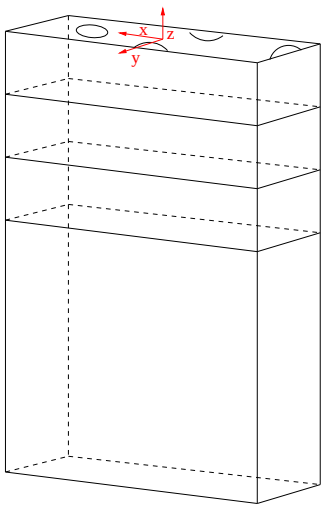

Figure 3.8: Computational domain for the near-wall region simulation.

the column, is known as *wall effect*, and it is one of the causes of flow maldistribution. An increased wall flow causes the large-scale liquid maldistribution, as reported by Wang et al. [4]. Several authors have studied this effect, which is one to be avoided in order to have a good liquid distribution, as noted by Hoftyzer [19]. Other interesting studies on liquid maldistribution on packed columns include those by Gunn [20], Cairns [21], Cihla and Schmidt [2], Marchot et al. [22] and Baker et al. [3].

The study for this case is carried out for one fourth of the reactor, since that is the existing symmetry. Figure 3.9 shows an upper view of the domain and the inlet boundary condition used in the simulations for this case. As it can be seen in the liquid volume fraction contours shown, the liquid focuses distribution is in agreement with the chimneys distribution on the distribution tray. This distribution of liquid volume fraction cannot be as detailed as it was for the two previous cases, due to the larger region to simulate, which translates into a coarser computational mesh. Non-slipping boundary condition is imposed at the wall and symmetry conditions at the two lateral faces.

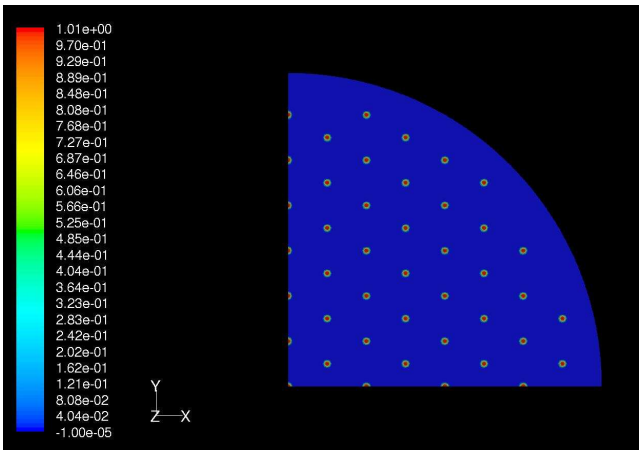

Figure 3.9: Inlet boundary condition. Liquid volume fraction contours.

Chapter 4

Mathematical model

This chapter is devoted to the presentation of the mathematical model that governs the flow in the physical models described in the previous chapter. The two-phase flow which flows through the bed of particles must satisfy the continuity and momentum equations in both phases. The flow is modelled considering continuity and momentum equations for each of the phases, linking them through interaction terms (drag and capillarity). The sum of volume fractions equal to one is another requirement which has to be satisfied. In the following sections, the equations which constitute the mathematical model in cartesian coordinates for a two-dimensional system with the gravity vector aligned along the positive y direction are shown.

4.1 Continuity

The continuity equation for the liquid is:

$$\frac{\partial \theta_l}{\partial t} + \frac{\partial (\theta_l u_l)}{\partial x} + \frac{\partial (\theta_l v_l)}{\partial y} = 0 \tag{4.1}$$

And for the gas:

$$\frac{\partial \theta_g}{\partial t} + \frac{\partial (\theta_g u_g)}{\partial x} + \frac{\partial (\theta_g v_g)}{\partial y} = 0 \tag{4.2}$$

4.2 Sum of volume fractions

In order to keep the flow volume conservation, the sum of volume fractions from the different phases has to be equal to one:

$$\theta_l + \theta_g + \theta_s = 1 \tag{4.3}$$

4.3 Momentum conservation

The momentum equation for the liquid in the x direction is:

$$\begin{aligned} &\overbrace{\frac{\partial \theta_l u_l}{\partial t}}^{Time\ evolution} + \overbrace{\frac{\partial\left(\theta_l u_l^2\right)}{\partial x} + \frac{\partial\left(\theta_l u_l v_l\right)}{\partial y}}^{Convection} = \overbrace{\frac{\mu_l}{\rho_l}\frac{\partial}{\partial x}\left(\theta_l \frac{\partial u_l}{\partial x}\right) + \frac{\mu_l}{\rho_l}\frac{\partial}{\partial y}\left(\theta_l \frac{\partial u_l}{\partial y}\right)}^{Diffusion} - \\ &- \underbrace{\frac{1}{\rho_l}\theta_l \frac{\partial P}{\partial x}}_{Pressure\ gradient} + \underbrace{\frac{1}{\rho_l}\theta_l \theta_s K_{lsx} u_l}_{Liquid-solid\ drag} + \underbrace{\frac{1}{\rho_l}\theta_l \theta_g K_{lgx}\left(u_l - u_g\right)}_{Liquid-gas\ drag} - \underbrace{\frac{1}{\rho_l}\frac{\partial}{\partial x}\theta_l\left(p_l - p_g\right)}_{Capillarity} \end{aligned} \tag{4.4}$$

where the different terms have been explicitly mentioned as an example, as they are referred to in following chapters.

And in the y direction:

$$\begin{aligned} &\frac{\partial \theta_l v_l}{\partial t} + \frac{\partial\left(\theta_l u_l v_l\right)}{\partial x} + \frac{\partial\left(\theta_l v_l^2\right)}{\partial y} = \frac{\mu_l}{\rho_l}\frac{\partial}{\partial x}\left(\theta_l \frac{\partial v_l}{\partial x}\right) + \frac{\mu_l}{\rho_l}\frac{\partial}{\partial y}\left(\theta_l \frac{\partial v_l}{\partial y}\right) - \\ &- \frac{1}{\rho_l}\theta_l \frac{\partial P}{\partial y} + g + \frac{1}{\rho_l}\theta_l \theta_s K_{lsy} v_l + \frac{1}{\rho_l}\theta_l \theta_g K_{lgy}\left(v_l - v_g\right) - \frac{1}{\rho_l}\frac{\partial}{\partial y}\theta_l\left(p_l - p_g\right) \end{aligned} \tag{4.5}$$

The momentum equation for the gas in the x direction is:

$$\begin{aligned} &\frac{\partial \theta_g u_g}{\partial t} + \frac{\partial\left(\theta_g u_g^2\right)}{\partial x} + \frac{\partial\left(\theta_g u_g v_g\right)}{\partial y} = \frac{\mu_g}{\rho_g}\frac{\partial}{\partial x}\left(\theta_g \frac{\partial u_g}{\partial x}\right) + \frac{\mu_g}{\rho_g}\frac{\partial}{\partial y}\left(\theta_g \frac{\partial u_g}{\partial y}\right) - \\ &- \frac{1}{\rho_g}\theta_g \frac{\partial P}{\partial x} + \frac{1}{\rho_g}\theta_g \theta_s K_{gsx} u_g + \frac{1}{\rho_g}\theta_g \theta_l K_{glx}\left(u_g - u_l\right) \end{aligned} \tag{4.6}$$

And in the y direction:

$$\frac{\partial \theta_g v_g}{\partial t} + \frac{\partial \left(\theta_g u_g v_g\right)}{\partial x} + \frac{\partial \left(\theta_g v_g^2\right)}{\partial y} = \frac{\mu_g}{\rho_g}\frac{\partial}{\partial x}\left(\theta_g \frac{\partial v_g}{\partial x}\right) + \frac{\mu_g}{\rho_g}\frac{\partial}{\partial y}\left(\theta_g \frac{\partial v_g}{\partial y}\right) - \\ - \frac{1}{\rho_g}\theta_g \frac{\partial P}{\partial y} + g + \frac{1}{\rho_g}\theta_g \theta_s K_{gsy} v_g + \frac{1}{\rho_g}\theta_g \theta_l K_{gly}\left(v_g - v_l\right) \tag{4.7}$$

4.3.1 Capillarity

There are two capillarity models widely used. The first of these models was proposed by Attou and Ferschneider [23], and it is shown in Equation 4.8.

$$p_l - p_g = -2\sigma_s\left(1-f\right)\left(\frac{\theta_s}{1-\theta_g}\right)^{\frac{1}{3}}\left(\frac{1}{dp} + \frac{1}{d_{min}}\right)F\left(\frac{\rho_g}{\rho_l}\right) \tag{4.8}$$

The wet efficiency, f, [24] is computed in the following manner:

$$f = 1.021\left(\frac{\theta_l}{1-\theta_s}\right)^{0.224} \tag{4.9}$$

And the pressure factor is:

$$F\left(\frac{\rho_g}{\rho_l}\right) = 1 + 88.1\frac{\rho_g}{\rho_l} \tag{4.10}$$

The minimum diameter is obtained using the following expression:

$$d_{min} = \left(\frac{\sqrt{3}}{\pi} - 0.5\right)^{0.5} dp \tag{4.11}$$

The second model model for capillarity was proposed by Grosser et al. [25] and is shown in Equation 4.12.

$$p_l - p_g = -\left(1-f\right)\sigma_s \frac{\sqrt{180}\theta_s}{\left(1-\theta_s\right)d_e}\left[0.48 + 0.036\ln\left(\frac{1-\theta_s-\theta_l}{\theta_l}\right)\right] \tag{4.12}$$

4.3.2 Drag

The drag terms which link the fluid and solid phases follow the Holub [9] model. The drag coefficients between the gas and solid phases in the x and y directions, respectively, are computed using the following expressions:

$$K_{gsx} = \left(A_{gs}\mu_g\theta_g u_g + B_{gs}\rho_g\theta_g^2 u_g^2\right)\frac{1}{(1-\varepsilon)\,|u_g|} \tag{4.13}$$

$$K_{gsy} = \left(A_{gs}\mu_g\theta_g v_g + B_{gs}\rho_g\theta_g^2 v_g^2\right)\frac{1}{(1-\varepsilon)\,|v_g|} \tag{4.14}$$

where

$$A_{gs} = 180\frac{(1-\varepsilon)^2}{\theta_g^3 dp^2} \tag{4.15}$$

$$B_{gs} = 1.8\frac{(1-\varepsilon)}{\theta_g^3 dp} \tag{4.16}$$

In a similar manner, the drag coefficients between the liquid and solid phases are:

$$K_{lsx} = \left(A_{ls}\mu_l\theta_l u_l + B_{ls}\rho_l\theta_l^2 u_l^2\right)\frac{1}{(1-\varepsilon)\,|u_l|} \tag{4.17}$$

$$K_{lsy} = \left(A_{ls}\mu_l\theta_l v_l + B_{ls}\rho_l\theta_l^2 v_l^2\right)\frac{1}{(1-\varepsilon)\,|v_l|} \tag{4.18}$$

where

$$A_{ls} = 180\frac{(1-\varepsilon)^2}{\theta_l^3 dp^2} \tag{4.19}$$

$$B_{ls} = 1.8\frac{(1-\varepsilon)}{\theta_l^3 dp} \tag{4.20}$$

The interaction between the two fluid phases, gas and liquid, is modelled in the following manner [10]:

$$K_{glx} = \frac{\theta_g}{\varepsilon}\left(A_{gl}\mu_g\theta_g|u_g - u_l| + B_{ls}\rho_g\theta_g^2|u_g - u_l|^2\right)\frac{1}{(1-\varepsilon)\,|u_g - u_l|} \tag{4.21}$$

$$K_{gly} = \frac{\theta_g}{\varepsilon}\left(A_{gl}\mu_g\theta_g|v_g - v_l| + B_{ls}\rho_g\theta_g^2|v_g - v_l|^2\right)\frac{1}{(1-\varepsilon)\,|v_g - v_l|} \tag{4.22}$$

where

$$A_{gl} = 180\frac{(1-\theta_g)^2}{\theta_g^3 dp^2}\left[\frac{1-\varepsilon}{1-\theta_g}\right]^{\frac{2}{3}} \tag{4.23}$$

$$B_{gl} = 1.8\frac{(1-\theta_g)}{\theta_g^3 dp}\left[\frac{1-\varepsilon}{1-\theta_g}\right]^{\frac{1}{3}} \tag{4.24}$$

Chapter 5

Multiphase Flow Solver

Multiphase Flow Solver (MFS) is a domestic two-dimensional code in cartesian coordinates for two-phase flows which flow through a bed of static particles. It constitutes the main objective of this work, since it gathers all the modelling required to predict flow dispersion in trickle-beds: the complete mathematical model together with the appropriate numerical approximations. Treatment of continuity and momentum equations is independent for each of the phases, which are linked through interaction terms (drag and capillarity) and the sum of volume fractions equal to unity. Pressure correction is based on SIMPLE [26], adapted to multiphase systems. MFS is written in Fortran programming language and it is parallelized for use with OpenMP libraries in shared-memory machines.

5.1 Linearization of the convective terms

The nonlinearity of the convective terms coupled with the large gradients between the liquid and gas phases in some regions of the domain makes the solution process highly unstable under certain conditions. In order to remove those instabilities, the convective terms are linearized using Picard's approach [27]. But before linearization, some numerical manipulation and combination of the momentum equations with the continuity equations yields an easier to solve version of the momentum equations. In the following mathematical manipulation of equations the phase index has been dropped because the same procedure is applied to both phases.

Applying the *chain rule* to the convective term in the x-velocity equation:

$$\begin{aligned}&\frac{\partial \theta u}{\partial t}+\frac{\partial \theta uu}{\partial x}+\frac{\partial \theta uv}{\partial y}= \\ &=\theta\frac{\partial u}{\partial t}+u\frac{\partial \theta}{\partial t}+\theta\frac{\partial uu}{\partial x}+u\frac{\partial \theta u}{\partial x}+\theta\frac{\partial uv}{\partial y}+u\frac{\partial \theta v}{\partial y}= \\ &=\theta\frac{\partial u}{\partial t}+\theta\frac{\partial uu}{\partial x}+\theta\frac{\partial uv}{\partial y}+u\frac{\partial \theta}{\partial t}+u\frac{\partial \theta u}{\partial x}+u\frac{\partial \theta v}{\partial y}\end{aligned} \tag{5.1}$$

The continuity equation states:

$$\frac{\partial \theta}{\partial t}+\frac{\partial \theta u}{\partial x}+\frac{\partial \theta v}{\partial y}=0 \tag{5.2}$$

Combining Eq. 5.1 and 5.2, yields:

$$\theta\frac{\partial u}{\partial t}+\theta\frac{\partial uu}{\partial x}+\theta\frac{\partial uv}{\partial y} \tag{5.3}$$

The diffusive terms can also be re-arranged after applying the *chain rule*:

$$\begin{aligned}&\frac{\mu}{\rho}\frac{\partial}{\partial x}\left(\theta\frac{\partial u}{\partial x}\right)+\frac{\mu}{\rho}\frac{\partial}{\partial y}\left(\theta\frac{\partial u}{\partial y}\right)= \\ &=\frac{\mu}{\rho}\left[\frac{\partial \theta}{\partial x}\frac{\partial u}{\partial x}+\theta\frac{\partial^2 u}{\partial x^2}\right]+\frac{\mu}{\rho}\left[\frac{\partial \theta}{\partial y}\frac{\partial u}{\partial y}+\theta\frac{\partial^2 u}{\partial y^2}\right]\end{aligned} \tag{5.4}$$

Rearranging the x-momentum equation, one obtains:

$$\begin{aligned}&\frac{\partial u}{\partial t}+\frac{\partial uu}{\partial x}+\frac{\partial uv}{\partial y}=\frac{\mu}{\rho}\frac{1}{\theta}\left[\frac{\partial \theta}{\partial x}\frac{\partial u}{\partial x}+\theta\frac{\partial^2 u}{\partial x^2}\right]+\frac{\mu}{\rho}\frac{1}{\theta}\left[\frac{\partial \theta}{\partial y}\frac{\partial u}{\partial y}+\theta\frac{\partial^2 u}{\partial y^2}\right]-\frac{1}{\rho}\frac{\partial P}{\partial x}+ \\ &+\frac{1}{\rho}K_s\theta_s u+\frac{1}{\rho}K_f\theta_f\left(u-u_f\right)-\frac{1}{\rho}\left(\frac{\partial\left(p_l-p_g\right)}{\partial x}+\left(p_l-p_g\right)\frac{1}{\theta}\frac{\partial \theta}{\partial x}\right)\end{aligned} \tag{5.5}$$

Linearizing the convective term:

$$\frac{\partial u}{\partial t}+\frac{\partial uu}{\partial x}+\frac{\partial uv}{\partial y}=\frac{\partial u}{\partial t}+2u^*\frac{\partial u}{\partial x}+u^*\frac{\partial v}{\partial y}+v^*\frac{\partial u}{\partial y} \tag{5.6}$$

where u^* and v^* are the velocities in the previous iteration.

Introducing the linearized term into the x-momentum equation (Eq. 5.5):

$$\frac{\partial u}{\partial t}+2u^*\frac{\partial u}{\partial x}+u^*\frac{\partial v}{\partial y}+v^*\frac{\partial u}{\partial y}=\frac{\mu}{\rho}\left[\frac{1}{\theta}\frac{\partial \theta}{\partial x}\frac{\partial u}{\partial x}+\frac{\partial^2 u}{\partial x^2}\right]+\frac{\mu}{\rho}\left[\frac{1}{\theta}\frac{\partial \theta}{\partial y}\frac{\partial u}{\partial y}+\frac{\partial^2 u}{\partial y^2}\right]-\frac{1}{\rho}\frac{\partial P}{\partial x}+$$
$$+\frac{1}{\rho}K_s\theta_s u+\frac{1}{\rho}K_f\theta_f\left(u-u_f\right)-\frac{1}{\rho}\left(\frac{\partial\left(p_l-p_g\right)}{\partial x}+\left(p_l-p_g\right)\frac{1}{\theta}\frac{\partial \theta}{\partial x}\right) \tag{5.7}$$

The same procedure is followed for the y-direction velocity equation. The *chain rule* is applied to the convective term:

$$\begin{aligned}&\frac{\partial \theta v}{\partial t}+\frac{\partial \theta uv}{\partial x}+\frac{\partial \theta vv}{\partial y}=\\&=\theta\frac{\partial v}{\partial t}+v\frac{\partial \theta}{\partial t}+\theta\frac{\partial uv}{\partial x}+v\frac{\partial \theta u}{\partial x}+\theta\frac{\partial vv}{\partial y}+v\frac{\partial \theta v}{\partial y}=\\&=\theta\frac{\partial v}{\partial t}+\theta\frac{\partial uv}{\partial x}+\theta\frac{\partial vv}{\partial y}+v\frac{\partial \theta}{\partial t}+v\frac{\partial \theta u}{\partial x}+v\frac{\partial \theta v}{\partial y}\end{aligned} \tag{5.8}$$

Combining Eq. 5.8 and the continuity equation (5.2), yields:

$$\theta\frac{\partial v}{\partial t}+\theta\frac{\partial uv}{\partial x}+\theta\frac{\partial vv}{\partial y} \tag{5.9}$$

Re-arranging the diffusive term after applying the *chain rule*:

$$\begin{aligned}&\frac{\mu}{\rho}\frac{\partial}{\partial x}\left(\theta\frac{\partial v}{\partial x}\right)+\frac{\mu}{\rho}\frac{\partial}{\partial y}\left(\theta\frac{\partial v}{\partial y}\right)=\\&=\frac{\mu}{\rho}\left[\frac{\partial \theta}{\partial x}\frac{\partial v}{\partial x}+\theta\frac{\partial^2 v}{\partial x^2}\right]+\frac{\mu}{\rho}\left[\frac{\partial \theta}{\partial y}\frac{\partial v}{\partial y}+\theta\frac{\partial^2 v}{\partial y^2}\right]\end{aligned} \tag{5.10}$$

Rearranging the y-momentum equation, one obtains:

$$\frac{\partial v}{\partial t}+\frac{\partial uv}{\partial x}+\frac{\partial vv}{\partial y}=\frac{\mu}{\rho}\frac{1}{\theta}\left[\frac{\partial \theta}{\partial x}\frac{\partial v}{\partial x}+\theta\frac{\partial^2 v}{\partial x^2}\right]+\frac{\mu}{\rho}\frac{1}{\theta}\left[\frac{\partial \theta}{\partial y}\frac{\partial v}{\partial y}+\theta\frac{\partial^2 v}{\partial y^2}\right]-\frac{1}{\rho}\frac{\partial P}{\partial y}+g+$$
$$+\frac{1}{\rho}K_s\theta_s v+\frac{1}{\rho}K_f\theta_f\left(v-v_f\right)-\frac{1}{\rho}\left(\frac{\partial\left(p_l-p_g\right)}{\partial y}+\left(p_l-p_g\right)\frac{1}{\theta}\frac{\partial \theta}{\partial y}\right) \tag{5.11}$$

Linearizing the convective term:

$$\frac{\partial v}{\partial t}+\frac{\partial uv}{\partial x}+\frac{\partial vv}{\partial y}=\frac{\partial v}{\partial t}+u^*\frac{\partial v}{\partial x}+v^*\frac{\partial u}{\partial x}+2v^*\frac{\partial v}{\partial y} \tag{5.12}$$

where u^* and v^* are, again, the velocities in the previous iteration.

Introducing the linearized term into the y-momentum equation (Eq. 5.11):

$$\frac{\partial v}{\partial t}+u^*\frac{\partial v}{\partial x}+v^*\frac{\partial u}{\partial x}+2v^*\frac{\partial v}{\partial y}=\frac{\mu}{\rho}\left[\frac{1}{\theta}\frac{\partial \theta}{\partial x}\frac{\partial v}{\partial x}+\frac{\partial^2 v}{\partial x^2}\right]+\frac{\mu}{\rho}\left[\frac{1}{\theta}\frac{\partial \theta}{\partial y}\frac{\partial v}{\partial y}+\frac{\partial^2 v}{\partial y^2}\right]-\frac{1}{\rho}\frac{\partial P}{\partial y}+$$
$$+g+\frac{1}{\rho}K_s\theta_s v+\frac{1}{\rho}K_f\theta_f\left(v-v_f\right)-\frac{1}{\rho}\left(\frac{\partial\left(p_l-p_g\right)}{\partial y}+\left(p_l-p_g\right)\frac{1}{\theta}\frac{\partial \theta}{\partial y}\right) \tag{5.13}$$

5.2 Computational grid

The set of equations is discretized using the finite volume technique [26]. The computational domain is divided in cells which form a grid. This computational grid used is staggered, where scalars (volume fractions, pressure) are placed at the center of the cells while the vectors (velocities) are placed at the cell faces.

The fact of using a staggered mesh provides the computational code with more physical consistency. If this type of mesh is not used, both the scalars and the vectors would be placed at the same position, which could lead to results with no physical sense, as for example a highly non-uniform pressure field treated as uniform in the momentum equations [26].

A representation of the mesh used is shown in Figure 5.1. The computational cells are those in blue, where the indexes for x and y direction, I and J, respectively, are written in capital letters to show that they are placed at the center of the cell. The i and j indexes, written in lower case letters, show the placement of the faces in the x and y directions, respectively. The green dashed cells contain the x-direction vectors (hence the first index in lower case letters and the second one in capital letters) while the red dashed cells contain the y-direction vectors (first index in capital letters and the second one in lower case letters).

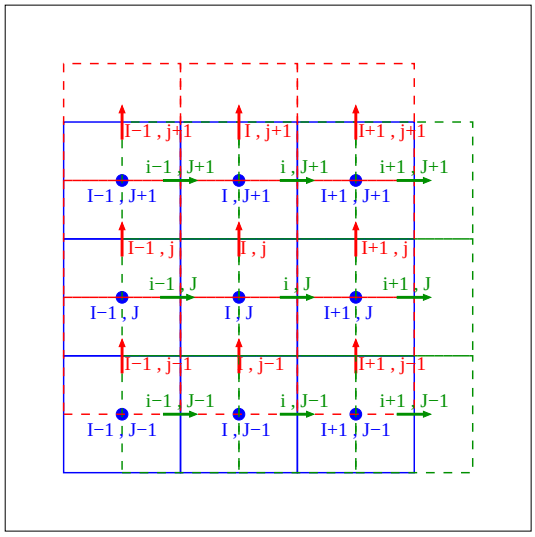

Figure 5.1: Computational mesh used in the MFS code

5.3 Discretization schemes

Due to the mesh configuration, it becomes necessary to interpolate some variables values when discretizing the equations. For example, to obtain the volume fraction values at the cell faces. Several different discretization schemes exist. Given the nature of the system which is being studied, where large gradients exist at the inlet, numerical instabilities appear. In order to avoid those instabilities, an *upwind* scheme is used for the convective terms. Since it takes into account flow direction, transportiveness is assured. In addition, the *upwind* scheme avoids the formation of wiggles [26]. The drag terms are also discretized using an *upwind* scheme. All other terms are discretized following a centered scheme.

Figure 5.2 shows a one-dimensional grid, over which both the centered and *upwind* schemes are explained. The capital letters refer to the cell centers, where *P* is equivalent to the *I,J* node shown in Figure 5.1 and *E*, the east neighbor, is the equivalent of the *I+1,J* node. The small size letters refer to the face values, which are unknown: *w* stands for the west face, *e* for the east face and *ee* for the east face of the east neighboring cell.

The centered scheme interpolates the face values, for any scalar ϕ, in the following manner:

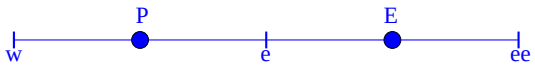

Figure 5.2: One-dimensional grid

$$\phi_e = \frac{1}{2}(\phi_P + \phi_E) \tag{5.14}$$

The *upwind* scheme takes into account the flow direction, so it gives the variable at the face its value at the center of the cell upstream.

$$\phi_e = \phi_P \tag{5.15}$$

5.4 Discretized equations

According to the discretization schemes previously described and the type of grid used, the set of equations is discretized in order to be solved numerically. To avoid repetition, phase indexes have been dropped in the discrete version of the continuity and momentum equations, being one of them for each phase.

5.4.1 Continuity

The discrete version of the continuity equation (Eq. 5.2) reads:

$$\begin{aligned} &\frac{\theta^*_{I,J} - \theta^{old}_{I,J}}{\Delta t} + \frac{1}{2}\left[\frac{\left(\theta^*_{I,J} + \theta^*_{I+1,J}\right)u_{i,J} - \left(\theta^*_{I-1,J} + \theta^*_{I,J}\right)u_{i-1,J}}{\Delta x}\right] + \\ &+ \frac{1}{2}\left[\frac{\left(\theta^*_{I,J} + \theta^*_{I,J+1}\right)v_{I,j} - \left(\theta^*_{I,J-1} + \theta^*_{I,J}\right)v_{I,j-1}}{\Delta y}\right] = 0 \end{aligned} \tag{5.16}$$

In order to be used to solve for the volume fraction, terms are rearranged, where the volume fraction is solved iteratively in an implicit manner using a tridiagonal matrix algorithm (TDMA) [28]:

$$\begin{aligned} AP_{I,J}\theta_{g\ I,J} &= AE_{I,J}\theta_{g\ I+1,J} + AW_{I,J}\theta_{g\ I-1,J} \\ &+ AN_{I,J}\theta_{g\ I,J+1} + AS_{I,J}\theta_{g\ I,J-1} + S_{I,J} \end{aligned} \tag{5.17}$$

Coefficients for the TDMA to solve for volume fraction:

$$AP_{I,J} = 1 + \frac{1}{2}\frac{\Delta t}{\Delta x}\left(u_{i,J} - u_{i-1,J}\right) + \frac{1}{2}\frac{\Delta t}{\Delta y}\left(v_{I,j} - v_{I,j-1}\right)$$

$$AE_{I,J} = -\frac{1}{2}\frac{\Delta t}{\Delta x}u_{i,J}$$

$$AW_{I,J} = \frac{1}{2}\frac{\Delta t}{\Delta x}u_{i-1,J}$$

$$AN_{I,J} = -\frac{1}{2}\frac{\Delta t}{\Delta y}v_{i,J}$$

$$AS_{I,J} = \frac{1}{2}\frac{\Delta t}{\Delta y}v_{i,J-1}$$

$$S_{I,J} = \theta_{g\ I,J}^{old}$$

5.4.2 Momentum in *x* direction

The discrete version of the momentum equation in the x direction (Eq. 5.7) reads:

$$
\begin{aligned}
&\frac{1}{\Delta t}\left(u_{i,J}-u_{i,J}^{old}\right)+\frac{1}{\Delta x}u_{i,J}^{*}\left(u_{i+1,J}-u_{i-1,J}\right)+\\
&+\frac{1}{2}\frac{1}{\Delta y}u_{i,J}^{*}\left(v_{I,j}+v_{I+1,j}-v_{I,j-1}-v_{I+1,j-1}\right)+\\
&+\frac{1}{8}\frac{1}{\Delta y}\left(v_{I,j}^{*}+v_{I+1,j}^{*}+v_{I,j-1}^{*}+v_{I+1,j-1}^{*}\right)\left(u_{i,J+1}-u_{i,J-1}\right)=\\
&=\frac{\mu}{\rho}\frac{1}{\Delta x^{2}}\left[\frac{\theta_{I+1,J}-\theta_{I,J}}{\theta_{I,J}+\theta_{I+1,J}}\left(u_{i+1,J}-u_{i-1,J}\right)+\left(u_{i+1,J}-2u_{i,J}+u_{i-1,J}\right)\right]+\\
&+\frac{\mu}{\rho}\frac{1}{\Delta y^{2}}\frac{1}{4}\frac{\theta_{I,J+1}+\theta_{I+1,J+1}-\theta_{I,J}-\theta_{I+1,J}}{\theta_{I,J}+\theta_{I+1,J}}\left(u_{i,J+1}-u_{i,J-1}\right)+\\
&+\frac{\mu}{\rho}\frac{1}{\Delta y^{2}}\left(u_{i,J+1}-2u_{i,J}+u_{i,J-1}\right)-\\
&-\frac{1}{\rho}\frac{1}{\Delta x}\left(P_{I+1,J}-P_{I,J}\right)+\frac{1}{\rho}K_{s\ i,J}\theta_{s\ I,J}u_{i,J}+\frac{1}{\rho}K_{f\ i,J}\theta_{f\ I,J}\left(u_{i,J}-u_{f\ i,J}\right)-\\
&-\frac{1}{\rho}\frac{1}{\Delta x}\left[\left(\Psi_{I+1,J}-\Psi_{I,J}\right)+\left(\Psi_{I+1,J}+\Psi_{I,J}\right)\frac{\theta_{I+1,J}-\theta_{I,J}}{\theta_{I,J}+\theta_{I+1,J}}\right]
\end{aligned}
\tag{5.18}
$$

Rearranging the terms and solving for u:

$$
\begin{aligned}
AP_{i,J}u_{i,J}&=AE_{i,J}u_{i+1,J}+AW_{i,J}u_{i-1,J}+\\
&+AN_{i,J}u_{i,J+1}+AS_{i,J}u_{i,J-1}+S_{i,J}
\end{aligned}
\tag{5.19}
$$

Coefficients for the TDMA to solve for u:

$$
AP_{i,J}=1+2\frac{\mu}{\rho}\left(\frac{\Delta t}{\Delta x^{2}}+\frac{\Delta t}{\Delta y^{2}}\right)-\frac{1}{\rho}\Delta t\left(K_{s\ i,J}\theta_{s\ I,J}+K_{f\ i,J}\theta_{f\ I,J}\right)
$$

$$
AE_{i,J}=-\frac{\Delta t}{\Delta x}u_{i,J}^{*}+\frac{\mu}{\rho}\frac{\Delta t}{\Delta x^{2}}\left(\frac{\theta_{I+1,J}-\theta_{I,J}}{\theta_{I,J}+\theta_{I+1,J}}+1\right)
$$

$$
AW_{i,J}=\frac{\Delta t}{\Delta x}u_{i,J}^{*}-\frac{\mu}{\rho}\frac{\Delta t}{\Delta x^{2}}\left(\frac{\theta_{I+1,J}-\theta_{I,J}}{\theta_{I,J}+\theta_{I+1,J}}-1\right)
$$

$$
\begin{aligned}
AN_{i,J}&=-\frac{1}{8}\frac{\Delta t}{\Delta y}\left(v_{I,j}^{*}+v_{I+1,j}^{*}+v_{I,j-1}^{*}+v_{I+1,j-1}^{*}\right)+\\
&+\frac{\mu}{\rho}\frac{\Delta t}{\Delta y^{2}}\left(\frac{1}{4}\frac{\theta_{I,J+1}+\theta_{I+1,J+1}-\theta_{I,J}-\theta_{I+1,J}}{\theta_{I,J}+\theta_{I+1,J}}+1\right)
\end{aligned}
$$

$$AS_{i,J} = \frac{1}{8}\frac{\Delta t}{\Delta y}\left(v^*_{I,j} + v^*_{I+1,j} + v^*_{I,j-1} + v^*_{I+1,j-1}\right) - \\ - \frac{\mu}{\rho}\frac{\Delta t}{\Delta y^2}\left(\frac{1}{4}\frac{\theta_{I,J+1} + \theta_{I+1,J+1} - \theta_{I,J} - \theta_{I+1,J}}{\theta_{I,J} + \theta_{I+1,J}} - 1\right)$$

$$S_{i,J} = u^{old}_{i,J} - \frac{1}{2}\frac{\Delta t}{\Delta y}u^*_{i,J}\left(v_{I,j} + v_{i+1,j} + v_{I,j-1} + v_{I+1,j-1}\right) - \\ - \frac{1}{\rho}\frac{\Delta t}{\Delta x}\left(P_{I+1,J} - P_{I,J}\right) - \frac{1}{\rho}\Delta t K_{f\ i,J}\theta_{f\ I,J}u_{f\ i,J} - \\ - \frac{1}{\rho}\frac{\Delta t}{\Delta x}\left[\left(\Psi_{I+1,J} - \Psi_{I,J}\right) + \left(\Psi_{I+1,J} - \Psi_{I,J}\right) + \left(\Psi_{I+1,J} + \Psi_{I,J}\right)\frac{\theta_{I+1,J} - \theta_{I,J}}{\theta_{I,J}} + \theta_{I+1,J}\right]$$

5.4.3 Momentum in *y* direction

The discrete version of the momentum equation in the *y* direction (Eq. 5.13) reads:

$$\frac{1}{\Delta t}\left(v_{I,j} - v^{old}_{I,j}\right) + \frac{1}{8}\frac{1}{\Delta x}\left(u^*_{i-1,J+1} + u^*_{i,J+1} + u^*_{i-1,J} + u^*_{i,J}\right)\left(v_{I+1,j} - v_{I-1,j}\right) + \\ + \frac{1}{2}\frac{1}{\Delta x}v^*_{I,j}\left(u_{i,J+1} + u_{i,J} - u_{i-1,J+1} - u_{i-1,J}\right) + \frac{1}{\Delta y}v^*_{I,j}\left(v_{I,j+1} - v_{I,j-1}\right) = \\ = \frac{\mu}{\rho}\frac{1}{\Delta x^2}\frac{\theta_{I+1,J+1} + \theta_{I+1,J} - \theta_{I-1,J+1} - \theta_{I-1,J}}{4\left(\theta_{I,J} + \theta_{I,J+1}\right)}\left(v_{I+1,j} - v_{I-1,j}\right) + \\ + \frac{\mu}{\rho}\frac{1}{\Delta x^2}\left(v_{I+1,j} - 2v_{I,j} + v_{I-1,j}\right) + \\ + \frac{\mu}{\rho}\frac{1}{\Delta y^2}\left[\frac{\theta_{I,J+1} - \theta_{I,J}}{\theta_{I,J} + \theta_{I,J+1}}\left(v_{I,j+1} - v_{I,j-1}\right) + \left(v_{I,j+1} - 2v_{I,j} + v_{I,j-1}\right)\right] - \\ - \frac{1}{\rho}\frac{1}{\Delta y}\left(P_{I,J+1} - P_{I,J}\right) + g + \frac{1}{\rho}K_{s\ I,j}\theta_{s\ I,J}v_{I,j} + \frac{1}{\rho}K_{f\ I,j}\theta_{f\ I,J}\left(v_{I,j} - v_{f\ I,j}\right) - \\ - \frac{1}{\rho}\frac{1}{\Delta y}\left[\left(\Psi_{I,J+1} - \Psi_{I,J}\right) + \left(\Psi_{I,J+1} + \Psi_{I,J}\right)\frac{\theta_{I,J+1} - \theta_{I,J}}{\theta_{I,J} + \theta_{I,J+1}}\right] \tag{5.20}$$

Rearranging the terms and solving for *v*:

$$\begin{aligned} AP_{I,j}v_{I,j} &= AE_{I,j}v_{I+1,j} + AW_{I,j}v_{I-1,j} + \\ &+ AN_{I,j}v_{I,j+1} + AS_{I,j}v_{I,j-1} + S_{I,j} \end{aligned} \tag{5.21}$$

Coefficients for the TDMA to solve for v:

$$AP_{I,j} = 1 + 2\frac{\mu}{\rho}\left(\frac{\Delta t}{\Delta x^2} + \frac{\Delta t}{\Delta y^2}\right) - \frac{1}{\rho}\Delta t\left(K_{s\,I,j}\theta_{s\,I,J} + K_{f\,I,j}\theta_{f\,I,j}\right)$$

$$\begin{aligned} AE_{I,j} &= -\frac{1}{8}\frac{\Delta t}{\Delta x}\left(u^*_{i-1,J+1} + u^*_{i,J+1} + u^*_{i-1,J} + u^*_{i,J}\right) + \\ &+ \frac{\mu}{\rho}\frac{\Delta t}{\Delta x^2}\left(\frac{1}{4}\frac{\theta_{I+1,J+1} + \theta_{I+1,J} - \theta_{I-1,J+1} - \theta_{I-1,J}}{\theta_{I,J} + \theta_{I,J+1}} + 1\right) \end{aligned}$$

$$\begin{aligned} AW_{I,j} &= \frac{1}{8}\frac{\Delta t}{\Delta x}\left(u^*_{i-1,J+1} + u^*_{i,J+1} + u^*_{i-1,J} + u^*_{i,J}\right) - \\ &- \frac{\mu}{\rho}\frac{\Delta t}{\Delta x^2}\left(\frac{1}{4}\frac{\theta_{I+1,J+1} + \theta_{I+1,J} - \theta_{I-1,J+1} - \theta_{I-1,J}}{\theta_{I,J} + \theta_{I,J+1}} - 1\right) \end{aligned}$$

$$AN_{I,j} = -\frac{\Delta t}{\Delta y}v^*_{I,j} + \frac{\mu}{\rho}\frac{\Delta t}{\Delta y^2}\left(\frac{\theta_{I,J+1} - \theta_{I,J}}{\theta_{I,J} + \theta_{I,J+1}} + 1\right)$$

$$AS_{I,j} = \frac{\Delta t}{\Delta y}v^*_{I,j} - \frac{\mu}{\rho}\frac{\Delta t}{\Delta y^2}\left(\frac{\theta_{I,J+1} - \theta_{I,J}}{\theta_{I,J} + \theta_{I,J+1}} - 1\right)$$

$$\begin{aligned} S_{I,j} &= v^{old}_{I,j} - \frac{1}{2}\frac{\Delta t}{\Delta x}v^*_{I,j}\left(u_{i,J+1} + u_{i,J} - u_{i-1,J+1} - u_{i-1,J}\right) - \frac{1}{\rho}\frac{\Delta t}{\Delta y}\left(P_{I,J+1} - P_{I,J}\right) + \\ &+ \Delta t g - \frac{1}{\rho}K_{s\,I,j}\theta_{f\,I,J}v_{f\,I,j} - \frac{1}{\rho}\frac{\Delta t}{\Delta y}\left[\left(\Psi_{I,J+1} - \Psi_{I,J}\right) + \left(\Psi_{I,J+1} - \Psi_{I,J}\right)\frac{\theta_{I,J+1} - \theta_{I,J}}{\theta_{I,J} + \theta_{I,J+1}}\right] \end{aligned}$$

5.5 Pressure and velocities correction

The velocity fields of the liquid and of the gas obtained using the discrete version of the momentum equations, with the initial or guessed pressure field, do not satisfy the continuity equation. For notation convenience, these fields will be designated by $\tilde{u}$, $\tilde{v}$ and $\tilde{P}$, and the ones satisfying the continuity equation by u, v and P. Then,

the corrections can be defined as the value which added to the current field yields the one which satisfies continuity, as stated by Equations 5.22 through 5.24:

$$u = \tilde{u} + u' \tag{5.22}$$

$$v = \tilde{v} + v' \tag{5.23}$$

$$P = \tilde{P} + P' \tag{5.24}$$

In MFS the pressure correction is derived from the continuity equation for the liquid phase. The liquid continuity equation (Eq. 4.1) can be re-written as:

$$\frac{\partial \theta_l}{\partial t} + \frac{\partial \left(\theta_l \left(\tilde{u}_l + u'_l\right)\right)}{\partial x} + \frac{\partial \left(\theta_l \left(\tilde{v}_l + v'_l\right)\right)}{\partial y} = 0 \tag{5.25}$$

In order to obtain the expressions for the velocities corrections, Equations 5.19 and 5.21 are used with a slight variation. The source term is decomposed into the pressure term and the remaining terms (renamed as $S^o_{i,J}$ and $S^o_{I,j}$). In that way, the new expressions for Equations 5.19 and 5.21 which yield the values which satisfy continuity become Equations 5.26 and 5.27.

$$\begin{aligned} AP_{i,J} u_{l\ i,J} &= AE_{i,J} u_{l\ i+1,J} + AW_{i,J} u_{l\ i-1,J} \\ &+ AN_{i,J} u_{l\ i,J+1} + AS_{i,J} u_{l\ i,J-1} + S^o_{i,J} - \frac{1}{\rho_l} \frac{\Delta t}{\Delta x} \left(P_{I+1,J} - P_{I,J}\right) \end{aligned} \tag{5.26}$$

$$\begin{aligned} AP_{I,j} v_{l\ I,j} &= AE_{I,j} v_{l\ I+1,j} + AW_{I,j} v_{l\ I-1,j} \\ &+ AN_{I,j} v_{l\ I,j+1} + AS_{I,j} v_{l\ I,j-1} + S^o_{I,j} - \frac{1}{\rho_l} \frac{\Delta t}{\Delta y} \left(P_{I,J+1} - P_{I,J}\right) \end{aligned} \tag{5.27}$$

However, the current values of u, v and P do not satisfy continuity. Equations 5.19 and 5.21 can be re-written for $\tilde{u}$, $\tilde{v}$ and $\tilde{P}$, yielding Equations 5.28 and 5.29.

$$\begin{aligned} AP_{i,J} \tilde{u}_{l\ i,J} &= AE_{i,J} \tilde{u}_{l\ i+1,J} + AW_{i,J} \tilde{u}_{l\ i-1,J} \\ &+ AN_{i,J} \tilde{u}_{l\ i,J+1} + AS_{i,J} \tilde{u}_{l\ i,J-1} + S^o_{i,J} - \frac{1}{\rho_l} \frac{\Delta t}{\Delta x} \left(\tilde{P}_{I+1,J} - \tilde{P}_{I,J}\right) \end{aligned} \tag{5.28}$$

$$\begin{aligned} AP_{I,j}\tilde{v}_{l\ I,j} &= AE_{I,j}\tilde{v}_{l\ I+1,j} + AW_{I,j}\tilde{v}_{l\ I-1,j} \\ &+ AN_{I,j}\tilde{v}_{l\ I,j+1} + AS_{I,j}\tilde{v}_{l\ I,j-1} + S^{o}_{I,j} - \frac{1}{\rho_l}\frac{\Delta t}{\Delta y}\left(\tilde{P}_{I,J+1} - \tilde{P}_{I,J}\right) \end{aligned} \tag{5.29}$$

Assuming that the values for the coefficients do not change in consecutive sweeps and discarding correction to the neighbors, subtracting Eq. 5.28 from Eq. 5.26 and Eq. 5.29 from Eq. 5.27, Equations 5.30 and 5.31 are obtained.

$$AP_{i,J}\left(u_{l\ i,J} - \tilde{u}_{l\ i,J}\right) = -\frac{1}{\rho_l}\frac{\Delta t}{\Delta x}\left(P_{I+1,J} - P_{I,J} - \tilde{P}_{I+1,J} + \tilde{P}_{I,J}\right) \tag{5.30}$$

$$AP_{I,j}\left(v_{l\ I,j} - \tilde{v}_{l\ I,j}\right) = -\frac{1}{\rho_l}\frac{\Delta t}{\Delta y}\left(P_{I,J+1} - P_{I,J} - \tilde{P}_{I,J+1} + \tilde{P}_{I,J}\right) \tag{5.31}$$

The velocities corrections can then be written as

$$u'_{l\ i,J} = -\alpha_{i,J}\frac{1}{\Delta x}\left(P'_{I+1,J} - P'_{I,J}\right) \tag{5.32}$$

$$v'_{l\ I,j} = -\beta_{I,j}\frac{1}{\Delta y}\left(P'_{I,J+1} - P'_{I,J}\right) \tag{5.33}$$

where the coefficients $\alpha_{i,J}$ and $\beta_{I,j}$ are

$$\alpha_{i,J} = \frac{1}{AP_{i,J}}\frac{1}{\rho_l}\Delta t \tag{5.34}$$

$$\beta_{I,j} = \frac{1}{AP_{I,j}}\frac{1}{\rho_l}\Delta t \tag{5.35}$$

Once the expressions for the velocity corrections are derived, combining the discrete version of Eq. 5.25 with Equations 5.32 and 5.33 one obtains:

$$\begin{aligned}
&\frac{1}{\Delta t}\left(\theta_{l\,I,J}-\theta_{l\,I,J}^{old}\right)+\frac{1}{\Delta x}\frac{1}{2}\left(\theta_{l\,I,J}+\theta_{l\,I+1,J}\right)\left(\tilde{u}_{l\,i,J}-\alpha_{i,J}\frac{1}{\Delta x}\left(P'_{I+1,J}-P'_{I,J}\right)\right)-\\
&-\frac{1}{\Delta x}\frac{1}{2}\left(\theta_{l\,I,J}+\theta_{l\,I-1,J}\right)\left(\tilde{u}_{l\,i-1,J}-\alpha_{i-1,J}\frac{1}{\Delta x}\left(P'_{I,J}-P'_{I-1,J}\right)\right)+\\
&+\frac{1}{\Delta y}\frac{1}{2}\left(\theta_{l\,I,J}+\theta_{l\,I,J+1}\right)\left(\tilde{v}_{l\,I,j}-\beta_{I,j}\frac{1}{\Delta y}\left(P'_{I,J+1}-P'_{I,J}\right)\right)-\\
&-\frac{1}{\Delta y}\frac{1}{2}\left(\theta_{l\,I,J}+\theta_{l\,I,J-1}\right)\left(\tilde{v}_{l\,I,j-1}-\beta_{I,j-1}\frac{1}{\Delta y}\left(P'_{I,J}-P'_{I,J-1}\right)\right)=0
\end{aligned} \tag{5.36}$$

Rearranging terms and solving for the pressure correction:

$$\begin{aligned}
AP_{I,J}P'_{I,J} &= AE_{I,J}P'_{I+1,J}+AW_{I,J}P'_{I-1,J}\\
&+AN_{I,J}P'_{I,J+1}+AS_{I,J}P'_{I,J-1}+S_{I,J}
\end{aligned} \tag{5.37}$$

where the coefficients to solve with a TDMA are:

$$\begin{aligned}
AP_{I,J} &= \frac{1}{2}\frac{1}{\Delta x^2}\left[\left(\theta_{l\,I,J}+\theta_{l\,I+1,J}\right)\alpha_{i,J}+\left(\theta_{l\,I-1,J}+\theta_{l\,I,J}\alpha_{i-1,J}\right)\right]+\\
&+\frac{1}{2}\frac{1}{\Delta y^2}\left[\left(\theta_{l\,I,J}+\theta_{l\,I,J+1}\right)\beta_{I,j}+\left(\theta_{l\,I,J-1}+\theta_{l\,I,J}\beta_{I,j-1}\right)\right]+
\end{aligned}$$

$$AE_{I,J}=\frac{1}{2}\frac{1}{\Delta x^2}\left(\theta_{l\,I,J}+\theta_{l\,I+1,J}\right)\alpha_{i,J}$$

$$AW_{I,J}=\frac{1}{2}\frac{1}{\Delta x^2}\left(\theta_{l\,I-1,J}+\theta_{l\,I,J}\right)\alpha_{i-1,J}$$

$$AN_{I,J}=\frac{1}{2}\frac{1}{\Delta y^2}\left(\theta_{l\,I,J}+\theta_{l\,I,J+1}\right)\beta_{I,j}$$

$$AS_{I,J}=\frac{1}{2}\frac{1}{\Delta y^2}\left(\theta_{l\,I,J-1}+\theta_{l\,I,J}\right)\beta_{I,j-1}$$

$$S_{I,J} = -\frac{1}{\Delta t}\left(\theta_{l\ I,J} - \theta^{old}_{l\ I,J}\right) -$$
$$-\frac{1}{2}\frac{1}{\Delta x}\left[\left(\theta_{l\ I,J} + \theta_{l\ I+1,J}\right)\tilde{u}_{l\ i,J} - \left(\theta_{l\ I-1,J} + \theta_{l\ I,J}\right)\tilde{u}_{i-1,J}\right] -$$
$$-\frac{1}{2}\frac{1}{\Delta y}\left[\left(\theta_{l\ I,J} + \theta_{l\ I,J+1}\right)\tilde{v}_{l\ I,j} - \left(\theta_{l\ I,J-1} + \theta_{l\ I,J}\right)\tilde{v}_{I,j-1}\right]$$

5.6 Convergence criteria

The residual for the liquid continuity equation at each cell is defined as:

$$RES\theta L_{I,J} = \frac{\theta_{l\ I,J} - \theta^{old}_{l\ I,J}}{\Delta t} +$$
$$+\frac{1}{2}\left[\frac{\left(\theta_{l\ I,J} + \theta_{l\ I+1,J}\right)u_{l\ i,J} - \left(\theta_{l\ I-1,J} + \theta_{l\ I,J}\right)u_{l\ i-1,J}}{\Delta x}\right] + \tag{5.38}$$
$$+\frac{1}{2}\left[\frac{\left(\theta_{l\ I,J} + \theta_{l\ I,J+1}\right)v_{l\ I,j} - \left(\theta_{l\ I,J-1} + \theta_{l\ I,J}\right)v_{l\ I,j-1}}{\Delta y}\right]$$

And the convergence criteria is defined as:

$$\frac{\rho_l \sum_I^J |RES\theta L_{I,J}|}{\dot{m}_l} \leq TLC\,(Threshold\ liquid\ continuity) \tag{5.39}$$

In a similar manner, the residual for the gas continuity equation at each cell is:

$$RES\theta G_{I,J} = \frac{\theta_{g\ I,J} - \theta^{old}_{g\ I,J}}{\Delta t} +$$
$$+\frac{1}{2}\left[\frac{\left(\theta_{g\ I,J} + \theta_{g\ I+1,J}\right)u_{g\ i,J} - \left(\theta_{g\ I-1,J} + \theta_{g\ I,J}\right)u_{g\ i-1,J}}{\Delta x}\right] + \tag{5.40}$$
$$+\frac{1}{2}\left[\frac{\left(\theta_{g\ I,J} + \theta_{g\ I,J+1}\right)v_{g\ I,j} - \left(\theta_{g\ I,J-1} + \theta_{g\ I,J}\right)v_{g\ I,j-1}}{\Delta y}\right]$$

And the convergence criteria is defined as:

$$\frac{\rho_g \sum_I^J |RES\theta G_{I,J}|}{\dot{m}_g} \leq TGC\,(Threshold\ gas\ continuity) \tag{5.41}$$

For the liquid u velocity, the residual is defined as:

$$
\begin{aligned}
RESUL_{i,J} = & \frac{1}{\Delta t}\left(u_{l\ i,J} - u_{l\ i,J}^{old}\right) + \\
& + \frac{1}{\Delta x} u_{l\ i,J}\left(u_{l\ i+1,J} - u_{l\ i-1,J}\right) + \frac{1}{2}\frac{1}{\Delta y}\left(u_{l\ i,J+1} - u_{l\ i,J-1}\right) + \\
& + \frac{1}{8}\frac{1}{\Delta y}\left(v_{l\ I,j} + v_{l\ I+1,j} + v_{l\ I,j-1} + v_{l\ I+1,j-1}\right)\left(u_{l\ i,J+1} - u_{l\ i,J-1}\right) - \\
& - \frac{\mu_l}{\rho_l}\frac{1}{\Delta x^2}\left[\frac{\theta_{l\ I+1,J} - \theta_{l\ I,J}}{\theta_{l\ I,J} + \theta_{l\ I+1,J}}\left(u_{l\ i+1,J} - u_{l\ i-1,J}\right) + \left(u_{l\ i+1,J} - 2u_{l\ i,J} + u_{l\ i-1,J}\right)\right] - \\
& - \frac{\mu_l}{\rho_l}\frac{1}{\Delta y^2}\frac{\left(\theta_{l\ I,J+1} + \theta_{l\ I+1,J+1} - \theta_{l\ I,J} - \theta_{l\ I+1,J}\right)\left(u_{l\ i,J+1} - u_{l\ i,J-1}\right)}{4\left(\theta_{l\ I,J} + \theta_{l\ I+1,J}\right)} - \\
& - \frac{\mu_l}{\rho_l}\frac{1}{\Delta y^2}\left(u_{l\ i,J+1} - 2u_{l\ i,J} + u_{l\ i,J-1}\right) + \\
& + \frac{1}{\rho_l}\frac{1}{\Delta x}\left(P_{I+1,J} - P_{I,J}\right) - \frac{1}{\rho_l}K_{ls\ i,J}\theta_{s\ I,J}u_{l\ i,J} - \frac{1}{\rho_l}K_{lg\ i,J}\theta_{g\ I,J}\left(u_{l\ i,J} - u_{g\ i,J}\right) + \\
& + \frac{1}{\rho_l}\frac{1}{\Delta x}\left[\left(\Psi_{I+1,J} - \Psi_{I,J}\right) + \left(\Psi_{I+1,j} + \Psi_{I,J}\frac{\theta_{l\ I+1,J} - \theta_{l\ I,J}}{\theta_{l\ I,J} + \theta_{l\ I+1,J}}\right)\right]
\end{aligned}
\tag{5.42}
$$

And the convergence criteria is:

$$
\frac{\sum_i^J |RESUL_{i,J}|}{maxterm} \leq TLU\,(Threshold\ liquid\ u - velocity) \tag{5.43}
$$

where *maxterm* is the largest of the terms at the right hand side of Equation 5.42.

In a similar manner for the gas u velocity:

$$
\begin{aligned}
RESUG_{i,J} &= \frac{1}{\Delta t}\left(u_{g\ i,J} - u_{g\ i,J}^{old}\right) + \\
&+ \frac{1}{\Delta x} u_{g\ i,J}\left(u_{g\ i+1,J} - u_{g\ i-1,J}\right) + \frac{1}{2}\frac{1}{\Delta y}\left(u_{g\ i,J+1} - u_{g\ i,J-1}\right) + \\
&+ \frac{1}{8}\frac{1}{\Delta y}\left(v_{g\ I,j} + v_{g\ I+1,j} + v_{g\ I,j-1} + v_{g\ I+1,j-1}\right)\left(u_{g\ i,J+1} - u_{g\ i,J-1}\right) - \\
&- \frac{\mu_g}{\rho_g}\frac{1}{\Delta x^2}\left[\frac{\theta_{g\ I+1,J} - \theta_{g\ I,J}}{\theta_{g\ I,J} + \theta_{g\ I+1,J}}\left(u_{g\ i+1,J} - u_{g\ i-1,J}\right) + \left(u_{g\ i+1,J} - 2u_{g\ i,J} + u_{g\ i-1,J}\right)\right] - \\
&- \frac{\mu_g}{\rho_g}\frac{1}{\Delta y^2}\frac{\left(\theta_{g\ I,J+1} + \theta_{g\ I+1,J+1} - \theta_{g\ I,J} - \theta_{g\ I+1,J}\right)\left(u_{g\ i,J+1} - u_{g\ i,J-1}\right)}{4\left(\theta_{g\ I,J} + \theta_{g\ I+1,J}\right)} - \\
&- \frac{\mu_g}{\rho_g}\frac{1}{\Delta y^2}\left(u_{g\ i,J+1} - 2u_{g\ i,J} + u_{g\ i,J-1}\right) + \\
&+ \frac{1}{\rho_g}\frac{1}{\Delta x}\left(P_{I+1,J} - P_{I,J}\right) - \frac{1}{\rho_g} K_{gs\ i,J}\theta_{s\ I,J} u_{g\ i,J} - \frac{1}{\rho_g} K_{gl\ i,J}\theta_{l\ I,J}\left(u_{g\ i,J} - u_{l\ i,J}\right)
\end{aligned}
\tag{5.44}
$$

And the convergence criteria is:

$$
\frac{\sum_i^J |RESUG_{i,J}|}{maxterm} \leq TGU\ (Threshold\ gas\ u - velocity) \tag{5.45}
$$

where *maxterm* is the largest of the terms at the right hand side of Equation 5.44.

The residual for the liquid v velocity is defined as:

$$
\begin{aligned}
RESVL_{I,j} &= \frac{1}{\Delta t}\left(v_{l\ I,j} - v_{l\ I,j}^{old}\right) + \\
&+ \frac{1}{8}\frac{1}{\Delta x}\left(u_{l\ i-1,J+1} + u_{l\ i,J+1} + u_{l\ i-1,J} + u_{l\ i,J}\right)\left(v_{l\ I+1,j} - v_{l\ I-1,j}\right) + \\
&+ \frac{1}{2}\frac{1}{\Delta x}v_{l\ I,j}\left(u_{l\ i,J+1} + u_{l\ i,J} - u_{l\ i-1,J+1} - u_{l\ i-1,J}\right) + \frac{1}{\Delta y}v_{l\ I,j}\left(v_{l\ I,j+1} - v_{l\ I,j-1}\right) - \\
&- \frac{\mu_l}{\rho_l}\frac{1}{\Delta x^2}\frac{\left(\theta_{l\ I+1,J+1} + \theta_{l\ I+1,J} - \theta_{l\ I-1,J+1} - \theta_{l\ I-1,J}\right)\left(v_{l\ I+1,j} - v_{l\ I-1,j}\right)}{4\left(\theta_{l\ I,J} + \theta_{l\ I,J+1}\right)} - \\
&- \frac{\mu_l}{\rho_l}\frac{1}{\Delta x^2}\left(v_{l\ I+1,j} - 2v_{l\ I,j} + v_{l\ I-1,j}\right) - \\
&- \frac{\mu_l}{\rho_l}\frac{1}{\Delta y^2}\left[\frac{\theta_{l\ I,J+1} - \theta_{l\ I,J}}{\theta_{l\ I,J} + \theta_{l\ I,J+1}}\left(v_{l\ I,j+1} - v_{l\ I,j-1}\right) + \left(v_{l\ I,j+1} - 2v_{l\ I,j} + v_{l\ I,j-1}\right)\right] + \\
&+ \frac{1}{\rho_l}\frac{1}{\Delta y}\left(P_{I,J+1} - P_{I,J}\right) - g - \frac{1}{\rho_l}K_{ls\ I,j}\theta_{s\ I,J}v_{l\ I,j} - \frac{1}{\rho_l}K_{lg\ I,j}\theta_{g\ I,J}\left(v_{l\ I,j} - v_{g\ I,j}\right) + \\
&+ \frac{1}{\rho_l}\frac{1}{\Delta y}\left[\left(\Psi_{I,J+1} - \Psi_{I,J}\right) + \left(\Psi_{I,J+1} + \Psi_{I,J}\frac{\theta_{l\ I,J+1} - \theta_{l\ I,J}}{\theta_{l\ I,J} + \theta_{l\ I,J+1}}\right)\right]
\end{aligned}
\tag{5.46}
$$

And the convergence criteria is:

$$
\frac{\sum_i^J |RESVL_{I,j}|}{maxterm} \leq TLV\ (Threshold\ liquid\ v - velocity) \tag{5.47}
$$

where *maxterm* is the largest of the terms at the right hand side of Equation 5.46.

The residual for the gas *v* velocity is defined as:

$$
\begin{aligned}
RESVG_{I,j} &= \frac{1}{\Delta t}\left(v_{g\ I,j} - v_{g\ I,j}^{old}\right) + \\
&+ \frac{1}{8}\frac{1}{\Delta x}\left(u_{g\ i-1,J+1} + u_{g\ i,J+1} + u_{g\ i-1,J} + u_{g\ i,J}\right)\left(v_{g\ I+1,j} - v_{g\ I-1,j}\right) + \\
&+ \frac{1}{2}\frac{1}{\Delta x} v_{g\ I,j}\left(u_{g\ i,J+1} + u_{g\ i,J} - u_{g\ i-1,J+1} - u_{g\ i-1,J}\right) + \\
&+ \frac{1}{\Delta y} v_{g\ I,j}\left(v_{g\ I,j+1} - v_{g\ I,j-1}\right) - \\
&- \frac{\mu_g}{\rho_g}\frac{1}{\Delta x^2}\frac{\left(\theta_{g\ I+1,J+1} + \theta_{g\ I+1,J} - \theta_{g\ I-1,J+1} - \theta_{g\ I-1,J}\right)\left(v_{g\ I+1,j} - v_{g\ I-1,j}\right)}{4\left(\theta_{g\ I,J} + \theta_{g\ I,J+1}\right)} - \\
&- \frac{\mu_g}{\rho_g}\frac{1}{\Delta x^2}\left(v_{g\ I+1,j} - 2v_{g\ I,j} + v_{g\ I-1,j}\right) - \\
&- \frac{\mu_g}{\rho_g}\frac{1}{\Delta y^2}\left[\frac{\theta_{g\ I,J+1} - \theta_{g\ I,J}}{\theta_{g\ I,J} + \theta_{g\ I,J+1}}\left(v_{g\ I,j+1} - v_{g\ I,j-1}\right) + \left(v_{g\ I,j+1} - 2v_{g\ I,j} + v_{g\ I,j-1}\right)\right] + \\
&+ \frac{1}{\rho_g}\frac{1}{\Delta y}\left(P_{I,J+1} - P_{I,J}\right) - g - \frac{1}{\rho_g} K_{gs\ I,j}\theta_{s\ I,J} v_{g\ I,j} - \frac{1}{\rho_g} K_{gl\ I,j}\theta_{l\ I,J}\left(v_{g\ I,j} - v_{l\ I,j}\right)
\end{aligned}
\tag{5.48}
$$

And the convergence criteria is:

$$
\frac{\sum_i^J |RESVG_{I,j}|}{maxterm} \leq TGV\ (Threshold\ gas\ v - velocity) \tag{5.49}
$$

where *maxterm* is the largest of the terms at the right hand side of Equation 5.48.

5.7 Algorithm

Once all the equations are discretized, it is time to solve the equations system to obtain the fields of volume fractions, velocities and pressure. The algorithm used is described below.

1. Variables are initialized at time *n*.

2. Liquid volume fractions are calculated at time *n+1*, solving Equation 5.17 (for each phase) with a TDMA solver. The velocities are those at time *n*.

3. Gas volume fractions are computed using Equation 4.3.

4. Liquid and gas velocities are calculated at time *n+1* using Equations 5.19 and 5.21 (for both phases) with a TDMA solver. The volume fractions are those obtained in the previous step. This is an iterative step in itself, due to the linearization of the convective terms.

5. Pressure correction is calculated using Equation 5.37 with a TDMA solver.

6. Corrections for liquid velocities are computed using Equations 5.32 and 5.33 and new liquid velocities are calculated (Eqs. 5.22 and 5.23).

7. New gas velocities are computed using Equations 5.19 and 5.21 (for the gas phase). The liquid velocities used are those obtained in the previous step.

8. Liquid volume fractions are updated using Equation 5.17 (for the liquid phase). The velocities used are the last computed ones.

9. Gas volume fractions are updated using Equation 4.3, where the liquid volume fractions are those obtained in the previous step.

10. Back to pressure correction (step 5) until all convergence criteria are met.

    In the present computations, all threshold values for residuals have been set equal to 10^{-3}.

Chapter 6

Results and discussion

The results obtained for the different cases described in chapter 3 are presented and discussed in this chapter. In some cases two different tools have been used to obtained these results, the commercial CFD software Fluent [12] and the domestic code MFS.

6.1 Models of flow through porous media available in Fluent

Before simulating the flow dispersion in the reactor, a validation of the different dispersion models available in Fluent was carried out. Fluent offers two models to simulate the flow through porous media: the *Porous media model* and the *Eulerian granular phase model*.

In the *Porous media model* one or more zones need to be defined as porous media. In this zone (defined as porous media) a pressure drop term is added to the momentum equations. This term is comprised of two parts: the viscous part and the inertial one, as shown in Eq. 6.1:

$$\Delta P = \frac{\mu}{\gamma} U_i + C_2 \frac{\rho}{2} |U_i| U \tag{6.1}$$

The viscous and inertial resistance coefficients have to be provided. These coefficients are obtained through the correlations shown in the Eqs. 6.2 and 6.3, for spherical particles.

$$\gamma = \frac{D_p^2}{150}\frac{\varepsilon^3}{1-\varepsilon^2} \tag{6.2}$$

$$C_2 = \frac{3.5\,(1-\varepsilon)}{Dp\;\varepsilon^3} \tag{6.3}$$

The *Eulerian granular phase model* is the second of the models available in Fluent to simulate flow dispersion in particle beds. In this model, the particles have to be defined as a static granular phase, and the system has to be initialized with the volume fraction of the particles. A method to estimate the drag coefficients between the phases has to be chosen as well.

6.2 Case A: Flow regime influence

First of all, the possible effect of turbulence on the flow at the macroscopic level is checked. In order to do that, a simulation using the porous media model is carried out with the domain being a prism, described in detail previously in chapter 3. Two simulations are performed for this case, one with a laminar model and another one with a turbulent ($k-\varepsilon$ *standard*) model [29]. As it can be seen in Figures 6.1 and 6.2, there are no differences between the results of laminar and turbulent simulations, which means that at a macroscopic level, the dissipative effect of the media exceeds that of turbulence so that turbulence has no perceptible effect on the flow through porous media.

Figure 6.1 shows the y-velocity profile in the center of the prism ($x = 0\ m$). It can be observed how the water velocity decreases as it descends through the bed until it reaches a constant velocity when the whole cross section is occupied by water. Figure 6.2 shows the velocity profile 1 m below the water inlet. As it can be seen, water spreads in both directions, resulting in the bell-shape profile which one should expect.

6.3 Case B: Pressure drop validation

The next step was to test the accuracy of the porous media model available in Fluent both for a single-phase flow and a two-phase flow through a packed bed. Two

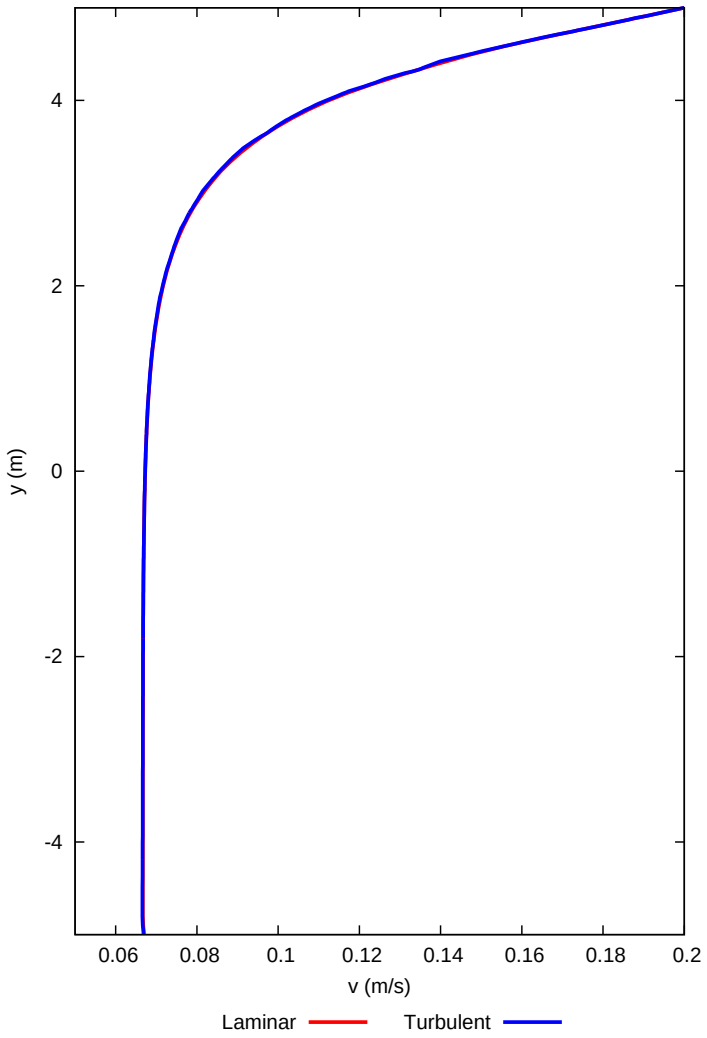

Figure 6.1: Velocities profile at the center of the bed $(x = 0,\ z = 0)$.

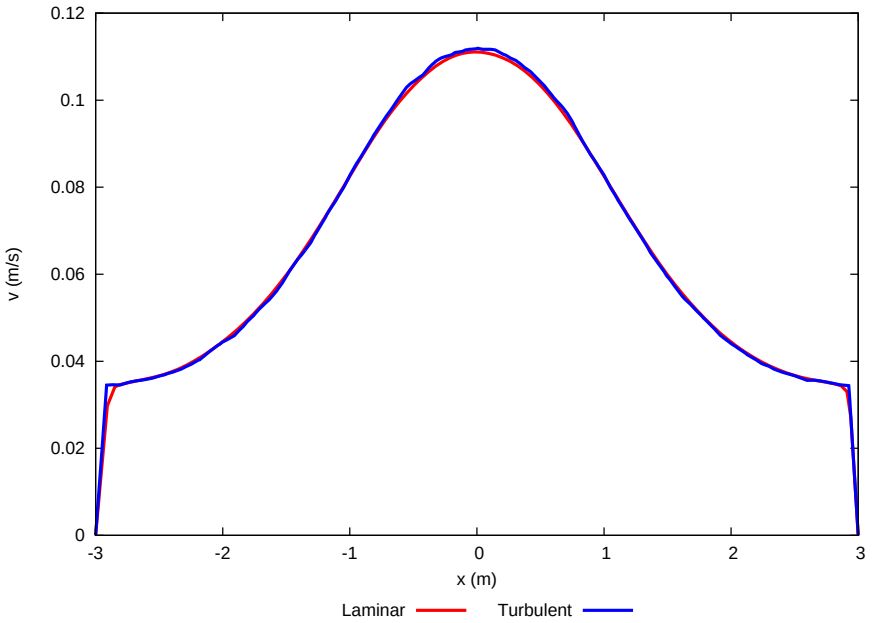

Figure 6.2: Velocities profile 1 m below the inlet.

Table 6.1: Pressure loss comparison

Fluid	**Surface flow rate** (kg/m^2s)	ΔP **Ergun** (kPa/m)	ΔP **Fluent** (kPa/m)	**Difference** $(\%)$
Water	1.250	0.1720	0.1710	0.61
Air	0.297	0.1088	0.1084	0.37

single-phase flow simulations are performed in the column described in chapter 3 for this case, one with water and another one with air. The parameter compared is the pressure drop, and the obtained values are compared to those computed using the Ergun equation [30]. Table 6.1 shows the results obtained for pressure drop between the inlet and outlet in these two simulations, and the comparison with the values obtained using the Ergun equation. As it can be seen, Fluent predicts accurately the pressure drop for single-phase flow, both gas and liquid.

Once it has been checked that Fluent predicted correctly the single-phase flow behavior in porous media regarding pressure drop, the next step is to choose a multiphase model among the ones available in Fluent. A brief description of those models is presented here:

1. *VOF model*: This model is recommended for stratified or free surface flows. It does not allow to define different velocities for each phase.

Table 6.2: Comparison with experimental data

Case	Experimental	Mixture model	Euler model
L (kg/m^2s)	4.060	4.060	4.060
G (kg/m^2s)	0.297	0.297	0.297
ΔP (kPa/m)	10.00	9.00	6.57
Error (%)	-	10.00	34.26

2. *Mixture model*: This model is recommended for flows where phases mix or separate, or for flows in which the volume fraction of the disperse phase is above 10 %. It is recommended specially where the disperse phase is widely distributed in the domain. It solves one momentum equation with the mixture properties.

3. *Euler model*: Like the *Mixture model*, this model is recommended for flows where phases mix or separate, or for flows where the disperse phase is above 10 %. The difference is that the *Euler model* solves one momentum equation for each phase, so it better fits for flows where the disperse phase is concentrated in some parts of the domain.

According to the previous description, the *VOF model* is discarded to be used in the simulations, since in this case phases are mixed. In order to choose between the other two models, it is chosen to reproduce with Fluent one of the experimental cases presented in the article by Tsochatzidis et al. [18] The system is the same that the one shown in Figure 3.2, but in this case a two-phase flow, consisting of water and air, enters the domain. The *Porous media model* was also used in these simulations. The results obtained in these simulations are shown in Table 6.2, where *L* and *G* are the liquid and gas flow rates, respectively. As it can be seen, the *Mixture model* yielded better results for the flow through porous media.

Once the multiphase model which better reproduces reality is chosen, experimental cases are simulated in order to validate Fluent results. This validation is done in two stages. The first stage consists in validating the pressure drop results provided by Fluent, while in the second one the aim is to validate the results for the flow dispersion obtained with Fluent.

The original experimental cases chosen for this validation can be found in the

Table 6.3: Comparison with experimental data for the uniform distribution

L (kg/m^2s)	**G** (kg/m^2s)	**Experimental ΔP** (kPa/m)	**Fluent ΔP** (kPa/m)	**Error** $(\%)$
1.36	0.297	7.00	3.75	-46.38
4.06	0.297	10.00	9.00	-10.00
4.06	0.366	12.00	11.08	-7.69
4.06	0.248	8.00	7.56	-5.50
6.78	0.297	13.00	14.63	+12.58
6.78	0.248	11.00	12.37	+12.46
6.78	0.366	16.00	17.87	+11.71
9.49	0.136	7.50	10.26	+36.76
9.49	0.248	14.00	17.18	+22.71

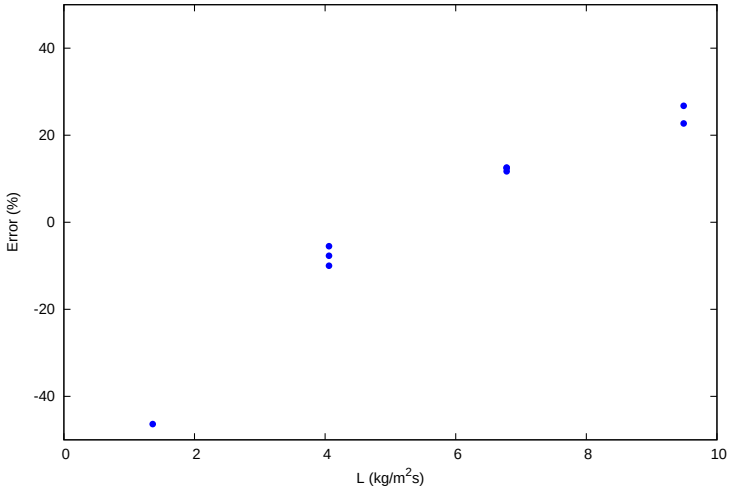

Figure 6.3: Comparison between simulations and experimental data for a uniform inlet distribution.

article by Tsochatzidis et al. [18]. As previously explained in chapter 3, two runs of cases are presented. The first of these runs consist of cases in which the inlet flow distribution is uniform, while in the second run, the inlet flow distribution is not uniform. The results obtained for the uniform distribution cases are shown in Table 6.3 and Figure 6.3. Figure 6.3 shows the surface flow rate of liquid and the error between Fluent results and the experimental data. The points in the same vertical correspond to the same gas flow rate. From Figure 6.3 the following can be concluded:

1. At low liquid flow rates, the pressure drop predicted by Fluent is lower than the experimental one.

Table 6.4: Comparison with experimental data for the non-uniform distribution

L (kg/m^2s)	**G** (kg/m^2s)	**Experimental ΔP** (kPa/m)	**Fluent ΔP** (kPa/m)	**Error** (%)
1.36	0.136	1.80	1.78	-1.07
4.06	0.136	4.00	4.17	+4.23
6.78	0.136	5.50	6.94	+26.24
9.49	0.136	7.00	9.77	+39.63
13.56	0.136	10.00	14.19	+41.89
1.36	0.248	5.00	3.22	-35.53
4.06	0.248	7.00	7.18	+2.53
6.78	0.248	9.00	11.68	+29.81
9.49	0.248	12.00	16.22	+35.18

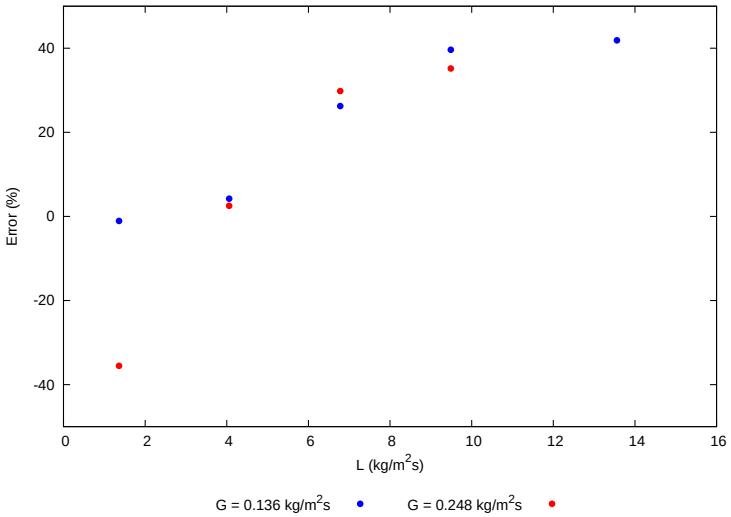

Figure 6.4: Comparison between simulations and experimental data for a non-uniform inlet distribution.

2. At intermediate liquid flow rates, Fluent reproduces accurately the experimental data, with errors around 10 %.

3. At high liquid flow rates, Fluent overestimates the pressure drop.

4. Gas flow rate has no influence on the Fluent prediction with regard to the experimental data.

Results for the non-uniform inlet distribution are shown in Table 6.4 and Figure 6.4, with the following conclusions:

1. At low liquid flow rates, the pressure drop predicted by Fluent is equal or

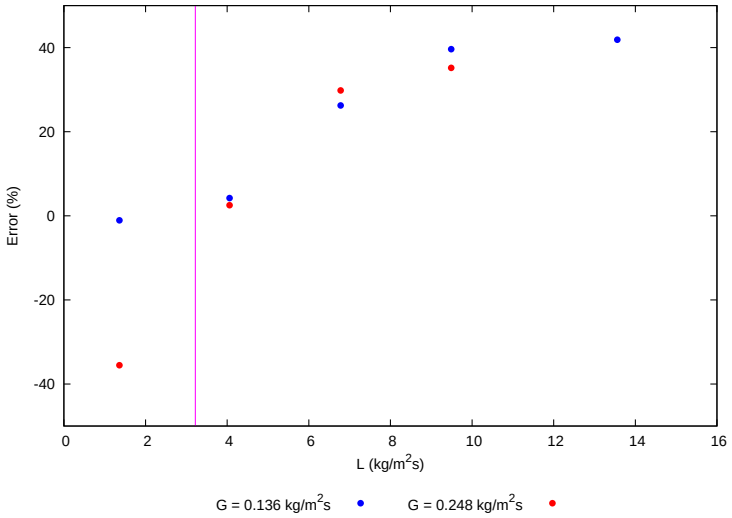

Figure 6.5: Comparison between simulations and experimental data for a uniform inlet distribution and operation point of the reactor

lower than the experimental one, increasing the error as the gas flow rate increases.

2. At intermediate liquid flow rates, Fluent reproduces accurately the experimental data, with errors around 10 %.

3. At high liquid flow rates, Fluent overestimates the pressure drop.

4. Gas flow rate has influence on the Fluent prediction with regard to the experimental data only for low liquid flow rates.

The main interest of this part of the study is to know the degree of accuracy with which Fluent can predict the flow behavior in the reactor beds. The reactor operates with a liquid surface flow rate of 3.22 kg/m^2s and a gas flow rate of 0.72 kg/m^2s. The operating point is shown in Figure 6.5, along with the results for the non-uniform distribution, which is the important one with regard to the real reactor. As it can be seen in Figure 6.5, the reactor operates with a liquid surface flow rate near the zone in which Fluent predicts correctly the pressure drop, but with a higher gas flow rate of the one which has been simulated, which introduces a degree of uncertainty.

6.4 Case C: Two-phase flow dispersion validation

The validation of the results obtained with both Fluent and MFS for the flow dispersion is the aim of this section. The results are compared to both the experimental and numerical results obtained by Boyer et al. [13], who studied two-phase flow dispersion in a cylindrical vertical column filled with spherical glass particles, as described in chapter 3.

6.4.1 Fluent results

As an example, Figure 6.6.a shows the contours of the liquid fraction predicted by Fluent using the average porosity. Figure 6.6.b shows a comparison between the experimental and numerical results obtained by Boyer et al. [13] and the results obtained with the *Porous media model*. The plotted lines correspond to a value of liquid volume fraction of 0.12. It must be noted that the liquid is injected at the center ($r < 4$ *mm*) of the top of the bed ($z = 1.8$ *mm*). As it can be seen in Figure 6.6, the liquid spreading in the considered conditions predicted by the *Porous media model* is clearly below the expected. In addition to it, liquid spreading is not sensitive to the porosity value, since simulations with the average and the minimum porosity values yield results with no significant difference.

As it is shown in Figure 6.6.b, the *Porous media model* available in Fluent, by default, is not able to accurately reproduce the experimental results of Boyer et al. [13]. As it is suggested in the model described by Jiang et al. [7, 8] and used in the simulations presented by Boyer et al. [13], a capillary pressure term is added, through a *User Defined Function*, to the momentum equations as an additional term to increase flow dispersion. Two cases are simulated with different capillarity pressure models, proposed by Attou and Ferschneider (Eq.4.8) and Grosser et al. (Eq.4.12). The effect of the addition of the capillary term (using that of Eq. 4.8) on the liquid distribution is shown in Figure 6.7. The results obtained using Eq. 4.12 are not significatively different to the ones shown in Figure 6.7, so they are not shown. As it can be seen, the model with the capillarity term added predicts approximately the same liquid spreading as the default *Porous media model* and it does not provide a significant improvement on the radial dispersion. The irregularity which can be observed at $z = 1.4$ *m* in the lines representing the liquid

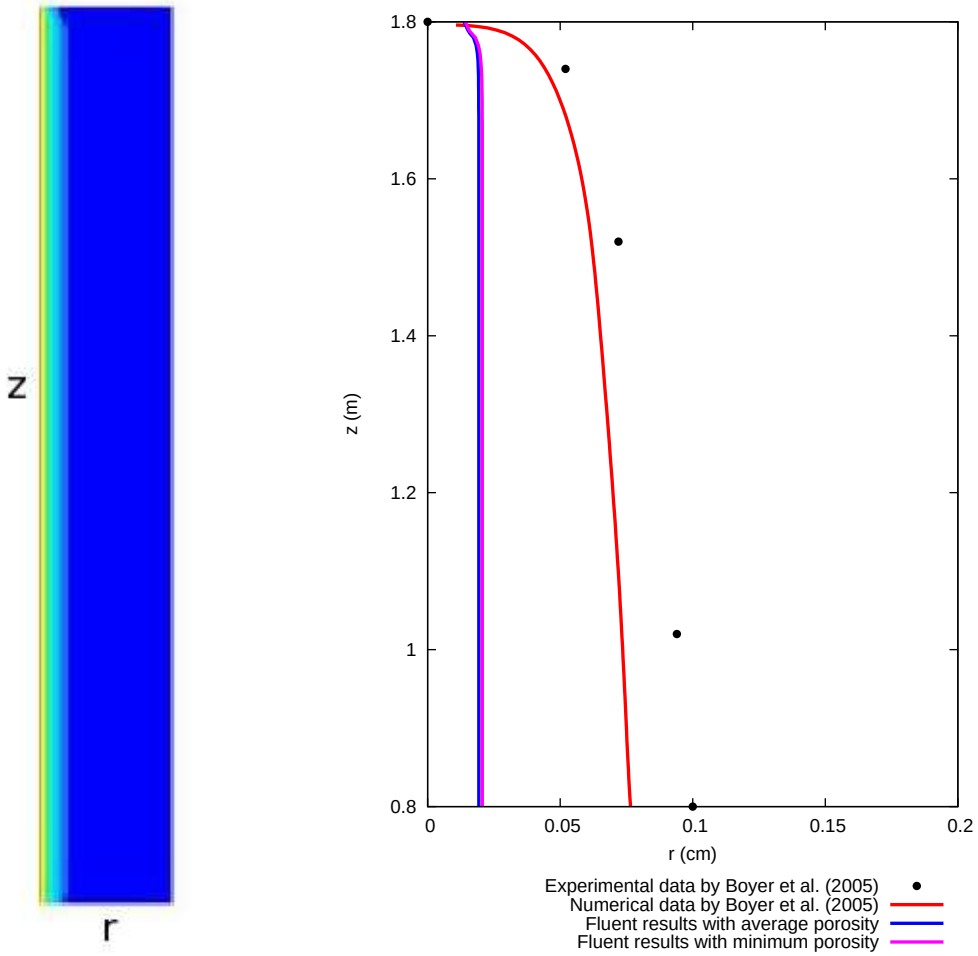

(a) (b)

Figure 6.6: (a) Contours of liquid volume fraction in an r-z plane of the bed predicted by Fluent for the case of average porosity. (b) Contours of liquid volume fraction 0.12 for different cases.

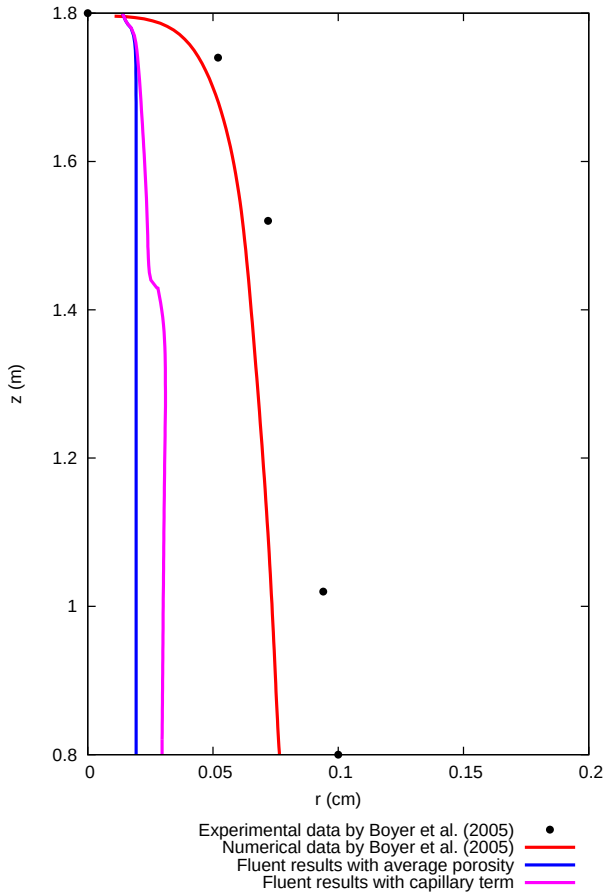

Figure 6.7: Contours of liquid volume fraction of value 0.12 in an r-z plane of the bed. Effect of the addtion of the capillary pressure term proposed by Attou and Ferschneider [23]

distribution with the added capillarity pressure term can be associated with convergence difficulties.

Figure 6.8 shows global views of the liquid volume fraction distribution prediction in the bed using the *Porous media model* (Figure 6.8.a) and the model with the added capillarity pressure term using Eq. 4.8 (Figure 6.8.b) and using Eq. 4.12 (Figure 6.8.c). It can be observed that the *Porous media model* modified with the addition of the capillarity pressure term is closer to the numerical results presented by Boyer et al. [13], although the predicted liquid spreading is smaller. It can be concluded that, for the conditions considered in the simulations, the *Porous media model* is not suitable to predict liquid spreading even with the addition of a capillarity pressure term to the momentum equations.

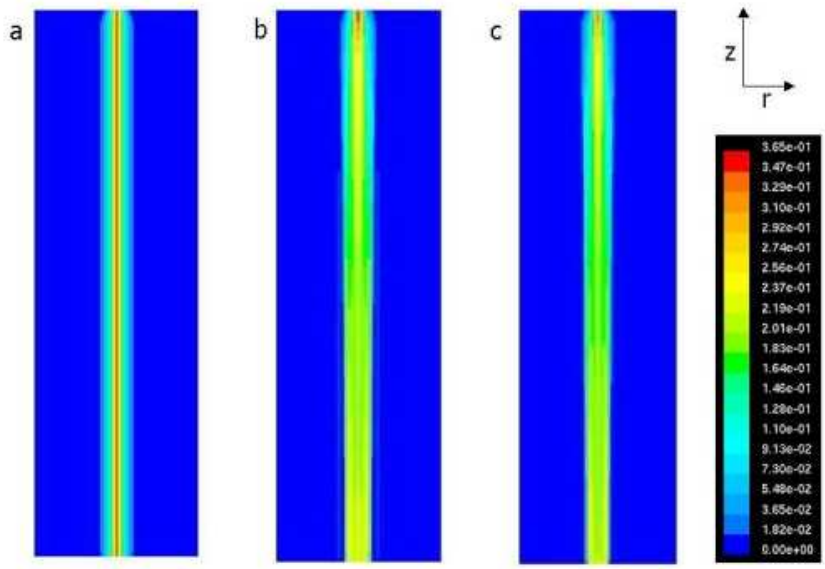

Figure 6.8: Liquid volume fraction contours. Effect of the addition of the capillary pressure term. Comparison between (a) the default *Porous media model*, (b) added capillary pressure term according to the model of Attou and Ferschneider [23] and (c) added capillary pressure term according to the model of Grosser et al. [25]

In the simulations using the *Eulerian granular phase model*, the fluid-particle interaction is modified through drag coefficients according to the model proposed by Holub [9]. The interaction among phases is modelled assuming that the drag force (F_{Dks}), which must be included in the corresponding momentum equations for each phase, can be expressed as,

$$F_{Dks} = \theta_k \theta_s K_{ks} \left(u_k - u_s\right) \tag{6.4}$$

where the drag coefficient, K_{ks}, was already defined in chapter 4.

Figure 6.9 shows the liquid volume fraction contours for the *Eulerian granular phase model* results and the comparison with the experimental and numerical results of Boyer et al. [13]. As it can be seen in Figure 6.9, the *Eulerian granular phase model* reproduces reasonably well the experimental data near the bed outlet, although at the bed inlet, the model overpredicts the liquid dispersion, which reaches a developed flow condition at $z > 1.7m$. Considering the limitations of the *Porous media model* described before, the *Eulerian granular model* is the one used

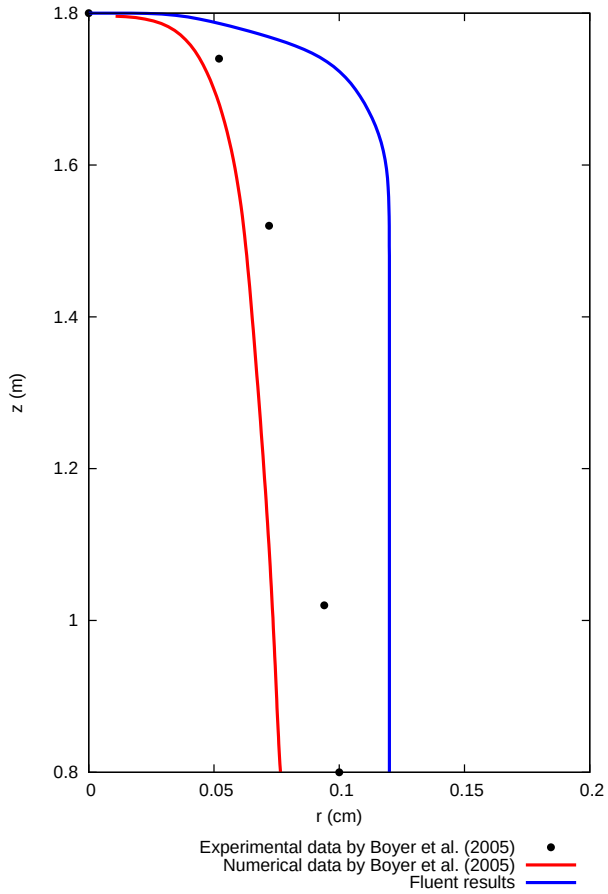

Figure 6.9: Contours of liquid volume fraction of value 0.12 in an r-z plane of the bed.

for the rest of the cases.

6.4.2 MFS results

A first version of MFS, which does not feature the convective terms linearization, is used for this case. Due to stability problems, before applying the aforementioned linearization, the operating conditions are smoothened, as shown in Table 6.5. It can be seen in Table 6.5 that the velocities are lowered significatively, specially for the liquid (from 0.7 to 0.01 m/s) but also for the gas (from 0.1 to 0.01 m/s). The x-direction drag terms have not been included and the capillary pressure term has been decreased by five orders of magnitude.

Figure 6.10 shows the liquid volume fraction contours. The left boundary is the

Table 6.5: Water-air system characteristics.

Parameter	Smoothened case	Original case
Porosity	0.365	0.365
v_l (x $<$ 4 mm)	0.01 m/s	0.7 m/s
v_g (4 mm $<$ x $<$ 200 mm)	0.01 m/s	0.1 m/s
ρ_l	10^3 kg/m^3	10^3 kg/m^3
ρ_g	1 kg/m^3	1 kg/m^3
Drag in the x direction	No	Yes
Drag in the y-direction	Yes	Yes
Capillary pressure	Multiplied by 10^{-5}	Yes

center of the column (symmetry axis) while the right boundary is the wall. As it can be seen, the results are physically consistent, more than those provided by Fluent. The liquid radial dispersion occurs continuously. However, this dispersion is not large, due to the low velocities from both phases.

When entering the real velocities for the case to validate (see Table 6.5), the drag in the x-direction or the non-smoothened capillarity, stability problems arise, due to the large difference between both phases densities. Applying the convective terms linearization the code gains stability, but the convergence criteria are not met. After realizing that a large difference in densities creates stability problems in the code, it is decided to test it with the hydrodesulfurization reactor conditions (physical properties and inlet velocities). The difference in densities is significatively smaller than in the water-air system, as shown Table 6.6, where the operating conditions for this simulation are summarized. The computational domain is the same that the one used for the water-air system. The velocities are an average of the ones obtained in the simulations of the region placed between the distribution tray and the first bed of the reactor, previously described in chapter 2.

This time, all the drag and capillarity terms are entered in the simulation. As opposed to the work of Boyer et al. [13], the capillarity term is not modified. The code, even without the convective terms linearization, is stable for these conditions, which confirms that instabilities are generated by the large difference between phases densities, being the densities ratio of 1000 to 1 for the case of the water-air system and approximately 30 to 1 for the reactor case.

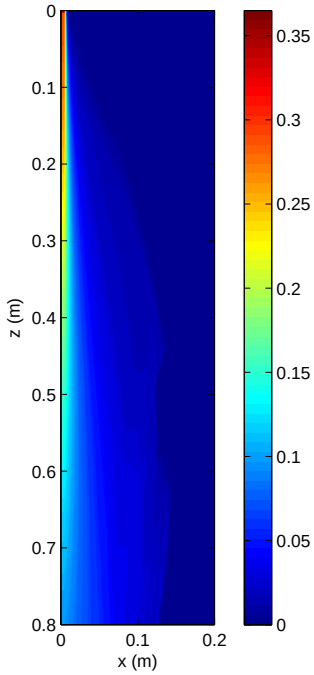

Figure 6.10: Contours of liquid volume fraction for smooth inlet conditions.

Table 6.6: Reactor system characteristics in a bed of constant porosity.

Porosity	0.365
v_l (x $<$ 4 mm)	0.22 m/s
v_g (4 mm $<$ x $<$ 200 mm)	$2.8{\cdot}10^{-3}$ m/s
ρ_l	611 kg/m^3
ρ_g	20.8 kg/m^3
Drag in x-direction	Yes
Drag in y-direction	Yes
Capillarity	Yes

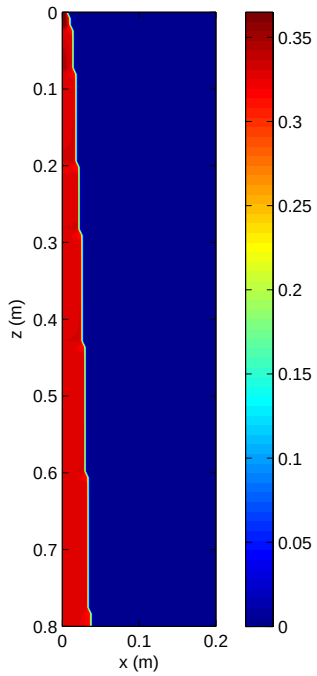

Figure 6.11: Contours of liquid volume fraction obtained with MFS.

Figure 6.11 shows liquid volume fraction contours. As it can be seen, despite the non-fully converged results for the fields shown, the results are physically consistent, showing the tendency of continuous liquid radial spreading.

6.5 Case D: Two-phase flow dispersion with a porosity change

Figure 6.12 shows the comparison of relative liquid volume fraction for neighboring beds with different porosity. The left image displays the results provided by Fluent, where it can be seen a liquid reconcentration when the flow goes from the top less porous to the bottom bed with larger porosity, which lacks physical meaning. On the other hand, MFS is able to yield results which are physically consistent, as shown in the right image. As it can be seen, there is no liquid reconcentration in the bottom bed, as the liquid distribution through the bed does not change significatively from the one at the exit of the first bed.

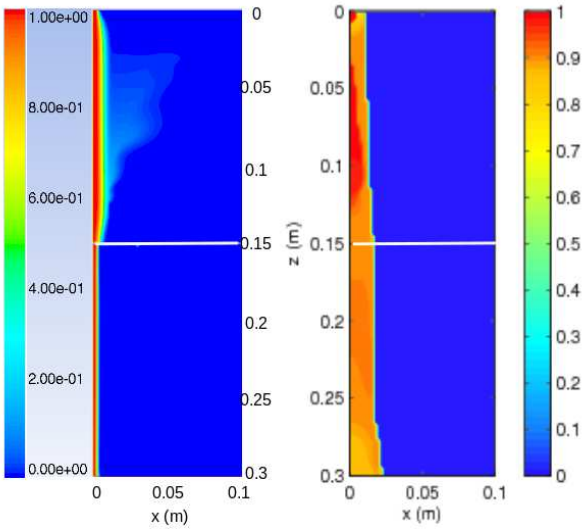

Figure 6.12: Relative liquid volume fraction contours obtained with Fluent (left) and MFS (right).

6.6 Case E: Two-phase flow dispersion in the central region of the reactor

Figure 6.13 shows the liquid distribution in the central region of the reactor, by displaying an iso-surface of liquid volume fraction of 0.10. The circular region at the top of the bed represents one chimney's projection and the arrow shows the inlet direction of the gas in the chimney. As it can be seen in Figure 6.13, the liquid distribution does not change significatively as the flow descends except for the top of the first bed, the third bed and the interphase of different beds. This change in the liquid distribution in the interphase between two beds is in agreement with their different porosity. For example, it can be seen in Figure 6.14 that the liquid is more dispersed in the first bed, of lower porosity ($\varepsilon = 0.33$, Figure 6.14.a), while it is more concentrated in the second bed, in which porosity is 0.53 (Figure 6.14.b). The same reasoning can be applied to Figures 6.14.c and 6.14.d, which show the third ($\varepsilon = 0.45$) and fourth ($\varepsilon = 0.40$) beds, respectively.

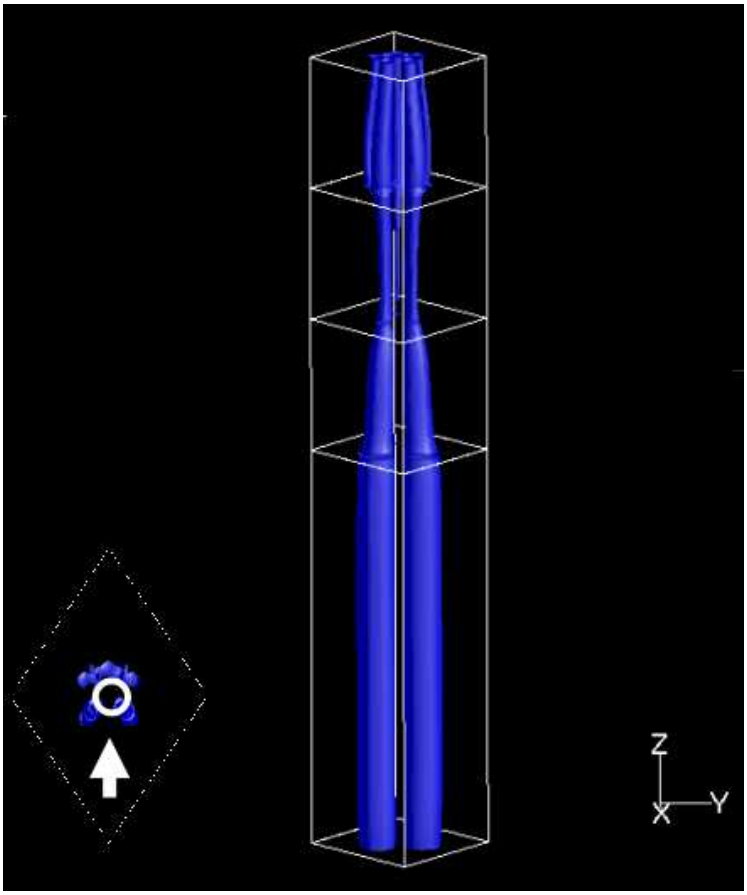

Figure 6.13: Liquid distribution in the area surrounding a central region chimney.

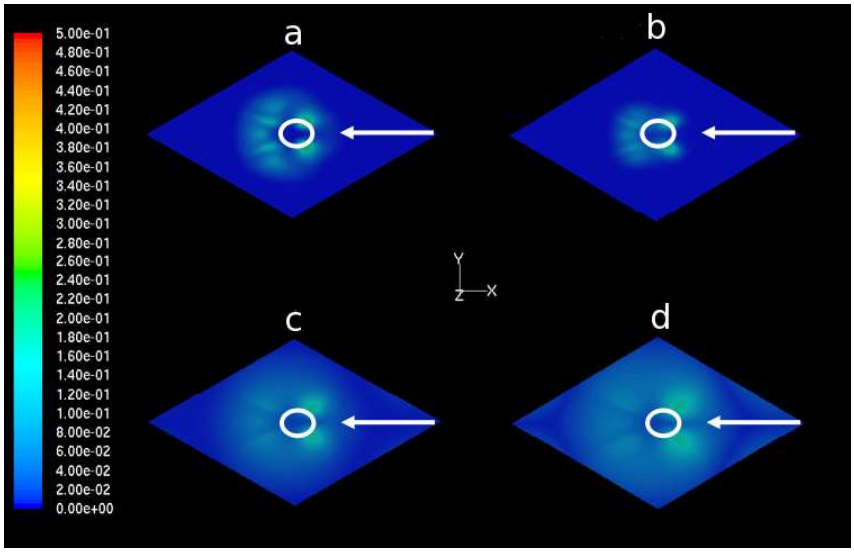

Figure 6.14: Liquid volume fraction contours at horizontal slices in the different beds for the central region. The slices are placed 75 mm below each bed inlet.

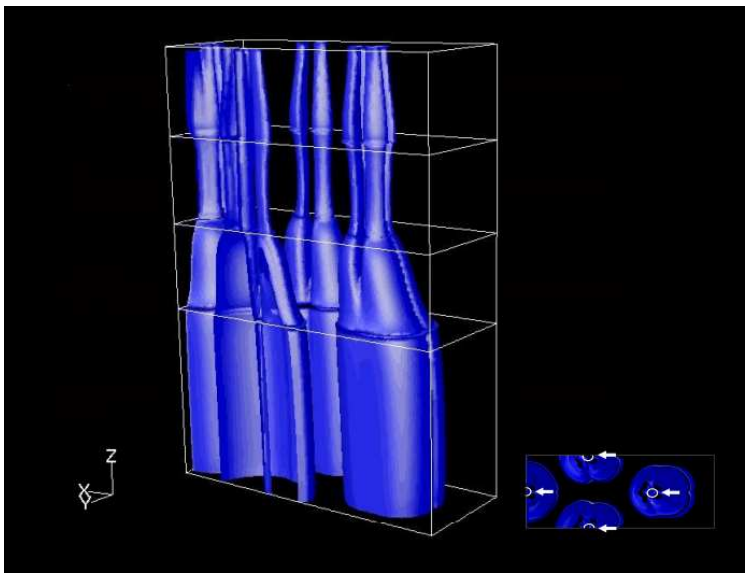

Figure 6.15: Liquid distribution in the area surrounding a near-wall region chimney.

6.7 Case F: Two-phase flow dispersion in the near-wall region of the reactor

Liquid distribution in the near-wall region is shown in Figure 6.15, as an isosurface of liquid volume fraction of 0.10. The circular regions shown at the top of the bed represent the projections of the chimneys placed above, while the arrows show the gas inlet direction into the chimney. As it has been previously seen in the case of the flow under a chimney placed at the central region of the reactor, the liquid distribution does not change significatively as the flow descends through the beds, except for the third bed in this case, where a flow attachment to the wall is suggested. This can be observed in the inclination towards the wall of the isosurface shown. However, this effect will be discussed in more detail later in section 6.8. The effect of the different porosity in the beds can be observed in Figure 6.16 which shows liquid volume fraction contours at four horizontal slices of the beds. As it can be seen in Figure 6.16, lower porosity beds show a more dispersed liquid than those of larger porosity. For example, liquid is more dispersed in the first bed (Figure 6.16.a, $\varepsilon = 0.33$) than in the second one (Figure 6.16.b, $\varepsilon = 0.53$). Figures 6.16.c and 6.16.d show a liquid more dispersed due to the lower porosity of these beds, 0.45 and 0.40 respectively, in comparison with the second bed.

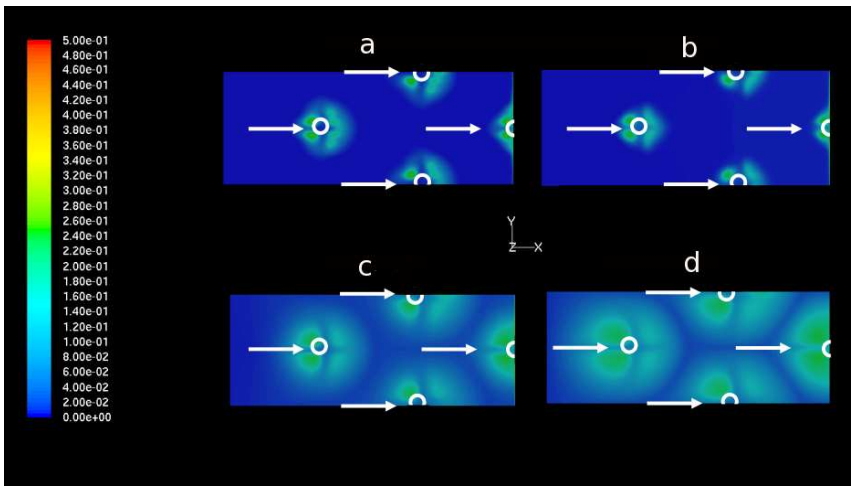

Figure 6.16: Liquid volume fraction contours at horizontal slices in the different beds for the near-wall region. The slices are placed 75 mm below each bed inlet.

6.8 Case G: Effect of the wall on the two-phase flow distribution along the reactor

Since the previous near-wall region simulation hinted at a tendency of the flow to attach the wall of the reactor as it descended through the beds, a study of that effect was carried out in more detail. Due to the nature of this case, calculations are carried out in sections, since simulating the whole reactor would result in a very large number of cells and an extremely high computational cost. The first 11 m of the reactor have been simulated, since it is considered that this is enough to appreciate any possible wall effect on the flow behavior.

6.8.1 Numerical procedure and optimization

As shown in Figure 6.17, the reactor has been divided in sections which are 15 cm deep, where the volume fractions and velocities distribution results at the outlet in each of these sections are taken as the inlet conditions of the following section. This contributes to speed up calculations, although, due to the large number of simulations needed to obtain meaningful results of the flow distribution through the reactor, time for calculations is also large. To avoid a possible distortion in the results caused by the outlet boundary condition, which seems to have an influence at the exit zone in each simulation, it has been decided to simulate sections 20 cm

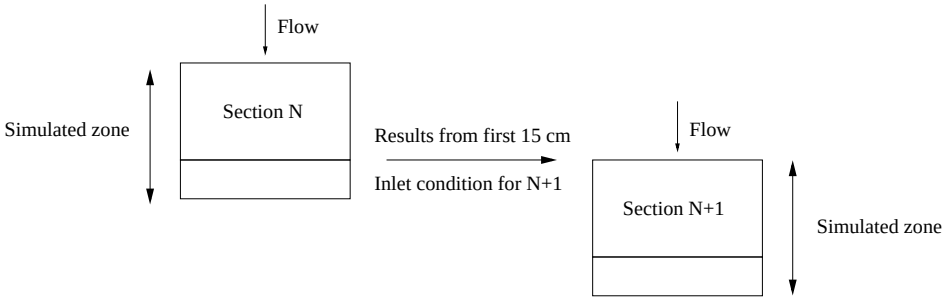

Figure 6.17: Sketch of the simulation procedure in sections.

Table 6.7: Simulation time comparison

Simulated section depth (*cm*)	10	20
Real section depth (*cm*)	5	15
Number of cells	1244720	2489440
Time per iteration ($min/iteration$)	2.97	5.72

deep but taking only the first 15 cm as valid.

Simulations varying the section depths were carried out to optimize the calculation time. Table 6.7 shows the comparison of the studied cases. It can be seen that simulating a thickness of 15 cm of the reactor instead of 5 cm produces a speed up factor of $\frac{15}{5}\frac{2.97}{5.72} = 1.56$. In order to speed up calculations even more, two processors were working in parallel. Table 6.8 shows the comparison between the serial and parallel computations. It can be seen that Fluent parallelizes in a very efficient manner the simulation with two processors, with a speed up factor of 2. The overall improvement factor in the computation efficiency, using two processors working in parallel and simulating 15-cm sections (real depth) is 3.12.

Table 6.8: Parallel computation

Number of processors	1	2
Real section depth (*cm*)	15	15
Number of cells	2489440	2489440
Time per iteration ($min/iteration$)	5.72	2.86

6.8.2 Liquid volume fraction

Figure 6.18 shows a liquid volume fraction isosurface of 0.10. It can be observed that the liquid spreads slowly in the radial direction, reaching a more uniform distribution in the central zone than in the near-wall zone. It should be noted that the isosurface shown provides only a partial information of what is really happening in the reactor. In order to obtain a more detailed view of the distribution of the liquid fraction, it is required to resort to liquid volume fraction contours and profiles at different reactor depths.

Figures 6.19 to 6.21 show liquid volume fraction contours at different depths. The red color represents liquid and the blue color gas, with the color gradation representing different values of liquid volume fraction according to the color scale shown at the left side of the contours. It can be seen that, as the flow descends through the reactor beds the liquid spreads radially improving phase distribution. While not perfectly uniformly distributed, from a depth of 8 m on the liquid is under a reasonably good distribution. This is seen in a more detailed manner in the volume fraction profiles shown next.

Two different planes have been chosen to show the liquid volume fraction profiles. The first of these planes is marked with a line in Figure 6.22. Figures 6.23 to 6.25 show the liquid volume fraction profiles at different reactor depths in the aforementioned plane. The reactor radius is shown on the horizontal axis while the liquid volume fraction is shown in the vertical axis. It can be seen in these figures, in the region close to the inlet, around the first 3 m, that the liquid volume fraction decreases faster in the chimneys placed near the wall than in the central ones. In other words, chimneys which are close to the wall spread the liquid radially faster than those in the central region of the reactor. This phenomenon balances between 3 m and 5 m of the reactor. From that depth on, the central chimneys start spreading faster than those near the wall. It can be seen, for a depth of 11 m, that in the first 0.3 m in radial direction the liquid distribution is uniform. Figure 6.26 shows simultaneously liquid volume fraction profiles at different depths.

The second plane chosen to show these profiles is the one shown in Figure 6.27. Figures 6.28 to 6.30 show liquid volume fraction profiles at different reactor depths.

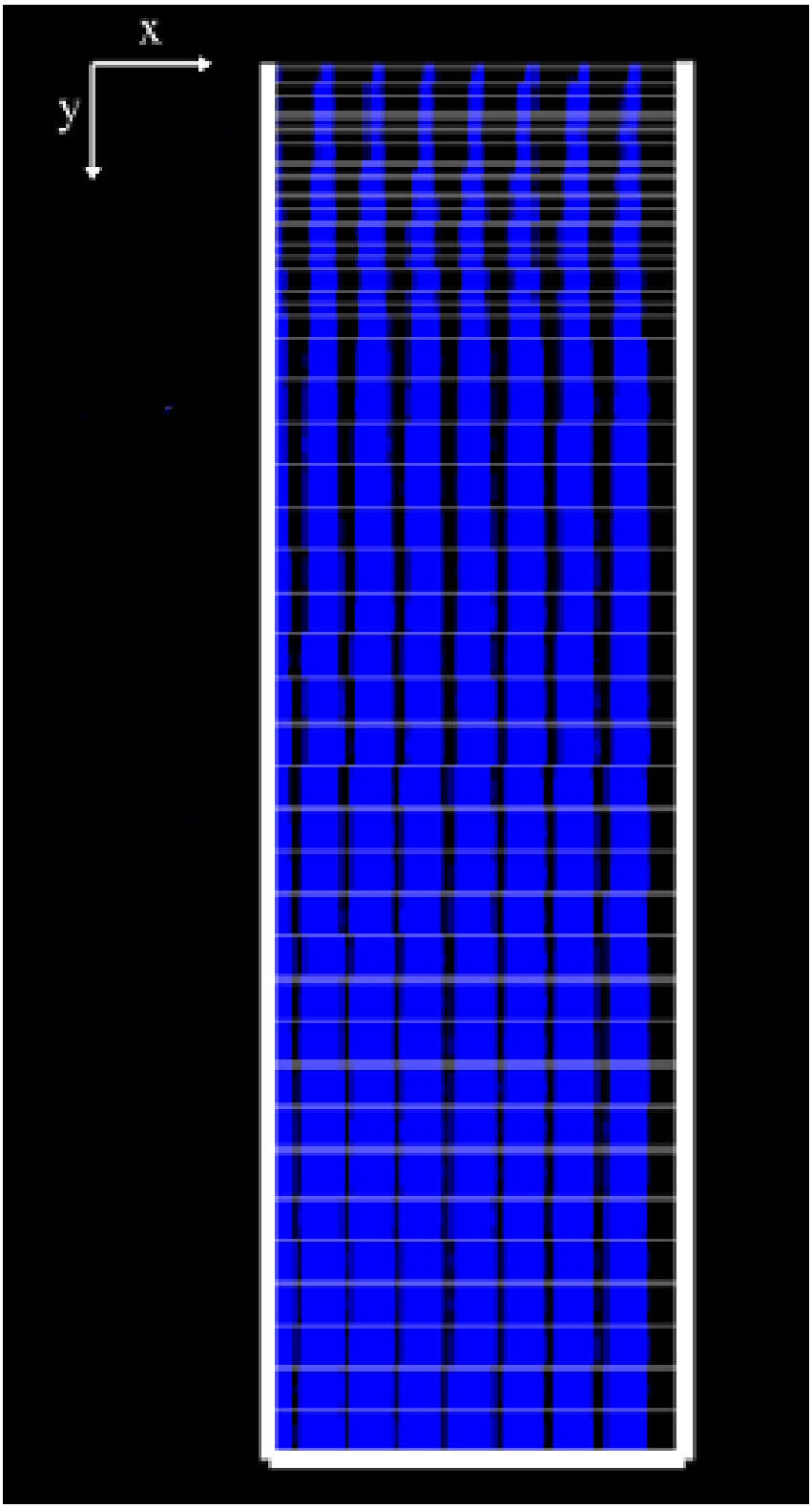

Figure 6.18: Liquid volume fraction isosurface of 0.10.

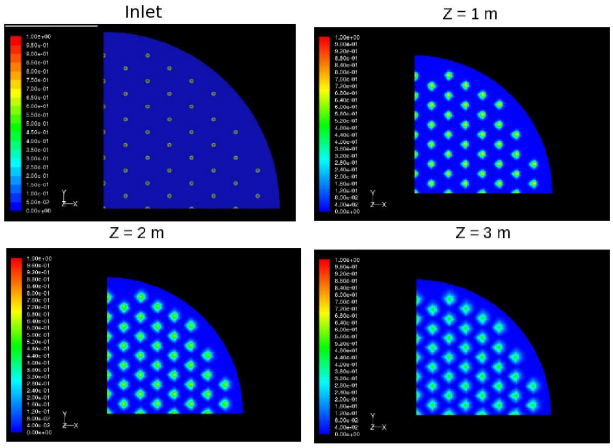

Figure 6.19: Liquid volume fraction contours. Slices at 0 m, 1 m, 2 m and 3 m.

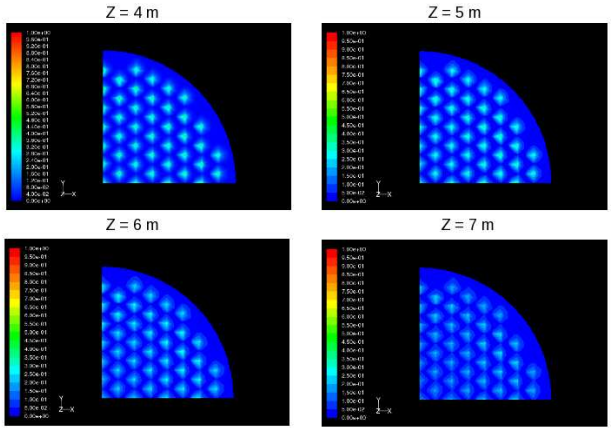

Figure 6.20: Liquid volume fraction contours. Slices at 4 m, 5 m, 6 m and 7 m.

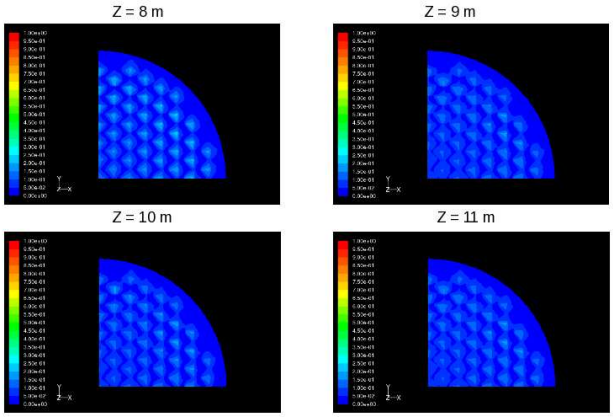

Figure 6.21: Liquid volume fraction contours. Slices at 8 m, 9 m, 10 m and 11 m.

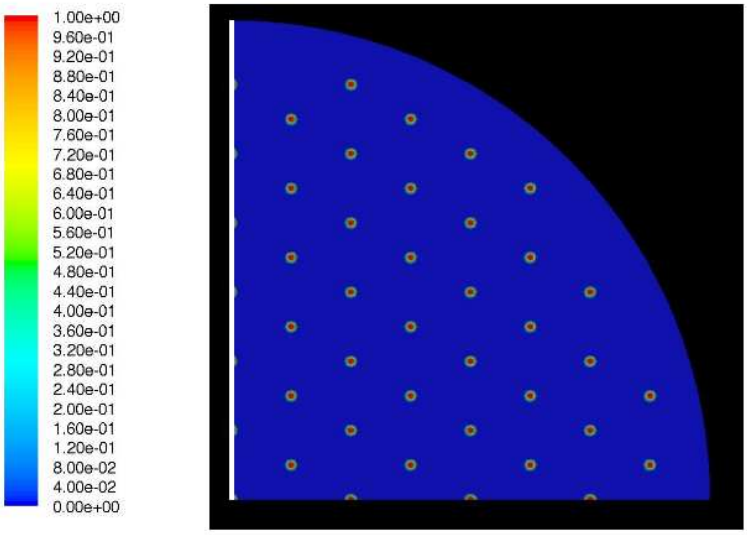

Figure 6.22: Plane on the symmetry axis chosen to show the liquid volume fraction profiles.

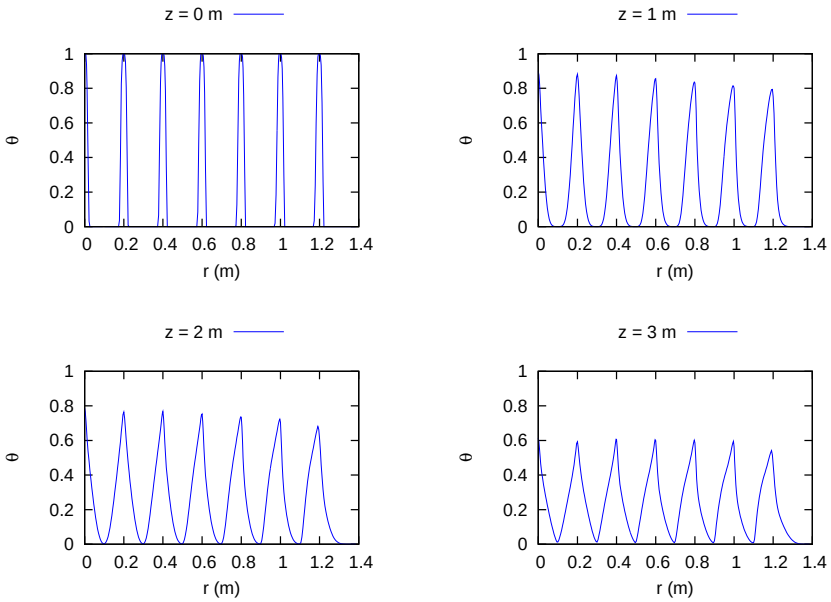

Figure 6.23: Liquid volume fraction profiles in the plane shown Figure 6.22. Slices at 0 m, 1 m, 2 m and 3 m.

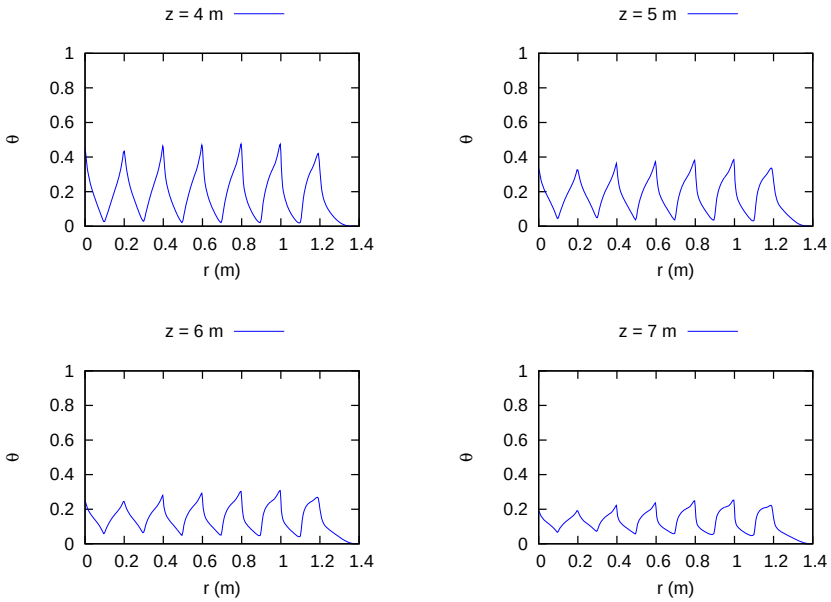

Figure 6.24: Liquid volume fraction profiles in the plane shown Figure 6.22. Slices at 4 m, 5 m, 6 m and 7 m.

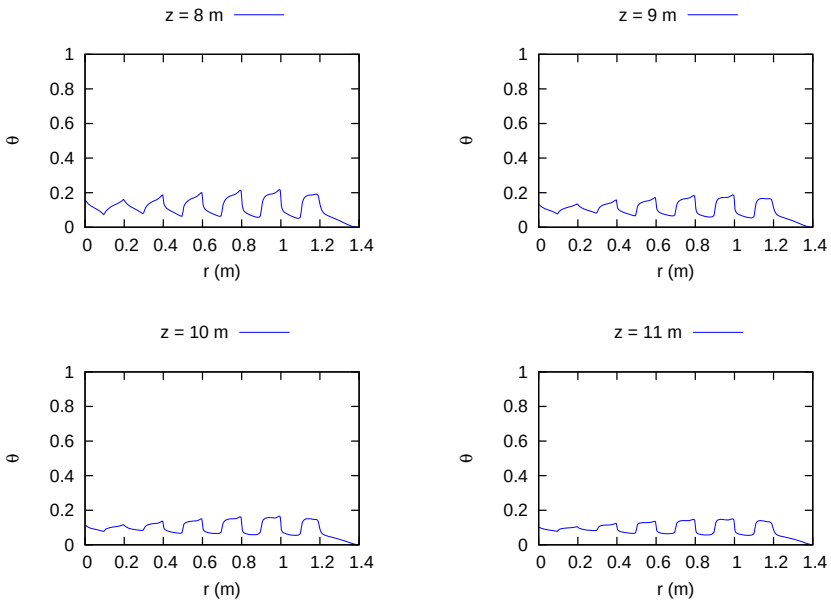

Figure 6.25: Liquid volume fraction profiles in the plane shown Figure 6.22. Slices at 8 m, 9 m, 10 m and 11 m.

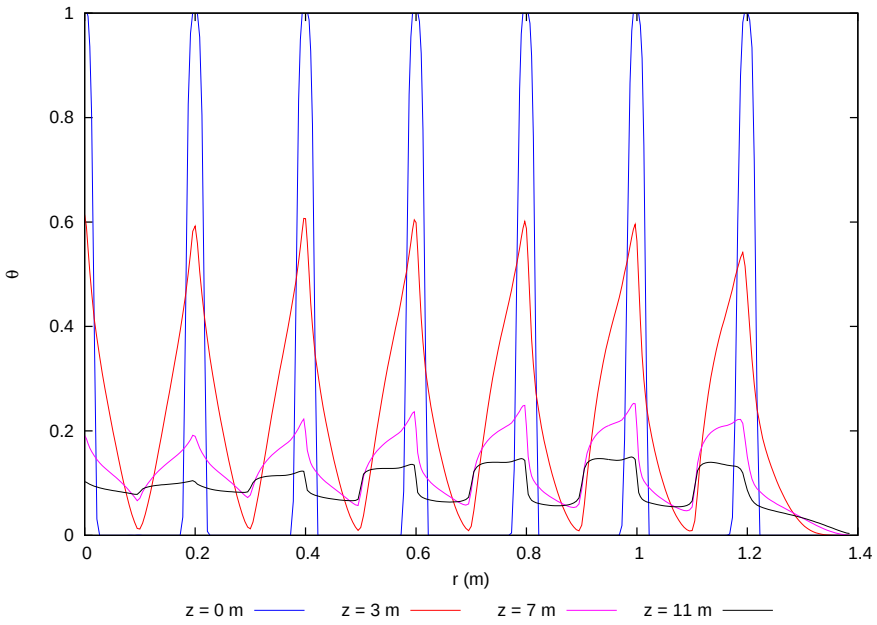

Figure 6.26: Liquid volume fraction profiles in the plane shown Figure 6.22. Slices at 0 m, 3 m, 7 m and 11 m.

As it can be seen, the results obtained are similar to those seen in the other plane. Figure 6.31 shows simultaneously liquid volume fraction profiles at different depths.

A characteristic of the liquid distribution worth mentioning is the lack of symmetry in the plumes as the flow descends through the reactor beds. As it can be seen in Figures 6.23 to 6.26 and Figures 6.28 to 6.31, the plume region close to the wall is narrower than the plume region close to the center of the reactor, or in other words, there is a suction effect on the flow from the central zone of the reactor, which is explained in the following subsection.

6.8.3 Liquid velocity

Figures 6.32 and 6.33 show the liquid axial velocity profiles, at different depths, for the planes shown in Figures 6.22 and 6.27, respectively. As it can be seen in these figures, liquid descends with higher velocity through the central zone of the reactor than in the near-wall region. This would explain the effect of liquid displacement towards the central region of the reactor, previously commented, resulting in a better liquid distribution in this region of the reactor. As the flow descends faster in the center, the liquid in the surrounding plumes is allowed to preferentially move

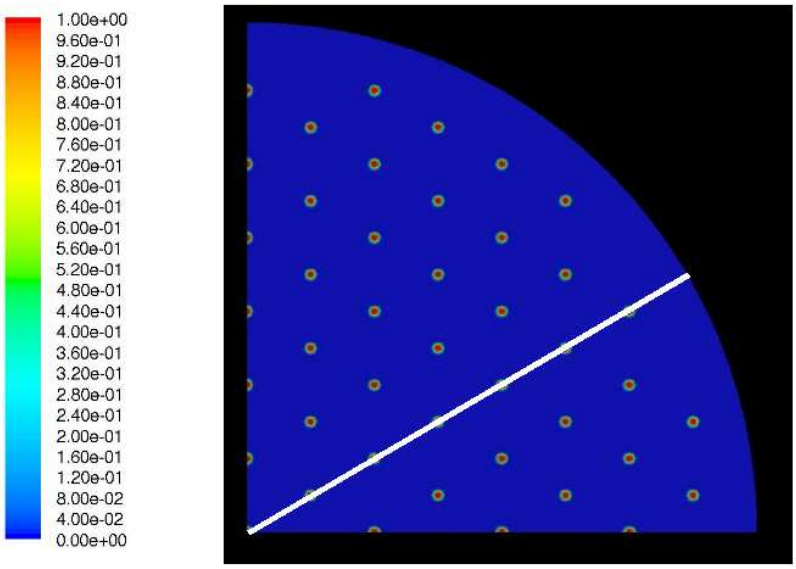

Figure 6.27: Plane chosen to show the liquid volume fraction profiles.

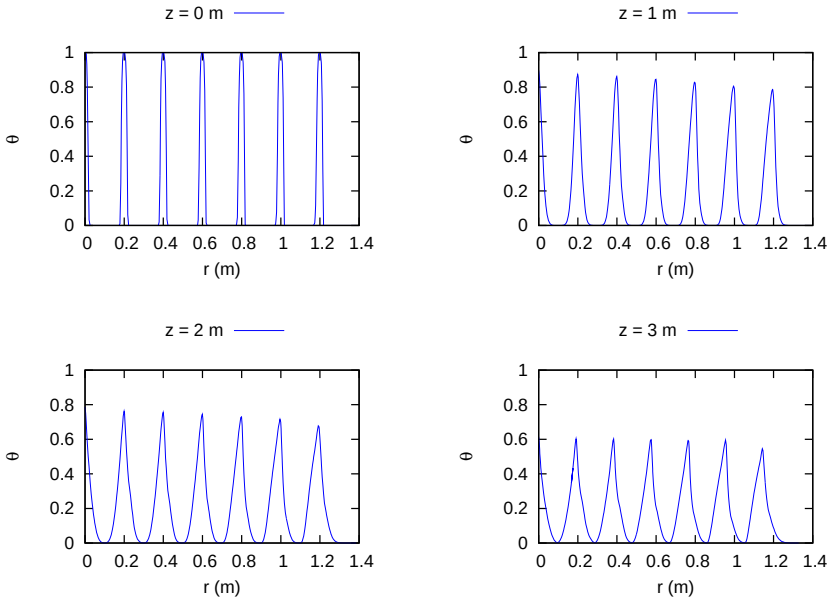

Figure 6.28: Liquid volume fraction profiles in the plane shown Figure 6.27. Slices at 0 m, 1 m, 2 m and 3 m.

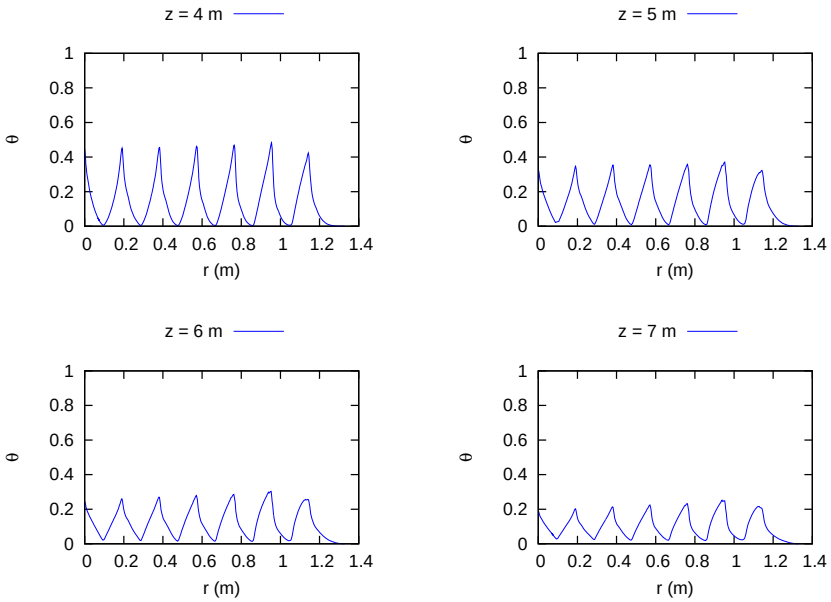

Figure 6.29: Liquid volume fraction profiles in the plane shown Figure 6.27. Slices at 4 m, 5 m, 6 m and 7 m.

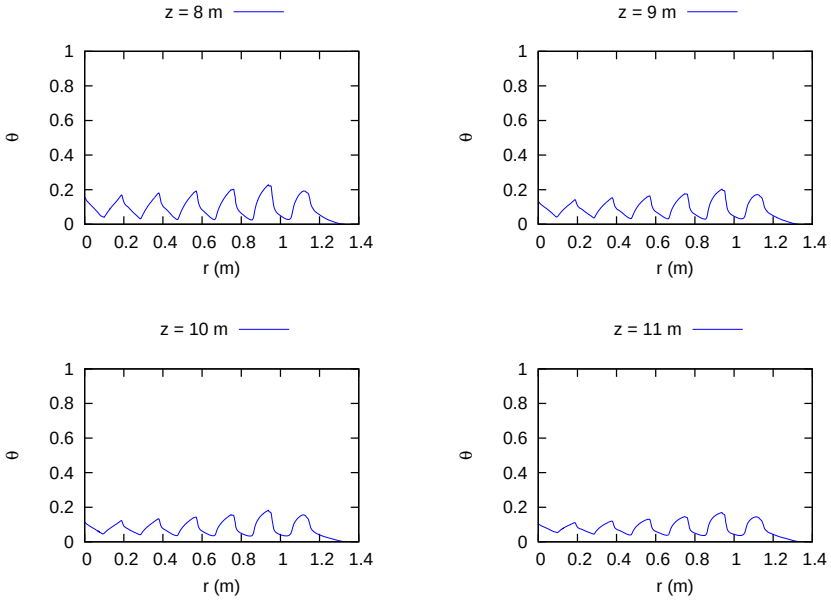

Figure 6.30: Liquid volume fraction profiles in the plane shown Figure 6.27. Slices at 8 m, 9 m, 10 m and 11 m.

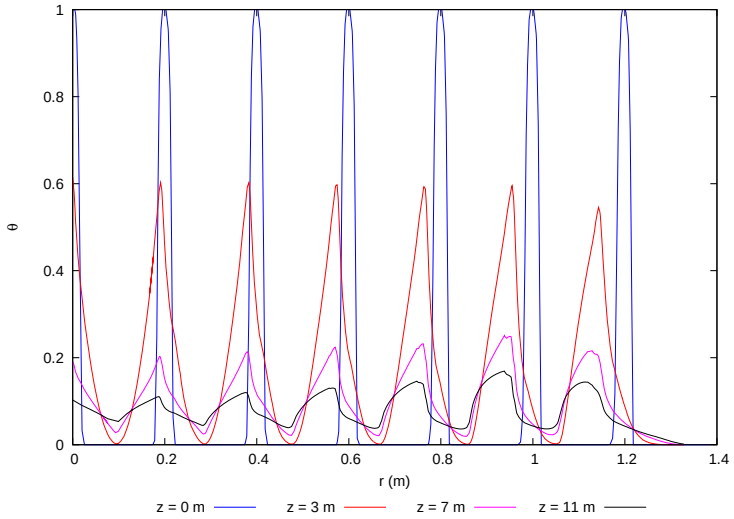

Figure 6.31: Liquid volume fraction profiles in the plane shown Figure 6.27. Slices at 0 m, 3 m, 7 m and 11 m.

towards the center, thus explaining the non-symmetrical liquid plumes descending through the bed.

6.8.4 Evolution of the center of the plumes

Figures 6.34.a and 6.34.b show the evolution of the center of the plumes for the central and near-wall chimneys in the planes shown in Figures 6.22 and 6.27, respectively. The point of maximum liquid volume fraction is considered the center of the plume. The horizontal axis shows the point of maximum liquid volume fraction for the plume, in other words, the center, while the depth of the bed is shown in the vertical axis. As it can be seen, in the first 3 m the plume of the near-wall chimney is displaced faster than the one of the central region, with a change in tendency happening at 5 m. The same phenomenon takes place in both planes, so it is assumed that it happens in the whole reactor. This confirms what the volume fraction profiles suggested, that in the first 3 m the liquid spreads faster in the near-wall region and that tendency changes from a depth of 5 m on, where the liquid spreads faster in the central region.

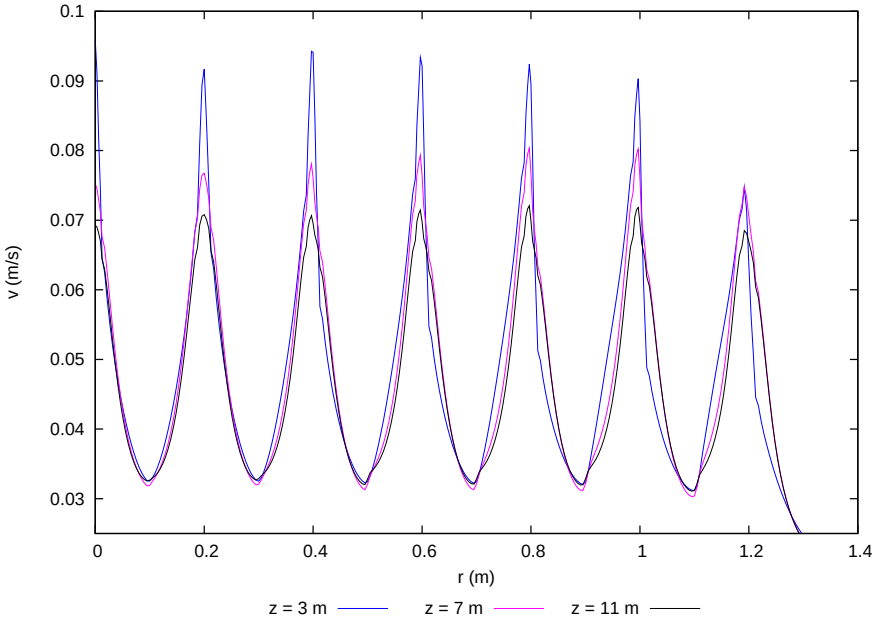

Figure 6.32: Liquid axial velocity profiles in the plane shown in Figure 6.22. Slices at 3 m, 7 m and 11 m.

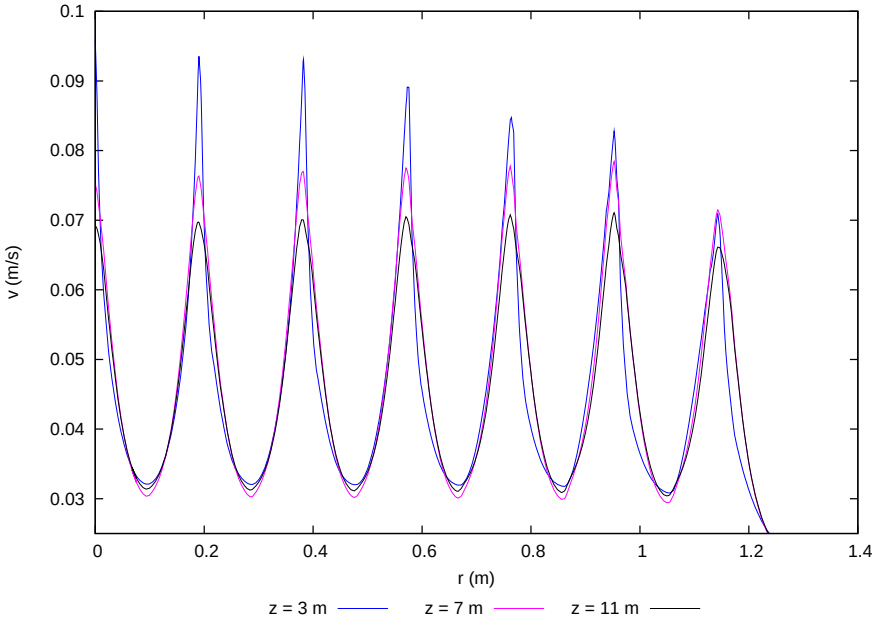

Figure 6.33: Liquid axial velocity profiles in the plane hown in Figure 6.27. Slices at 3 m, 7 m and 11 m.

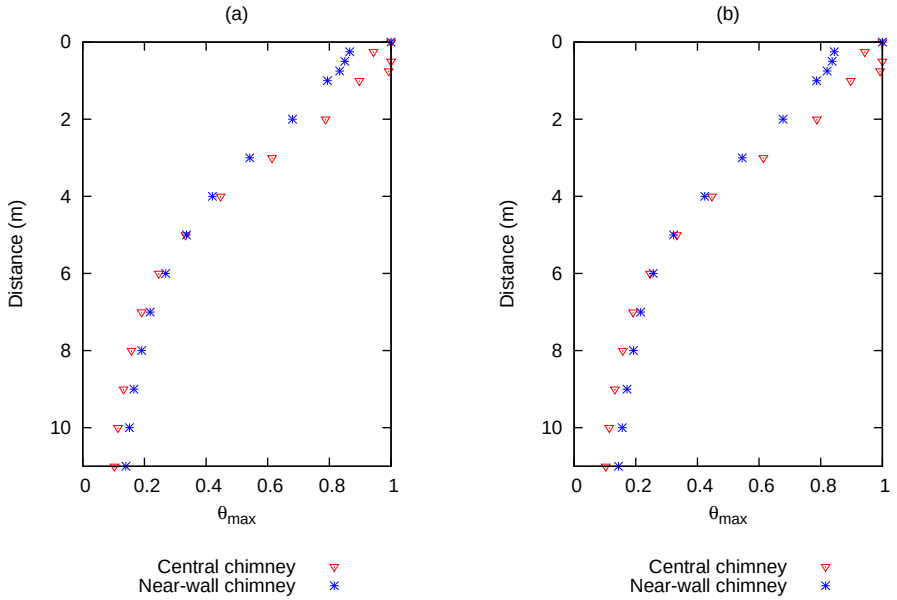

Figure 6.34: Evolution of the center of the plumes for the near-wall and central chimneys. (a) Plane shown in Figure 6.22. (b) Plane shown in Figure 6.27

6.8.5 Half-width

An efficient manner to measure dispersion in porous media is the half-width. The half-width concept is shown in Figure 6.35. In a gaussian distribution, the half-width is defined as the distance that links the two points of value half of the maximum of the distribution at both sides of this maximum. That distance is represented by the red arrow in Figure 6.35. Figures 6.36.a and 6.36.b show the evolution of the half-width along the reactor in the planes shown in Figures 6.22 and 6.27, respectively. As it can be seen, until a depth of 5 m the plume of the near-wall chimney is wider than the central region one. However, from a depth of 6 m on the central plume is clearly wider than the one in the near-wall region. From a depth of 8 m on, it is considered that in the central region the liquid is well enough distributed so there is no need to represent the half-width. This reinforces the idea of a faster dispersion near the wall in the first meters of the reactor and a change of tendency from a depth of 5 m on.

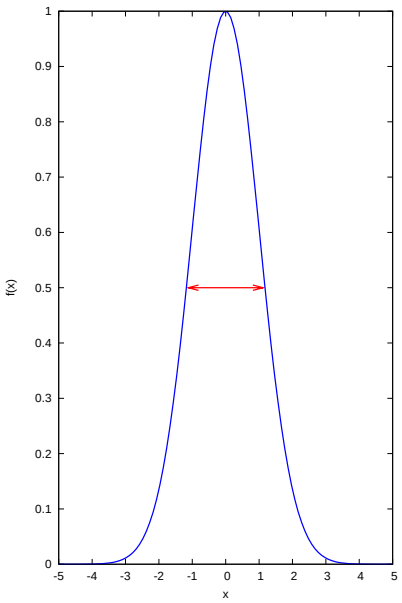

Figure 6.35: Half-width concept

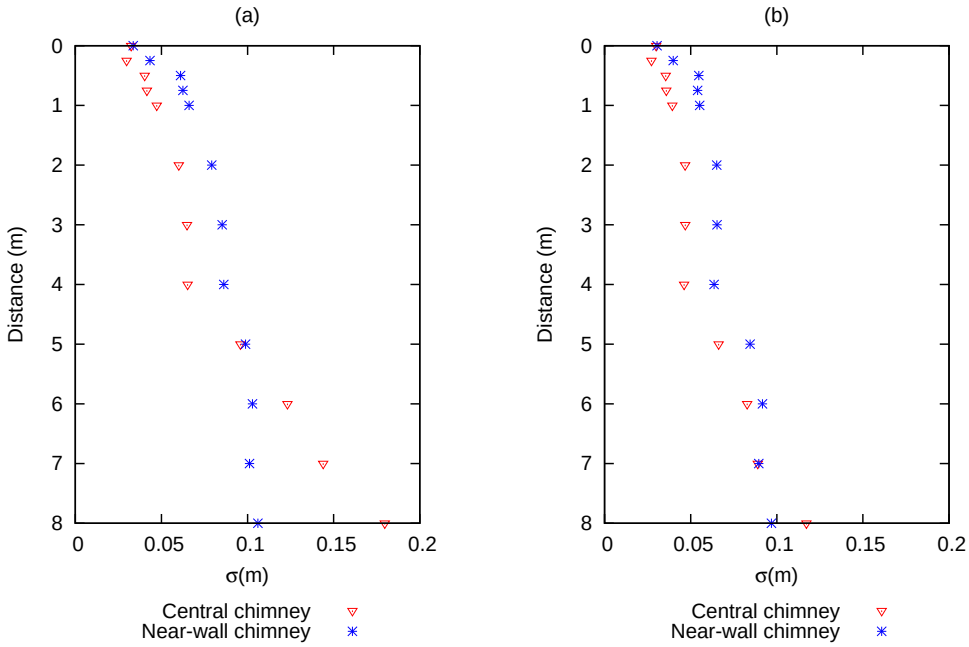

Figure 6.36: Evolution of the half-width for the near-wall and central chimneys. (a) Plane shown in Figure 6.22. (b) Plane shown in Figure 6.27

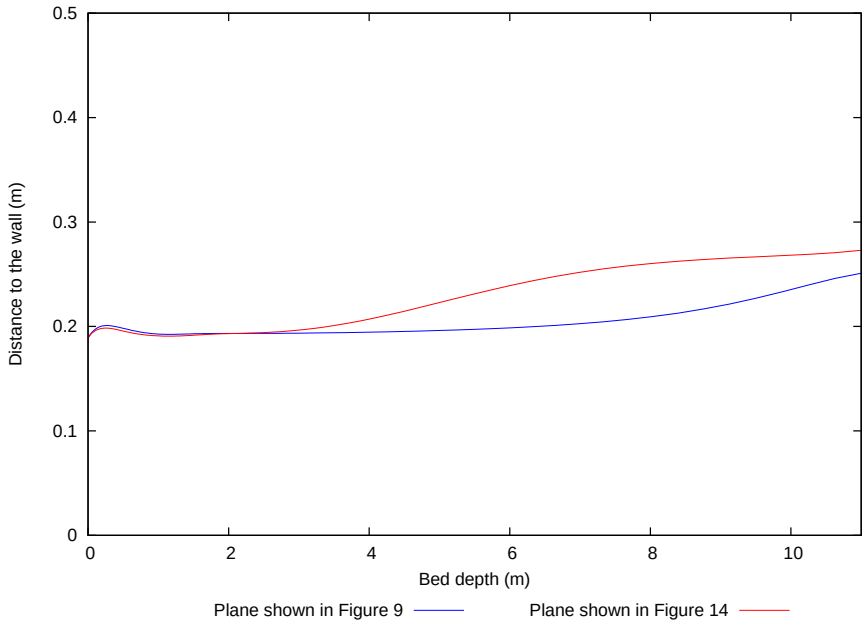

Figure 6.37: Evolution of the distance between the center of the plume of the nearest-wall chimney and the wall.

6.8.6 Distance to the wall

Figure 6.37 shows the distance between the center of the plume which is nearest the wall and the wall in the planes shown in Figures 6.22 and 6.27. As it can be seen, from a depth between 5 m and 6 m, the plume starts to move away from the wall. Thus, any suction effect by the wall is discarded. On the contrary, and as previously discussed, the liquid tends to move towards the center of the reactor.

As it was already reported in section 3.7, the inlet distribution of the phases for this case is not as detailed as it is for case F, and the computational mesh is also coarser. These factors have to be taken into account when drawing conclusions about the wall effect. The results from section 6.7 suggested a tendency of the liquid flow to attach the wall, while the results from this section show that the liquid moves away from the wall from a depth of 5 m on. Case F only studied the first 70 cm of the reactor, while case G studies the first 11 m. Figure 6.38 shows the comparison between cases F and G for the first 70 cm of the reactor, where the distance between the center of the nearest-wall plumes and the wall is plotted against the reactor depth. As it can be seen, at that depth of 70 cm the case G simulation shows no change in the distance between the center of the nearest-wall plume and the wall.

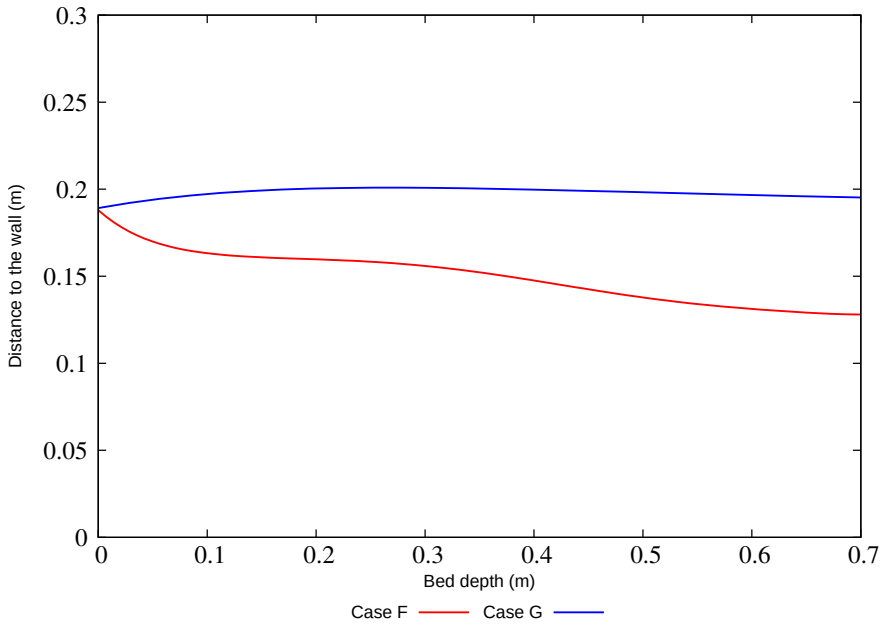

Figure 6.38: Comparison between the evolution of the distance between the center of the plume of the nearest-wall chimney and the wall for cases F and G.

The case F simulation shows an approachment of 6 cm between the center of the plume and the wall, which occurs up until a depth of 55 cm, remaining constant from there on. In case G, the maximum distance that the liquid moves away from the wall is 7 cm at a depth of 11 m. Taking into account those displacements and that the reactor has a diameter of 2.77 m, any wall effect on the two-phase flow can be discarded.

Chapter 7

Conclusions

After all the results obtained, both with the commercial CFD software Fluent and the domestic code MFS, the following conclusions can be drawn:

- There is no need to model turbulence in porous media, as it has no effect on this type of flow for the conditions (liquid velocities up to 2 m/s, gas velocities up to 0.3 m/s, porosities ranging from 0.33 to 0.53) considered as compared to the effect the media has on the flow dispersion. Simulations with and without implementing a turbulence model yielded the same results. This simplifies slightly the already complex modelization of multiphase flows through porous media.

- The widely used commercial CFD software Fluent predicts accurately the macroscopic pressure drop in this type of flows for the operating conditions of interest in this study. However, regarding two-phase flow dispersion in porous media there are two issues which need to be properly solved. The lack of a continuous liquid spreading as the flow descends through a packed bed and the subtle liquid reconcentration when the flow changes from a less porous bed to a more porous one need to be addressed. However, the overall magnitude of the dispersion predicted is in reasonable agreement with experimental data available in the literature, which allowed the software to be used in most cases presented in this PhD thesis. In order to do that, new drag models had to be implemented in Fluent via *User Defined Functions*. The same was done with the capillarity models, but stability problems arose which could not be solved.

- The domestic code developed during the length of this PhD thesis, *Multiphase Flow Solver (MFS)*, yields results which are physically more consistent than those provided by Fluent. MFS is able to predict continuous two-phase flow dispersion through a packed bed and avoids non-physically consistent predictions when dealing with porosity changes. MFS is still on its development stage and it is not a completely finished product yet. Numerical instabilities have yet to be removed under certain conditions, although some of them were already eliminated by linearizing the convective terms, but the results obtained as of now are encouraging. In addition, the current version of MFS can be used for parallel computation with OpenMP.

- The capillarity term is the most important parameter for the two-phase flow dispersion in porous media. At the same time, it increases the complexity of the model. Modifying this term has a big impact both on the flow behavior and on the numerical stability of the model. MFS is able to incorporate a capillarity term without the stability problems of Fluent.

- Two different zones of the reactor have been studied: a region containing the projection of a chimney from the center of the distribution tray and its surrounding area and another for a near-wall region, containing also the projection of one chimney and three additional half-chimneys from the surrounding area. No significant differences have been found in the flow behavior between the two zones. The liquid distribution does not change significatively as the flow descends, except at the interface of two different beds when porosity changes from one bed to another one.

- The simulation of the region under the projection of one near-wall chimney of the distribution tray and its surroundings hinted at the possibility of liquid tending to attach the wall as the flow descends. A more detailed study of one fourth of the reactor shows that there is no flow attachment to the wall. The regions under the projections of the chimneys placed near the wall spread the liquid faster radially in the first 3 m of the reactor than those in the center of the reactor. From a depth of 5 m on, that tendency changes, and the regions under the projections of the chimneys placed at the center of the distribution tray spread the liquid faster radially than those near the wall of the reactor. Liquid descends with higher velocity in the central region than in the

near-wall region, which allows the liquid from surrounding regions to move towards the center of the reactor. Comparing the results of cases F and G and taking into account the reactor dimensions, it can be concluded that no wall effect exists.

- A completely uniform distribution in the simulated depth of the reactor is not achieved. However, at a depth of 11 m, a uniform distribution is reached for the first 0.3 m in radial direction. In order to accurately determine the exit flow conditions, and whether the flow is uniformly distributed there, it would be needed to simulate the additional 7 m of the reactor, with the corresponding high computational cost. However, the uniform distribution is not important only at the last 7 m but at the first 11 m too, so the results obtained are enough to conclude that the two-phase flow distribution is not optimum in the reactor.

Chapter 8

Future work

Future work should be centered around the completion of the *Multiphase Flow Solver* code. The early results point in the good direction, but the complexity of two-phase flows through porous media requires some extensions to the current state of MFS. The main recommendations are described below:

- Stabilize the code for the case of large gradients for flows in which the density ratio between liquid and gas is large. In order to do this, the focus should be the convective and capillarity terms, and to a lesser extent, the drag terms. The linearization of the convective terms already removed some of the numerical instabilities. The next step could be the implementation of different discretization schemes for those terms. Although not presented in this document, a collocated mesh was also tested and the Rhie-Chow [31] interpolation used, but the results were no significatively different from those obtained with the staggered grid, so it is not recommended to change the type of grid.

- MFS is based on an Eulerian approach. It would be interesting and could be worth trying to implement a Lagrangian approach as well, either by tracking the liquid-gas interphase or packages of both phases. A combined Eulerian-Lagrangian approach is also an option. However, this point needs better definition before being attempted.

- Since the capillarity term is the key one, it is highly recommended to search for alternative models to the ones presented in this document.

- Implement chemical reactions and heat and mass transfer processes. Species

concentrations and temperature can be implemented as scalars, with the corresponding transport equations for each of them.

- Once the code is stable under all conditions, and chemical reactions and heat and mass transfer processes have been implemented, expand it to a cartesian three-dimensional domain.

Nomenclature

Latin symbols

C_2 ..... inertial resistance coefficient (m^{-1})
D_p ..... partial diameter (m)
d_{min} ..... minimum diameter (m)
f ..... wetting efficiency
F ..... drag force per unit volume $(N\ m^{-3})$
G ..... gas surface flow rate $(kg\ m^{-2}\ s^{-1})$
g ..... gravity acceleration $(m\ s^{-2})$
K ..... drag coefficient $(kg\ m^{-3}\ s^{-1})$
L ..... liquid surface flow rate $(kg\ m^{-2}\ s^{-1})$
$\dot{m}$ ..... mass flow rate per volum unit $(kg\ s^{-1})\ m^{-3}$
p ..... capillary pressure (Pa)
P ..... pressure (Pa)
t ..... time (s)
U ..... velocity $(m\ s^{-1})$
u ..... x-direction velocity $(m\ s^{-1})$
v ..... y-direction velocity $(m\ s^{-1})$
x ..... x coordinate (m)
y ..... y coordinate (m)

Greek symbols

α ..... coefficient for u velocity correction $(m^3\ s\ kg^{-1})$
β ..... coefficient for v velocity correction $(m^3\ s\ kg^{-1})$
γ ..... permeability (m^2)
ε ..... porosity
θ ..... volume fraction

μ ..... dynamic viscosity $(Pa\ s)$
ρ ..... density $(kg\ m^{-3})$
σ ..... surface tension $(N\ m^{-1})$
ϕ ..... any scalar
Ψ ..... capillarity pressure (Pa)

Superscript

new ..... new time step
o ... used for the momentum source term which does not include the pressure term
old ..... old time step
$'$ ..... correction value
$*$ ..... value from the previous iteration

Subscript

e ..... east face of a cell
E ..... center of the east neighboring cell
f ..... fluid
g ..... gas phase
i ..... x-direction cell face index
I ..... x-direction cell center index
j ..... y-direction cell face index
J ..... y-direction cell center index
l ..... liquid phase
P ..... center of the cell
s ..... solid phase
w ..... west face of a cell
W ..... center of the west neighboring cell
x ..... x direction
y ..... y direction

List of publications

Journal papers

- **"Numerical simulation of the liquid distribution in a trickle-bed reactor. Part I: Study of the flow in a distribution chimney."** Martínez M., López J., Pallarès J., López A., Albertos F., García M.A., Grau F.X. *Submitted for publication to Chemical Engineering Science, 2011.*

- **"Numerical simulation of the liquid distribution in a trickle-bed reactor. Part II: Study of the two-phase flow dispersion in the packed beds."** Martínez M., Pallarès J., López A., Albertos F., García M.A., Grau F.X. *Submitted for publication to Chemical Engineering Science, 2011.*

- **"Study of the effect of the wall on the distribution of an isothermal two-phase flow in a hydrodesulfurization reactor."** Martínez M., Pallarès J., López A., García M.A., Grau F.X. *Submitted for publication to Computers and Chemical Engineering, 2011.*

Contributions to conferences

- **"Numerical study of the wall effect on the liquid distribution in a trickle-bed reactor."** Martínez M., Pallarès J., López A., García M.A., Grau F.X.. Oral presentation at the *8th International Conference on Computational Fluid Dynamics in the Oil and Gas, Metallurgical and Process Industries, June 21-23 2011, Trondheim, Norway.*

- **"Numerical study of liquid distribution in a trickle-bed column: Development of a multiphase CFD code"** Martínez M., Pallarès J., López A., García M.A., Grau F.X. Poster presented at the *International Conference on Multiphase Flow (ICMF-2010), May 30 - June 4 2010, Tampa, Florida, United States.*

- **"Numerical simulation of liquid distribution in a trickle-bed reactor."** Martínez M., Pallarès J., López A., Albertos F., Grau F.X. Poster presented at the *17th International Congress of Chemical and Process Engineering, August 27-31 2006, Prague, Czech Republic.*

Bibliography

[1] Dudukovic, M.P., Larachi, F., Mills, P.L. *Multiphase reactors - revisited.* Chemical Engineering Science (1999) 54, pp. 1975.

[2] Cihla, Z., Schmidt, O. *A study of the flow of liquid when freely trickling over the packing in a cylindrical tower.* Collection Czechoslov. Chem. Commun. (1957) 22, pp. 896.

[3] Baker, T., Chilton, T.H., Vernon, H.C. *The course of liquor flow in packed towers.* Presented at the Wilmington, Delaware, Meeting (1935).

[4] Wang, Y.F., Mao, Z.S., Chen, J. *Scale and variance of radial liquid maldistribution in trickle beds.* Chemical Engineering Science (1998) 53, pp. 1153.

[5] Boyer, C., Fanget, B. *Measurement of liquid flow distribution in trickle bed reactor of large diameter with a new gamma-ray tomographic system.* Chemical Engineering Science (2001) 57, pp. 1079.

[6] Harter, I., Boyer, C., Raynal, L., Ferschneider, G, Gauthier, T. *Flow distribution studies applied to deep hydro-desulfurization.* Ind. Eng. Chem. Res. (2001) 40, pp. 5262.

[7] Jiang, Y., Khadilkar, M.R., Al-Dahhan, M.H., Dudukovic, M.P. *CFD of multiphase flow in packed bed reactors: I. k-fluid modelling issues* AIChE Journal (2002) 48.

[8] Jiang, Y., Khadilkar, M.R., Al-Dahhan, M.H., Dudukovic, M.P. *CFD of multiphase flow in packed bed reactors: II. Results and applications* AIChE Journal (2002) 48.

[9] Holub, R.A., Dudukovic, M.P., Ramachadran, P.A. *A phenomenological model for pressure drop, liquid holdup, and flow regime transition in gas-liquid trickle flow.* Chemical Engineering Science (1992) 47, pp. 2343.

[10] Attou, A., Boyer, C., Ferschneider, G. *Modeling of the hydrodynamics of the cocurrent gas-liquid trickle flow through a trickle bed reactor.* Chemical Engineering Science (1999) 54, pp. 785.

[11] Gunjal, P.R., Ranade, V.V., Chaudhari, V. *Liquid distribution and RTD in trickle bed reactors: experiments and CFD simulations.* The Canadian Journal of Chemical Engineering (2003) 81, pp. 821.

[12] Ansys Fluent 12.0. Documentation, Ansys Inc. 2009.

[13] Boyer, C., Koudil, A., Chen, P., Dudukovic, M.P. *Study of liquid spreading from a point source in a trickle bed via gamma-ray tomography and CFD simulation.* Chemical Engineering Science (2005) 60, pp. 6279.

[14] Jiang, Y., Khadilkar, M.R., Al-Dahhan, M.H., Dudukovic, M.P. *Two-phase flow distribution in 2D trickle-bed reactors.* Chemical Engineering Science (1999) 54, pp. 2409.

[15] Harlow, F.H., Amsden, A.A. *Numerical calculation of multiphase fluid flow.* Journal of Computational Physics (1975) 17, pp. 19.

[16] Moukalled, F., Darwish, M. *Pressure based algorithms for multi-fluid flow at all speeds. Part I: Mass conservation formulation.* Numerical Heat Transfer. Part B: Fundamentals. (2004) 45, pp. 495.

[17] Moukalled, F., Darwish, M. *Pressure based algorithms for multi-fluid flow at all speeds. Part II: Geometric conservation formulation.* Numerical Heat Transfer. Part B: Fundamentals. (2004) 45, pp. 523.

[18] Tsochatzidis, N.A., Karabelas, A.J., Giakoumakis, D., Huff, G.A. *An investigation of liquid maldistribution in trickle beds.* Chemical Engineering Science (2002) 57, pp. 3543.

[19] Hoftyzer, P.J. *Liquid distribution in a column with dumped packing.* Trans. Instn Chem. Engrs (1964) 42, pp. T109.

[20] Gunn, D.J. *Axial and radial dispersion in fixed beds.* Chemical Engineering Science (1987) 42, pp. 363.

[21] Cairns, W.A. *Liquid distribution characteristics of tower packing materials.* Canadian Chemistry and Process Industries (1948), pp. 314.

[22] Marchot, P., Toye, D., Crine, M., Pellser, A.M., L'Homme, G. *Investigation of liquid maldistribution in packed columns by x-ray tomography.* Trans IChemE (1999) 77, pp. 511.

[23] Attou, A., Ferschneider, G. *A two-fluid hydrodynamic model for the transition between trickle and pulse flow in a cocurrent gas-liquid packed bed reactor.* Chemical Engineering Science (2000) 55, pp. 491.

[24] El-Hisnawi, A.A. *Tracer and reaction studies in trickle-bed reactors.* D.Sc. Thesis, Washington University, St. Louis, USA (1981).

[25] Grosser, K.A., Carbonell, R.G., Sundaresan, S. *Onset of pulsing in two-phase cocurrent downflow through a packed bed.* AIChE Journal (1998) 34, pp. 1850.

[26] Versteeg, H.K., Malalasekera, W. *An introduction to computational fluid dynamics. The finite volume method.* Pearson Education Limited, 1995.

[27] DeBlois, B.M. *Linearizing convection terms in the Navier-Stokes equations.* Comput. Methods Appl. Mech. Engrg. (1997) 143, pp. 289.

[28] Conte, S.D., DeBoor, C. *Elemental numerical analysis.* McGraw-Hill, New York (1972).

[29] Jones, W.P., Launder B.E. *The prediction of laminarization with a two-equation model of turbulence.* International Journal of Heat and Mass Transfer (1972) 15, pp. 301.

[30] Ergun, S. *Fluid flow through packed columns.* Chem. Process Eng. (1952) 48, pp. 89.

[31] Rhie, C.M., Chow, W.L. *Numerical study of the turbulent flow past an airfoil with trailing edge separation.* AIAA Journal (1983) 21, pp.1525.